Sensor and Simulation Notes

Note 338

March 23, 1992

MODELING HYBRID EMP SIMULATORS WITH GAP FEED LOCATIONS FAR FROM THE RF SOURCE

C. Zuffada
J. Martinez

Kaman Sciences Corporation
Advanced Electromagnetics Division
2800 28th Street Suite 370
Santa Monica, CA 90405

C. Baum
W. Prather

Phillips Laboratory
Kirtland AFB, NM 87117

ABSTRACT

Recently a new bybrid EMP simulator has been developed where the signal is transmitted by a high-quality coaxial cable from a RF source on the ground to a point above the ground where the cable is cut to create a gap source. The cable is made part of the antenna by passing it through chokes which provide a frequency dependent inductively coupled impedance, thus making the cable-shield exterior effectively loaded for exterior scattering purposes over a wide band of frequencies of interest. Two geometries have been analyzed and practically implemented and a simple analytical model has been developed to make current and field predictions. Comparisons are presented between measurements and calculations.

CONTENTS

ACKNOWLEDGEMENTS

We wish to thank Dr. D. McLemore of KSC, Mr. B. Burton formerly of Kaman Sciences Corporation and Mr. T. Tran of Phillips Laboratory for their assistance with the field mapping effort for both antenna configurations.

SUMMARY

This note describes the features of an illuminator which offers flexible geometry, ease of construction and handling, and low cost. It consists of a loop arbitrarily shaped in principle, made with a coaxial cable and simply cut open at some point to create a gap source, with currents flowing along the exterior surface of the cable outer conductor, and through a properly chosen loading impedance. Because the basic idea rests with the feed rather than the antenna shape, we refer to it as the Wormhole Feed Concept, as will be explained in Sec. 1. Such an antenna concept was implemented recently in two geometries, triangular and semielliptical. The description of these particular antennas and the related instrumentation set-up is presented in Sec. 2.

To characterize the electromagnetic features of such an antenna a mathematical model was developed to calculate currents and fields; this is detailed in Sec. 3. Section 4 presents a comparison between model predictions and actual field map measurements, showing a very satisfactory agreement between the two. This suggests that the important features of the antenna are understood and well described in the model of Sec. 3. Finally, some recommendations for design simplifications/improvements are offered in Section 5.

INTRODUCTION

Recently the interest of the community involved with assessing system's vulnerability to RF signals, such as EMP, has turned to low level continuous wave testing techniques as a possible supplement to the more costly, traditional high level pulse methods. In fact, in addition to cost savings, there are several advantageous features to continuous wave testing, one of which is the availability of simple, "portable" illuminators which can generate smooth, plane-wave-like fields over wide frequency ranges and reasonably large volumes. For linear systems, by measuring the system's response at each frequency of interest one can determine a "transfer function" operator which, when multiplied with the spectrum of any given RF threat, will generate the spectrum of the system's response to that threat. An inverse Fourier transform will then allow to calculate the time domain response.

Resistively loaded loops have been used for this application because of their ability to produce fields at low frequency (quasi static limit) as well as at high frequency when the radiation emanates from a relatively small region around the source location. By proper choice of the resistive load the ratio E/H at the center of a loop in air can be made equal to 377 Ω, in the low frequency limit. Additionally the resistance damps the loop resonances and enhances the antenna bandwidth. Various geometries are possible depending on specific field requirements. One such geometry is a semi ellipse above the earth with a source at various possible locations, including the highest point above the ground. For this geometry it was shown [1] that the optimum resistive loading depends on the source location and deviates somewhat from that of a circular loop of the same perimeter [2], which is independent of it, due to the symmetry of the antenna.

Concerning the source location, it is often desirable to produce electric fields which are horizontally polarized. This requires the source to be at the highest point above the ground. Up to now, in this case, the signal coming from the network analyzer is made to travel inside a coaxial cable to an amplifier located under the antenna, at its center. From there a coaxial cable brings the amplified signal up to the actual feed point above the ground, where some matching network is employed to drive the antenna. Such a cable is a large scatterer and it will cause perturbation of the fields in the volume where the test object could be located. The perturbation can be minimized by placing it in a plane where the electric field is perpendicular to it but this solution prevents the test article from being positioned under the antenna, where the field levels are the highest, and have desirable spatial properties [2]. This note describes a feed concept which eliminates the presence of the cable and/or other instrumentation in the working volume, by making this cable part of the antenna.

1.0 FUNDAMENTAL CONCEPTS

The basic ideas for an illuminator which allows for a part of the antenna to be also part of the feed without compromising its electromagnetic environment are presented in [3]. This section is a reproduction of Sec. 2 and 3 of that note.

The problem with a long slender conductor (such as a coaxial cable shield) is that, if there is a component of an incident electric field parallel to the path of this conductor, then large axial currents are induced with associated large scattered fields. Incident electric-field components transverse to this path scatter relatively little, such scattering being related to the small transverse dimensions of the conductor.

One way to look at this is the asymmetry in the physical world seen in the presence of electrical conductors (e.g., metals), compared to the lack of magnetic conductors (due to the apparent lack of magnetic monopoles). One might consider an ideal magnetic boundary as in Fig. 1A for its possible use in containing conductors (cables) inside a long slender magnetic tubular boundary. This isolates the interior cable from the external fields (no currents on the cable exterior). However, by forcing the external axial magnetic field to zero this kind of a "shield" is also a large scatterer of the external fields. This is just the dual (interchanging E and H) of a slender conductor. Of course, there is no such ideal magnetic conductor, but it can be approximated by a pipe with a high permeability (and thick) wall as in Fig. 1B. This also shows part of the problem in such an approach in that a large axial magnetic flux is induced in the wall of such a pipe.

A way out of this problem of electric versus magnetic boundaries is to mix them, i.e., expose suitable short lengths of the conductor (cable shield) to the external incident electric field, while separating these by use of inductive magnetic cores (effective magnetic boundaries) as indicated in Fig. 1C. Such cores represent a localized high impedance (a choke) limiting the current induced on the conductor. For sufficiently large impedances we can think of the exterior scattering as being from a colinear array of unconnected short conductors. This scattering will be small provided core spacing d is small compared to the half wavelength. Note also that the separation between cores breaks up any significant increase of magnetic flux parallel to the conductor. In the limit of a large number of separated cores we can think of a dielectric/magnetic sandwich comprised of alternate thin layers of magnetic material separated by thin dielectric layers as discussed in [4]. Here we are looking at such a structure from the exterior properties as compared to the interior emphasis in [4]. Even with separated cores as in Fig. 1C, the individual cores might be constructed in such a sandwich form for high-frequency purposes.

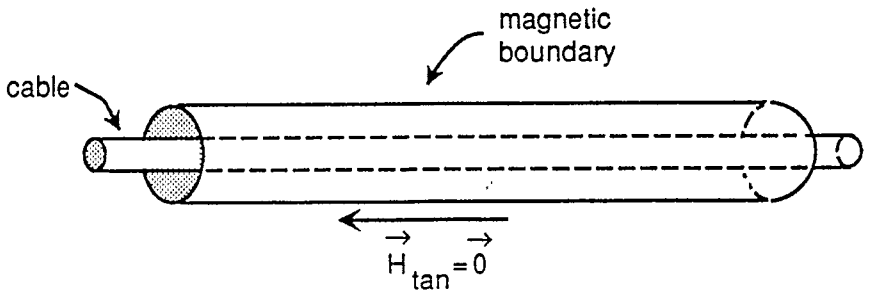

A. Tubular magnetic boundary

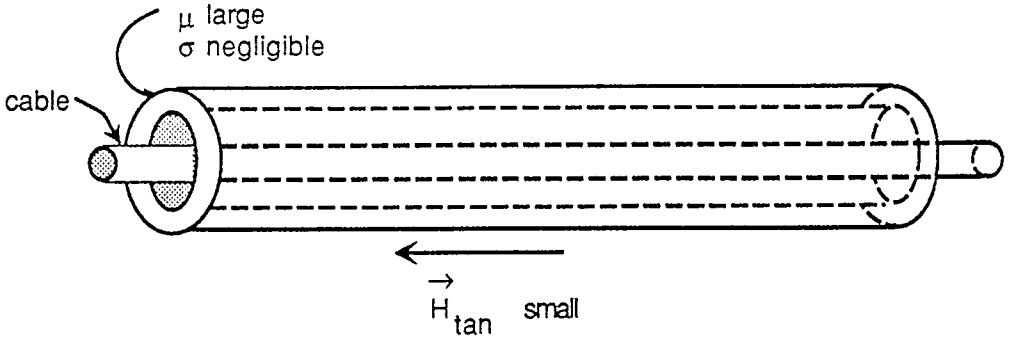

B. Pipe of high permeability

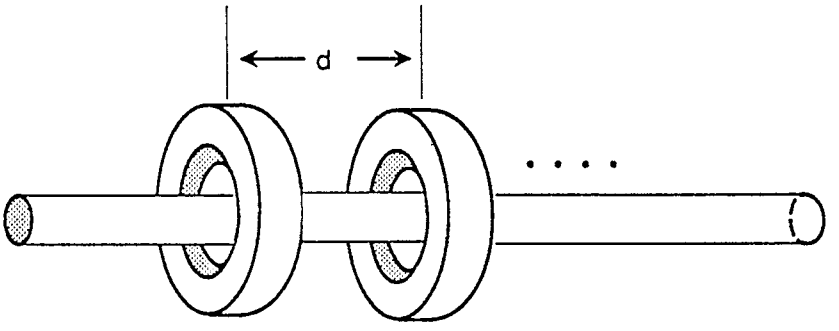

C. Spaced inductive cores

Figure 1. Progression from Magnetic Boundary to Spaced Inductive Cores.

With this general concept of effectively isolating the conductor by the alternating electric/magnetic boundaries for the exterior fields we can think of this in topological terms. This is analogous to a wormhole which conceptually returns electric flux lines (to make them closed) between positive and negative charges [5]. This wormhole is postulated to pass between the charges in some higher dimension of space. Another paper [6] shows how a special helical transmission line can propagate an effective magnetic monopole with the magnetic field lines closing by returning through the tube formed by the helical solenoid. In the present case a well-designed alternating electric/magnetic boundary gives something like a wormhole, in the sense that a signal cable can pass between two points in three-dimensional space without being there (approximately) in an exterior electromagnetic scattering sense.

Having a technique to approximately hide a conducting cable, the next question is where to place this cable path with its special "shield". Referring to Fig. 2 the topological problem is where to place this path with endpoints at B and somewhere on the earth surface. As mentioned previously, the path should be excluded from the test volume since the system under test is to go there. Furthermore, one would prefer that this path not be close to the test volume because its shield is as a practical matter imperfect (non completely invisible).

Observe that there are already two earth-contact positions, A and C, for the simulator proper (antenna). At these locations there are ground rods "already" in place. One could use either A or C, but since one of these may be closer to B(i.e., C in the Fig. 2 example), we may choose this one and make our conductor path connect B and C. The next question concerns where the conductor path from C to B should be placed. An obvious choice is to place it along the same path as the resistively loaded antenna structure where it can be supported by the same dielectric support structure (poles, catenary, etc.).

Then , as in Fig. 3A, consider that there is a current I along the antenna path consisting of wire-connected resistors, each of value

$$R = \frac{R'}{\nu}$$

$\nu \equiv$ number of resistors per meter (1)

Let the adjacent cable path have its inductive cores (chokes) spaced the same as the resistors (ν per meter) giving

$$d = \frac{1}{\nu} \quad (2)$$

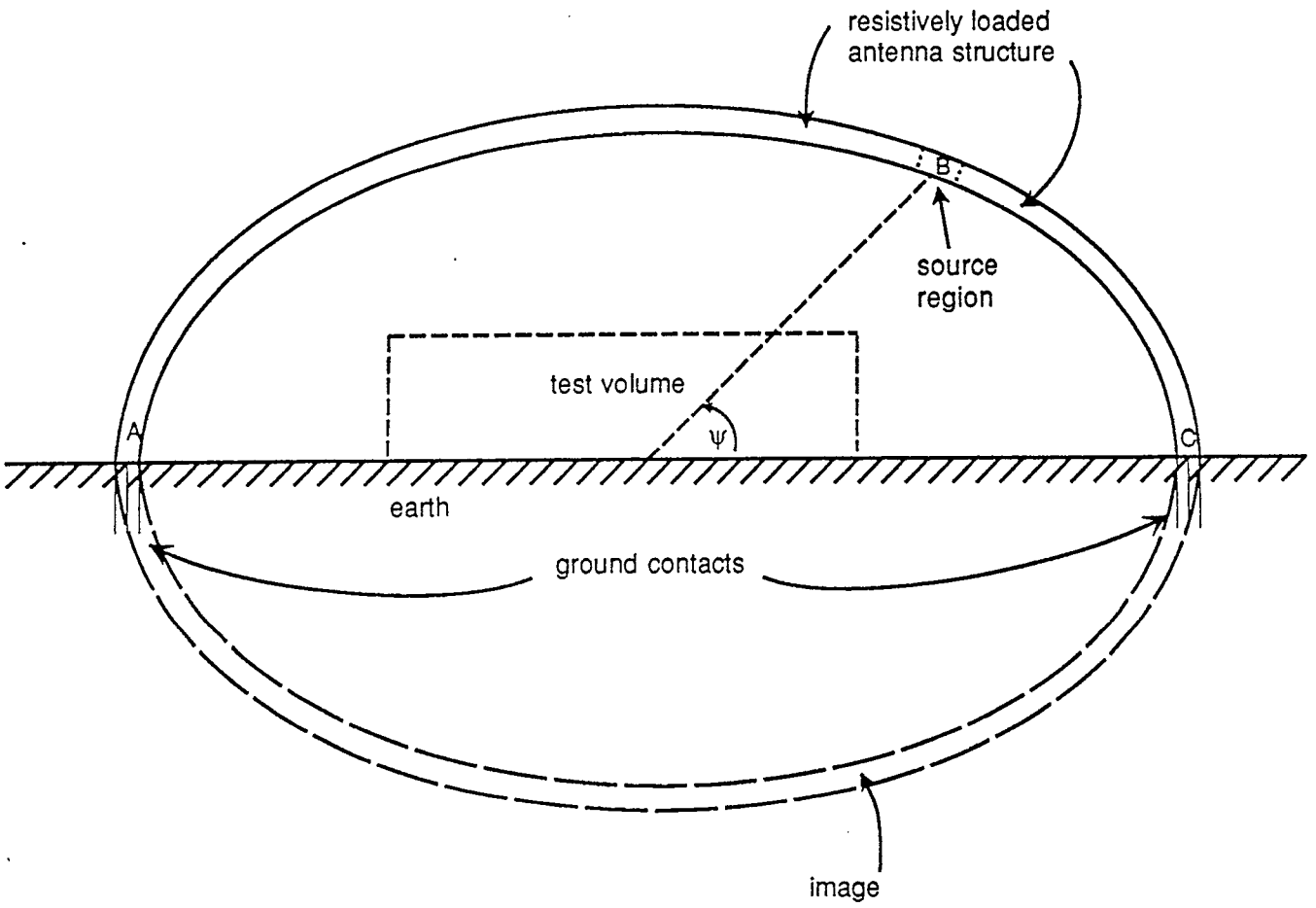

Figure 2. Hybrid EMP Simulator.

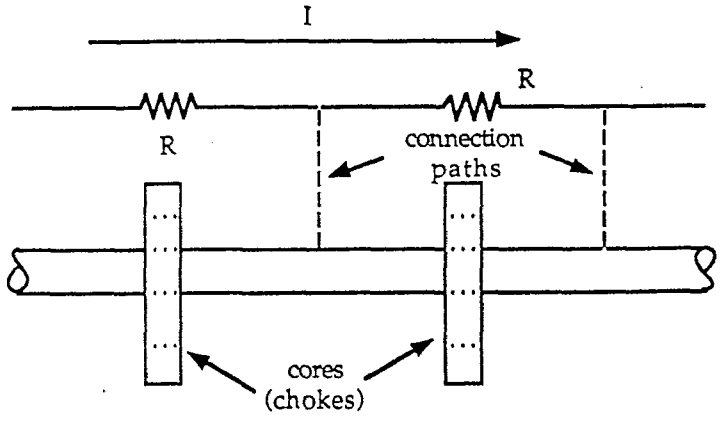

A. Resistively-loaded wire in parallel with core-loaded cable

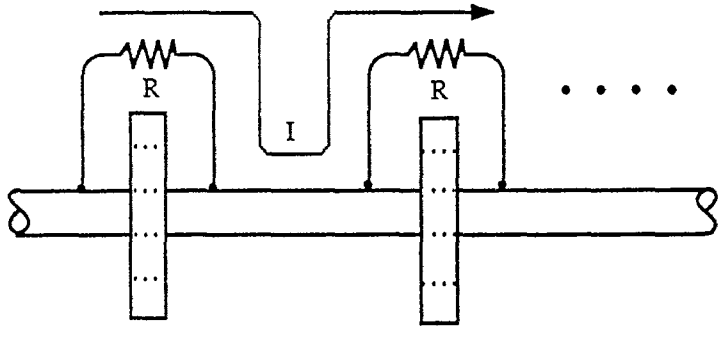

B. Current diverted to cable-shield exterior

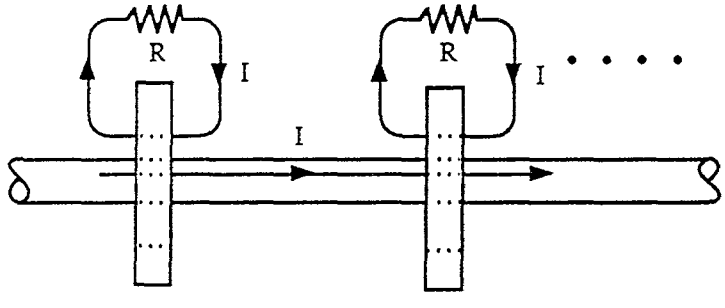

C. Current through resistors separated from opposite current on cable-shield exterior

Figure 3. Progression from Adjacent Paths to Common Path for Resistively-Loaded Cable-Shield Exterior.

and positioned adjacent to the resistors. With negligible current on the cable-shield exterior (for half wavelength $\lambda/2 >> d$), let us electrically connect each wire between resistors to the corresponding adjacent position on the cable-shield exterior via the connection paths in Fig. 3A. Negligible current runs on these connections. Then as in Fig. 3B deform the wire and connections so that the current I passes through the resistor to the cable shield and back to the next resistor, etc. Negligible current still passes through each choke on the cable-shield exterior. Then in Fig. 3C the wires connecting each resistor to the cable shield on opposite sides of a choke are slid together (inside the choke), connected to each other, and removed (not necessarily) from the cable shield. Now I flows on the cable-shield exterior through the choke but is cancelled by an opposite I on the wire connected (both ends) to the resistor. The choke now acts as a transformer.

The two paths have now become one. There is a significant, but controlled, current I on the cable-shield exterior. The cable shield should be a good one, say a continuous metal tube (aluminum or copper) instead of a braid. This is consistent with a high-quality foam-dielectric (or similar) coaxial cable capable of efficiently transmitting signals in the GHz range. The requirement to make the cable "invisible" by the special alternating electric/magnetic boundary has been made a little easier. It need not prevent "all" current from flowing on the cable-shield exterior, but merely limit it to I, the value desired for the antenna.

Figure 4A shows a view along the cable axis of the core and loading resistor (with wire linking through the core). The current I (approximately) in this wire associated with the resistor is not centered in the core, giving a non uniform excitation of the core. One can compensate by offsetting the cable shield to obtain better angular uniformity for the magnetic field associated with the common mode (small) of the currents on this wire plus cable-shield exterior. Better still, one can replace the single resistor of resistance R by N resistors, each of resistance NR spaced at equally angles $(2\pi/N)$ around the core as indicated in Fig. 4B. This gives a more uniform current and magnetic-field distribution in an angular sense around the core. One can extend this concept by replacing the wire loops by a continuous metal structure with a circumferential slot around the outside [7, 8], the N resistors being connected across this slot.

If the core is approximated as a simple inductance L, then define

$$\omega_o \equiv \frac{R}{L} \tag{3}$$

The effective impedance of the resistor-loaded cores is then

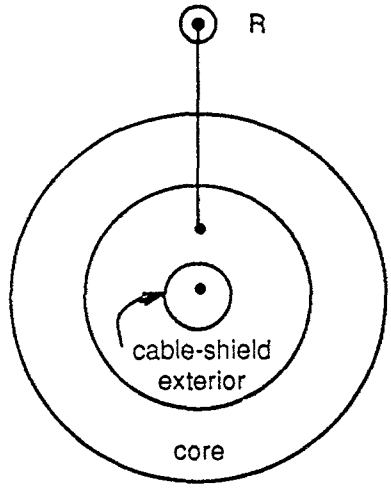

A. Single resistor

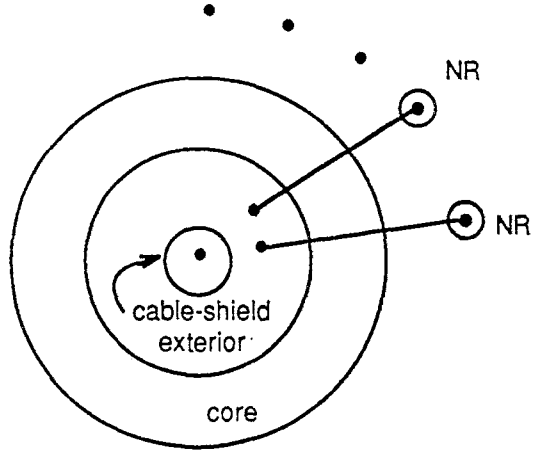

B. Multiple (N) resistors in parallel

Figure 4. Resistively Loaded Cores.

$$\tilde{Z}(s) = R\,//\,(sL) = \left[\frac{1}{R} + \frac{1}{sL}\right]^{-1}$$

$s = \Omega + j\omega \equiv$ Laplace - transform variable or complex frequency (4)

In this form the resistor-loaded cores give an effective impedance per unit length R' for this antenna/cable path provided

$$\omega_o << \omega \tag{5}$$

For a given R' then one can choose v(=1/d) and L to make ω_o some desired low-frequency limit on the ideal performance of the antenna.

In a more general sense the choke impedance $\tilde{Z}_{ch}(s)$ need not exactly follow an inductive form sL for L constant (>0). In this more general case we have

$$\tilde{Z}(s) = R\,//\,\tilde{Z}_{ch}(s) = \left[\frac{1}{R} + \frac{1}{\tilde{Z}_{ch}(s)}\right]^{-1} \tag{6}$$

For R' to dominate the antenna performance we require

$$\left|\tilde{Z}_{ch}(j\omega)\right| >> R \tag{7}$$

for frequencies of interest, so it is important only that the choke impedance be large compared to R. As one increases the number of resistors (decreasing d) R is decreased, making the requirement of Eq. (7) be met for a broader band of frequencies.

The following section describes a practical implementation of the basic ideas discussed above. Ferrite cores were used to generate the necessary $\tilde{Z}_{ch}(j\omega)$ and, as a first step, the cores were not loaded with resistors. The objective was to demonstrate the concept and our present choice of materials, parts and design features are not necessarily optimal. Two shapes have been investigated: a triangular half-loop and a semielliptical half-loop.

2.0 PHYSICAL DESCRIPTION OF THE ANTENNA

2.1 Suspension System

The first version of the Wormhole Feed Concept (Fig. 5) consisted of a coaxial cable (characteristic impedance = 50 Ω, outer diameter (2r) = 7/8") shaped to form an approximately triangular loop of height (h) ~ 20 m and base (2b) ~ 80 m, laying in a plane perpendicular to the ground and suspended at the apex via a dielectric rope. To relieve the coaxial cable of the tensioning action, a nylon rope was laid along the cable in the desired geometrical shape of the illuminator and the cable was made to follow the intended shape by use of clamping plastic sleeves, positioned every few meters, which allowed for free movement of the cable with respect to the nylon rope when the latter was tensioned.

The support system is ideally provided by stretching a dielectric rope between two wooden poles, which was implemented at Kirtland when the concept of this illuminator was first demonstrated. In that case the existing Achilles III [9] support system was used and the tension on the suspension rope was adjusted so that the desired antenna height of 20 m was obtained. Later on this design was simplified and improved by eliminating the portion of coaxial cable laying on the ground, relocating the amplifier outside the working volume, and grounding both ends as shown in Fig. 6. From the electromagnetic standpoint the latter configuration has the advantage of providing a working volume free of instrumentation and eliminates the accumulation of charges between the horizontal portion of cable and the earth.

In addition to the triangular geometry the semielliptical geometry was also implemented (See Fig. 7) using the same support system and overall design. To shape the cable into a semi ellipse (Ellipticus) a slightly more complicated dielectric support system was necessary.

2.2 Feed And Associated Electronic Equipment

A signal from a network analyzer is fed via a coaxial link to an amplifier, whose output drives one of the coaxial legs of the antenna from one vertex. At the apex the coaxial cable is opened up and its center conductor is connected to the shield of the other coaxial leg, either directly or via a "transformer" (See detail of Figs. 5 and 7). This second leg has its center conductor shorted to its shield. The mechanical support of the gap is provided by a piece of plexiglass to which the two halves of coaxial cable are attached and held in place by means of plastic straps (see inset of Figs. 5-7). The shields of both legs are grounded to the earth, and to the ground of the amplifier. It is noted that the actual feed point of the loop is the apex, which can be regarded as a gap

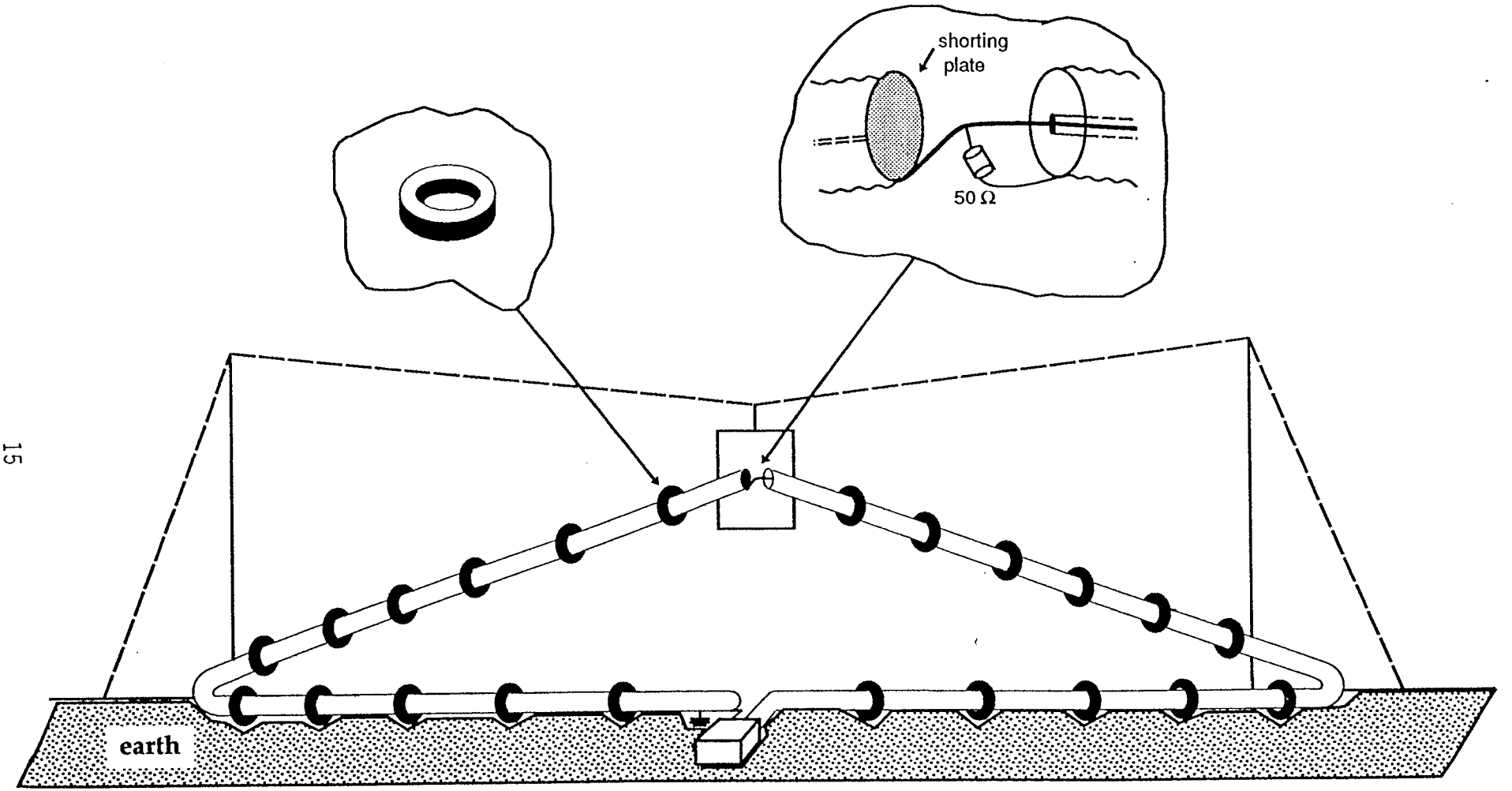

Figure 5. Triangular loop geometry, first design.

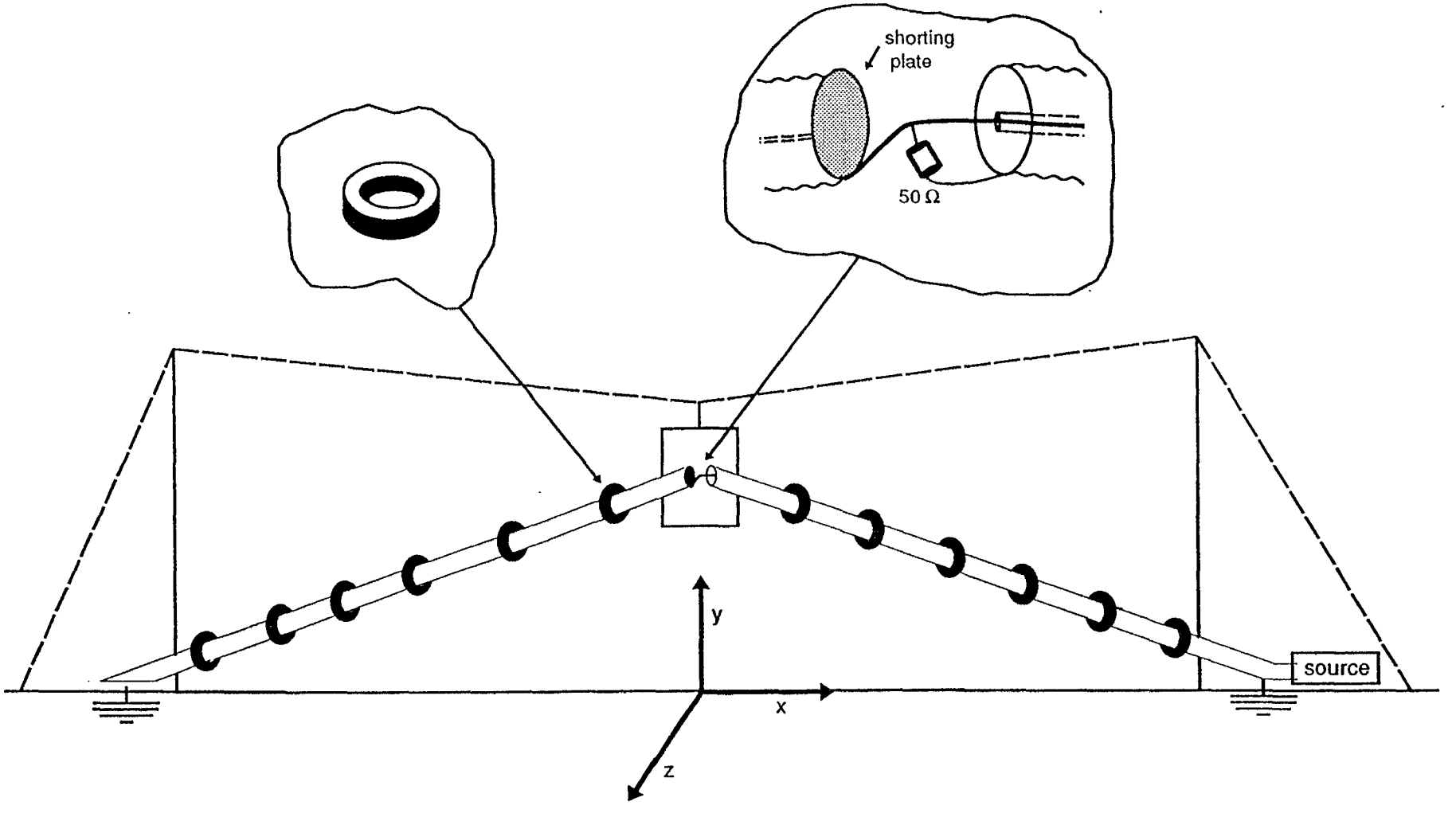

Figure 6. Triangular loop geometry, second design..

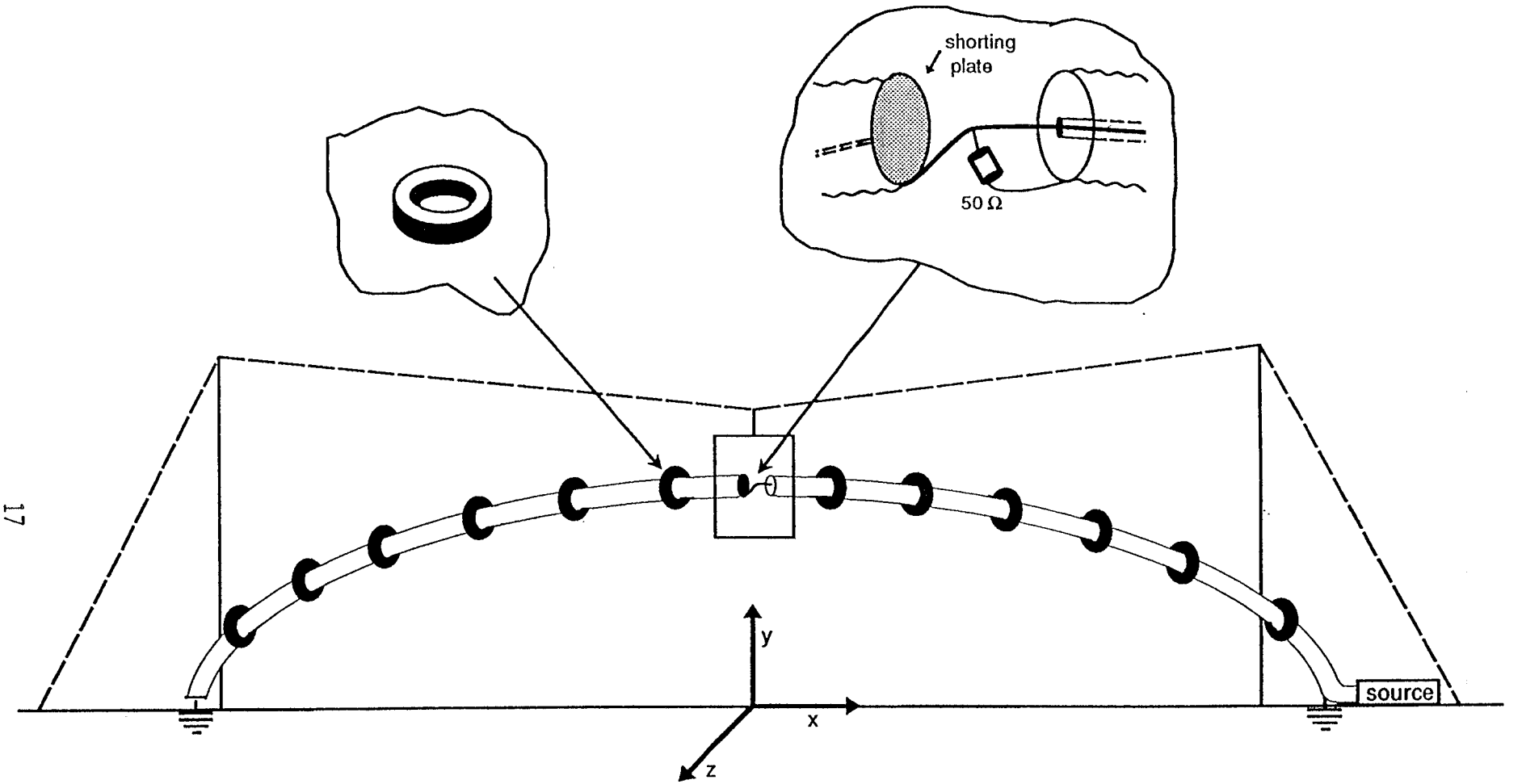

Figure 7. Elliptical loop geometry.

source, and the shields of both legs serve as linear conductors for the flow and radiation of current. To insure smooth fields over a wide frequency range the antenna is loaded with ferrite toroidal beads designed to provide both inductive and resistive losses, symmetrically placed along its legs. Ferrite toroids characteristics and the rationale for our choice of units and their placement along the antenna are presented in Sec. 2.3.

2.3 Properties of Ferrite Beads For RF Suppression

Ferrite beads and toroidal cores are used extensively to provide attenuation of unwanted RF signals in systems, subsystems and circuits. To accomplish this, use is made of the losses that such meterials present over a wide spectrum of frequencies. Such losses, due to eddy currents, hystereses and residual core losses (relaxation of magnetic domain walls) are such that the device can be modeled simply as a frequency dependent R-L series impedance; at relatively low frequencies the inductive portion is dominant, while the resistive part becomes dominant at higher frequencies. The overall impedance is small at low frequency, then it increases, reaches a broad maximum and eventually decreases, as shown in Fig. 8, for three types of ferrites. When used as RF suppressors the ferrite material basically acts as a "low pass filter" whereby the frequency of the desired signal must be low enough so that the losses of the chosen ferrite are too low to affect it. On the contrary, at higher frequencies, the increasing resistance acts to progressively reduce the unwanted signals that propagate along the path where the ferrite toroid/bead has been installed. The choice of ferrite material is mainly dictated by the required suppression band, and more than one type of material might be necessary for wide-band operations.

Our design shares some aspects of the RF suppression problem described above. When the antenna is not loaded the loop resonances would give rise to electromagnetic fields such as those shown in Fig. 9 at the points (0, 3, 20) (The reader is referred to Fig. 5 for an illustration of the Cartesian coordinate system used for this problem). Such behavior has its origin in the interference between the current flowing along each leg directly from the source and that coming back from the other leg after having traveled along half the loop. One can see that the extremely wide variations of the field components make this antenna unsuitable for simulating a smooth plane wave environment. To damp the resonances the antenna was therefore loaded with 240 ferrite beads distributed as follows; 120 material #43 ferrites were originally placed along the antenna legs, spaced roughly uniformly for the demonstration test in Albuquerque, but during the test five were broken. Furthermore, 120 material #77 ferrite beads were originally distributed along the base of the antenna, uniformly spaced; however, breakage of ten units occurred during the tests. The optimum number of beads was determined empirically by increasing their number

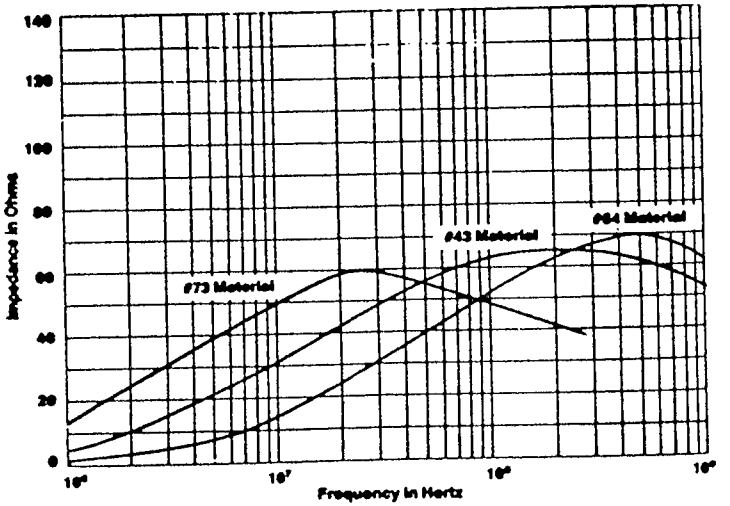

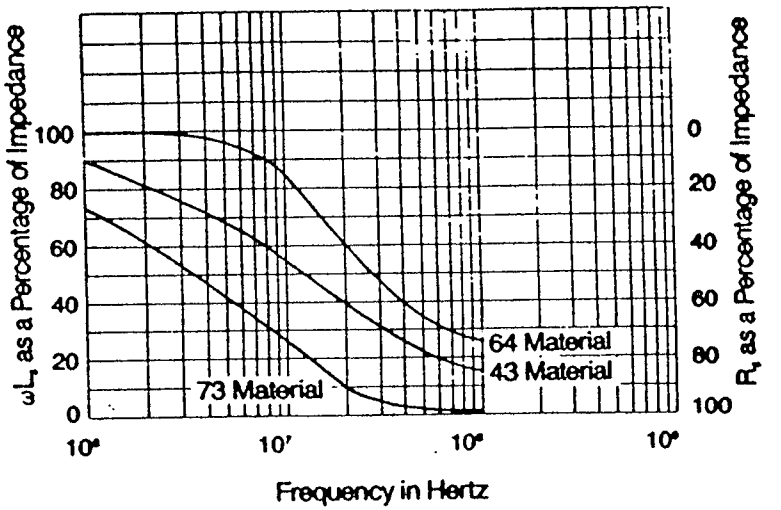

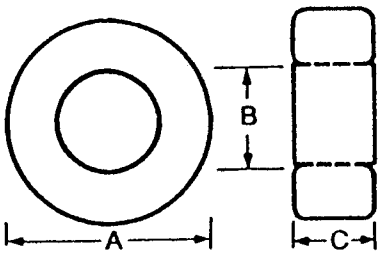

A = 2.4"
B = 1.4"
C = 0.5"

Figure 8. Properties of ferrite beads for three different materials, identified by their commercial names, and provided by manufacturers
#64 permeability 250
#43 permeability 850
#73 permeability 2500

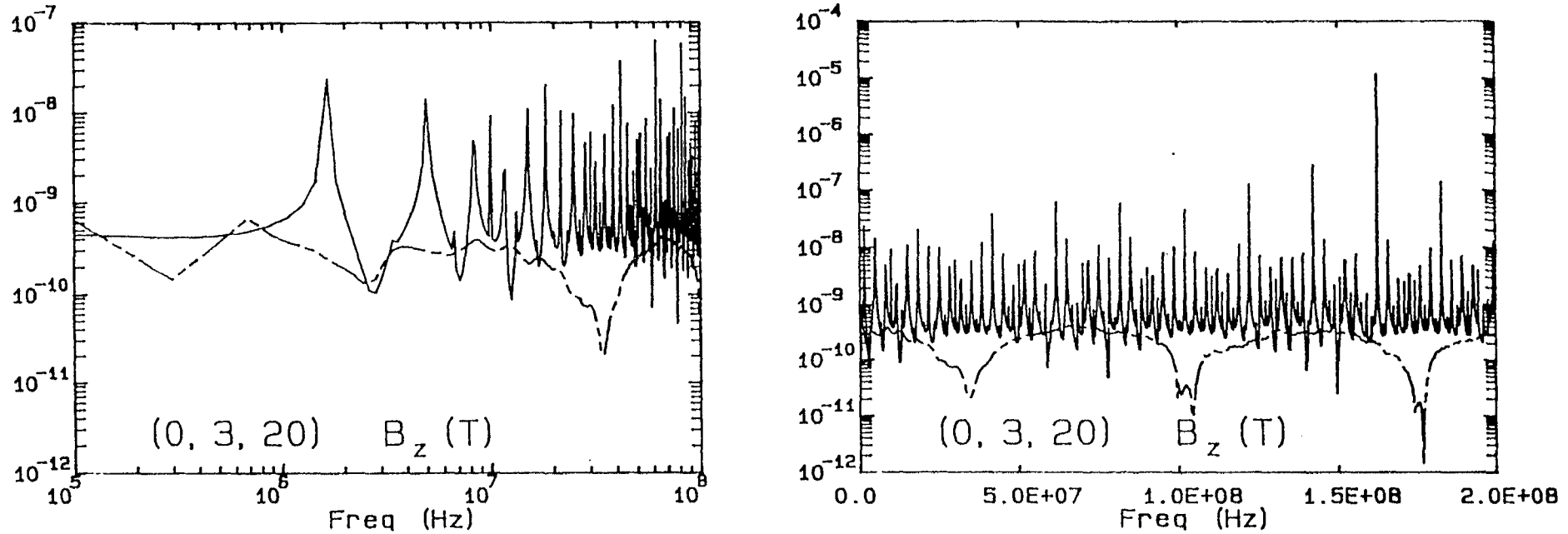

Figure 9. Effect of ferrite loading on the magnetic induction at (0, 3, 20).
Solid curve - Calculation without ferrites
Dashed curve - Measurement with ferrite loading

in three steps and observing that the measured B_z field along the antenna axis at the distance of 20 m exhibited an increasingly smooth behavior up to 200 MHz. It is pointed out that the notation #43 and #77 are widely used commercial names, identifying the metals used in the ferrite compounds.

The ferrite beads impedance was obtained experimentally for each material in two steps. First, by loading the end of a coaxial cable with a wire through which 10 ferrites have been routed, the series impedance for the ten elements can be obtained through direct measurement of the reflection coefficient. This procedure is required to obtain accurate measurements at low frequency, i.e. up to a few MHz, where the amplitude of the reflection coefficient for one single bead is too close to one and the phase to 180° to allow a correct reading. On the other hand, at high frequency the series combination of ferrites introduces a capacitive effect which lowers the impedance. Therefore, a second step is necessary where only one ferrite is passed through the wire for a correct measurement at high frequency; the low frequency and high frequency values of the reflection coefficient are then combined. In summary, the operation to be performed is the following

$$Z_f = 50\frac{1+\rho_m}{1-\rho_m} \tag{8}$$

where ρ_m is the measured reflection coeffcient and 50 (Ω) is the characteristic impedance of the coaxial cable used for the experiment. If ten ferrites are measured the value of Z_f thus obtained must be divided by 10. The impedance for material #43 and #77 single beads (outer diameter = 2.4", inner diameter = 1.4", height = 0.5") derived as described above are illustrated in Figs. 10 and 11.

Our particular choice of ferrite material satisfied the need to damp current in a broad frequency range, as indicated by the impedance values shown in the above figures. The placement of material #77 ferrites along the base of the triangle was justified by the fact that their effect is important at low frequency, as evinced from Fig. 10. Since at low frequency the antenna is electrically small the location of these beads is not very critical to provide an attenuation of the return current from one leg back to the other, because the variation of the current along each leg is small. At high frequencies, however, the variation of the current is rapid and an effective damping is achieved only if the ferrites are placed all along the antenna legs, starting from the source point. However, in the improved design both species of toroids were distributed all along the legs, alternately, but with somewhat random separation. The field smoothing process is accomplished here at the expense of its level, since a lot of the energy is dissipated in the loading

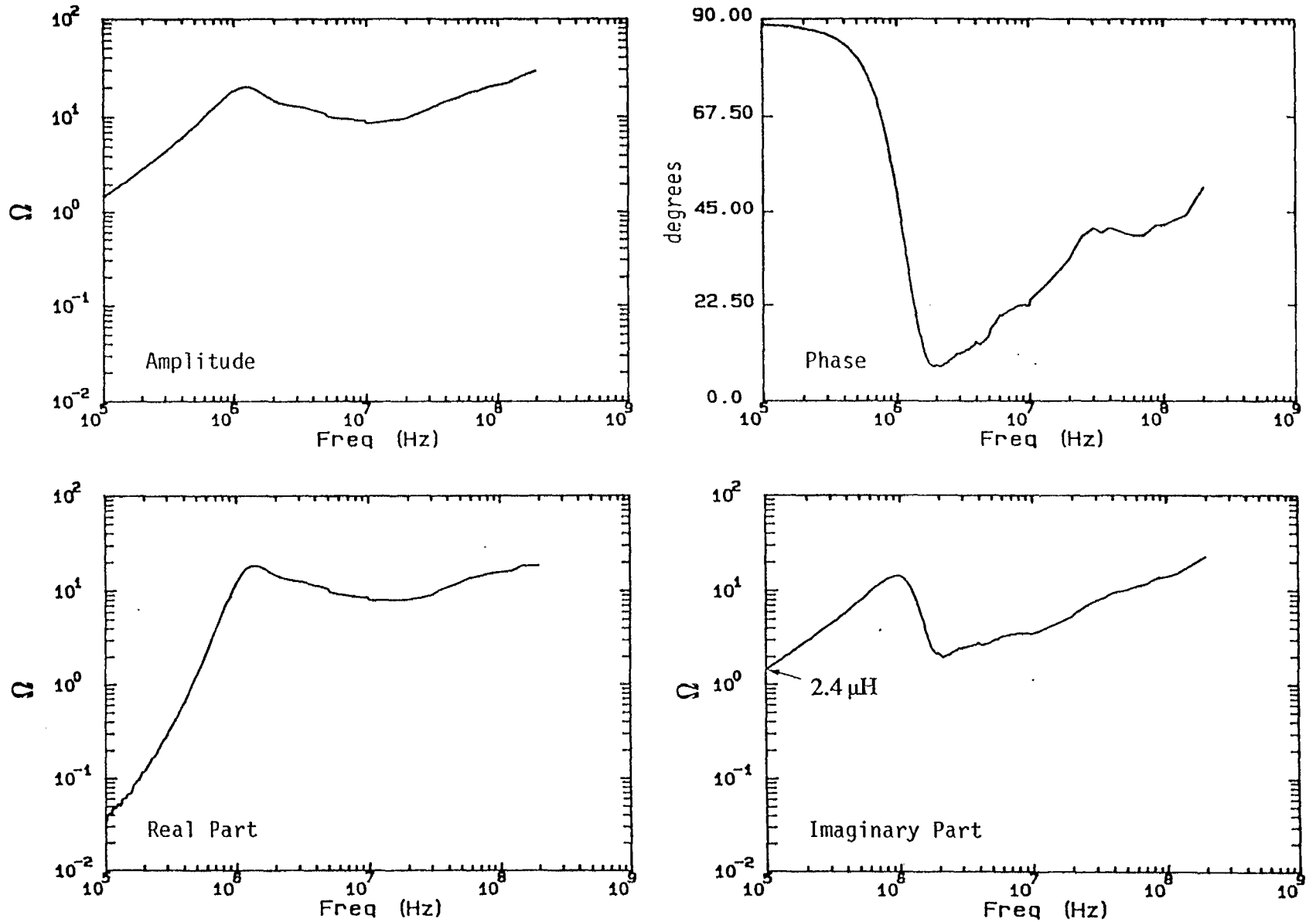

Figure 10. Measured impedance for one ferrite toroid made with material #77 (manganese-zinc).

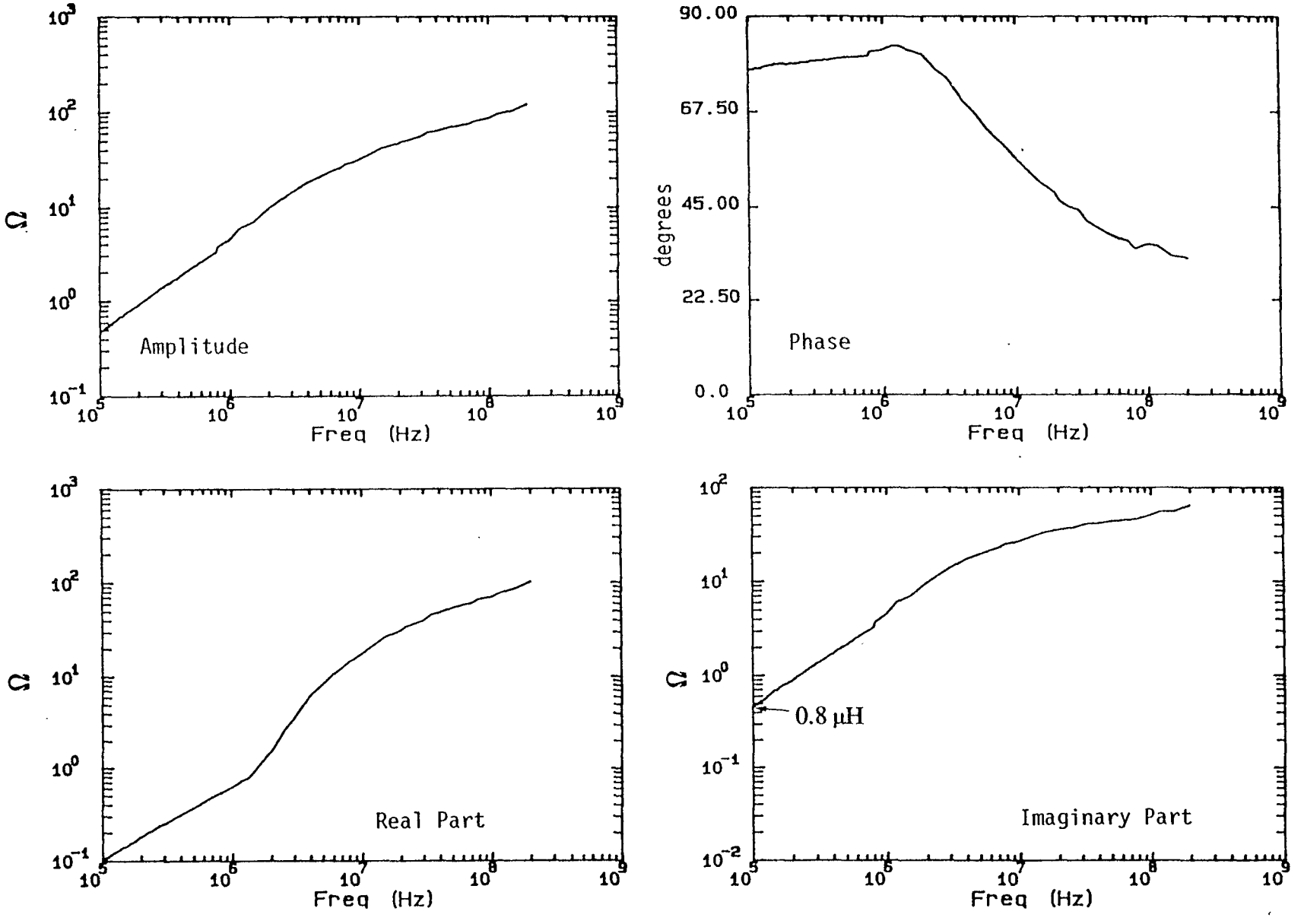

Figure 11. Measured impedance for one ferrite toroid made with material #43 (nickel-zinc).

elements. This effect is illustrated in Fig. 9 where the magnetic induction calculated at (0, 3, 20) in the absence of the ferrites is contrasted with that measured under load condition. One can notice that as a result of loading, the antenna resonances are shifted down in frequency, and are attenuated and broadened. A more comprehensive and quantitative description of the field properties with ferrite loading is presented in Sec. 4, where measured data are analyzed and compared with calculations obtained from a simple mathematical model of the antenna behavior.

2.4 Antenna Input Impedance

The antenna input impedance was obtained from measurements of the reflection coefficient at the actual feed point, according to Eq. (1), and is presented in Fig. 12, displayed both as amplitude and phase and as real and imaginary part. Note the double peak, one around 400 kHz and the other around 900 kHz, with a small valley in between, which corresponds to a passage of the phase through zero three times. One can conclude that the first resonance point occurs roughly around 600 kHz; actually there are two resonances, slightly splitted. A second resonance takes place around 900 kHz, beyond which the behavior of the antenna is capacitive. It is shown that the input impedance is always higher than the characteristic impedance of the feeding cable (50 Ω), and a substantial mismatch occurs at the antenna apex, resulting in a reduced efficiency.

To minimize the impedance mismatch, a 50 Ω low induction resistor was connected in parallel with the antenna input gap, since time constraints did not allow us to try out a more refined matching device. Future effort should be directed to designing a matching network for this antenna which optimizes the radiated fields. The present design results in a lot of wasted energy into the resistor.

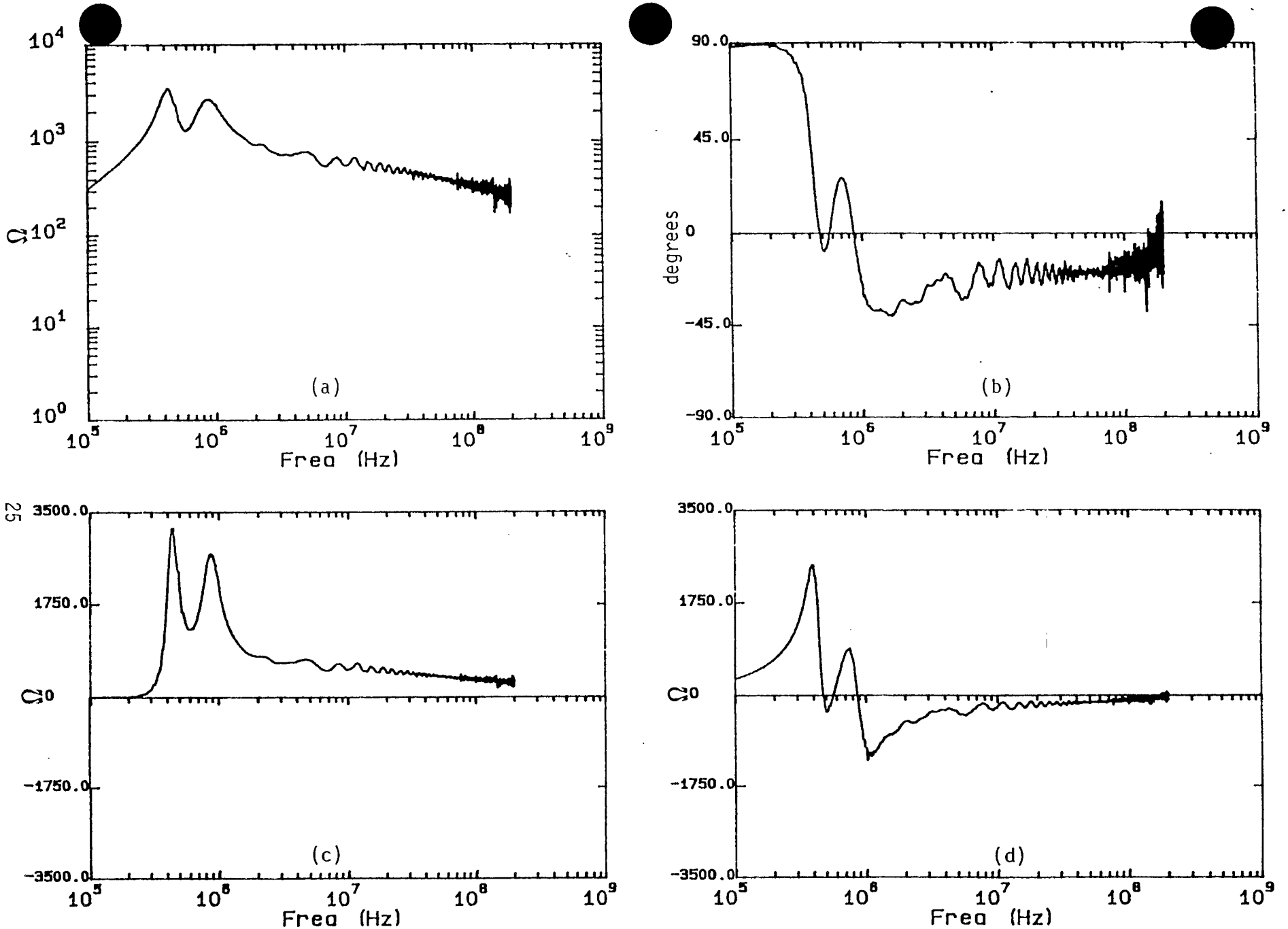

Figure 12. Antenna input impedance, displayed as (a) amplitude (b) phase (c) real part (d) imaginary part

3.0 MATHEMATICAL MODEL OF ANTENNA PERFORMANCE

The antenna is modeled by either a triangular loop or a semielliptical loop as illustrated in Figs. 6 and 7, and the Cartesian coordinate system shown there is used throughout this section. Note that the antenna is located in the plane xy, with the three vertices at ($\pm$b, 0, 0) and (0, h, 0), respectively. To determine the current our model does not differentiate between the two geometries. On the other hand the precise geometry is used when calculating fields.

3.1 Current Calculation - Perfectly Conducting Ground

At first let's assume that the ground is perfectly conducting. Then an image loop can be considered with the current flowing in the directions indicated in Fig. 13. For simplicity the loading impedance is assumed to be distributed uniformly along the antenna legs only; the value of the impedance per unit length Z_L is arrived at by using the following simple approach

$$Z_L(\omega) = \frac{N_1 Z_{43}(\omega) + N_2 Z_{77}(\omega)}{2L} \tag{9}$$

where Z_{43} and Z_{77} are the impedances of a single ferrite bead for material #43 and material #77, respectively, presented in Figs. 10 and 11 of Sec. 2.3, and L is the antenna leg given by $(h^2 + b^2)^{1/2}$. Additionally, N_1 and N_2 are the total numbers of such beads. Note that the model assumes that the distribution is along the antenna legs only and not along the base. This approximation rests on the fact that the base is very close to the ground so that in this model its current is neutralized by the correspondent image, as shown in Fig. 13, and the loop is reduced to a rhombus. Furthermore, the load provided by the material #77 beads is effective only at relatively low frequencies, say below a few MHz, above which the impedance becomes much smaller than that of material #43. Since the antenna is electrically small at low frequency, and the current does not change significantly along the loop, it does not matter where precisely the impedance load is located, for the attenuation introduced by the load will be roughly equally effective at suppressing the flow of current from one leg back to the other.

Under the above conditions, it has been shown [4] that for thin loops the longitudinal current I_s satisfies the following equation

$$\frac{\partial^2 I_s}{\partial_{s^2}} + k^2 \left(1 + i\frac{Z_L}{kZ_c}\right) I_s = \frac{ik}{Z_c} V_o[\delta(s-L) + \delta(s-3L)] \tag{10}$$

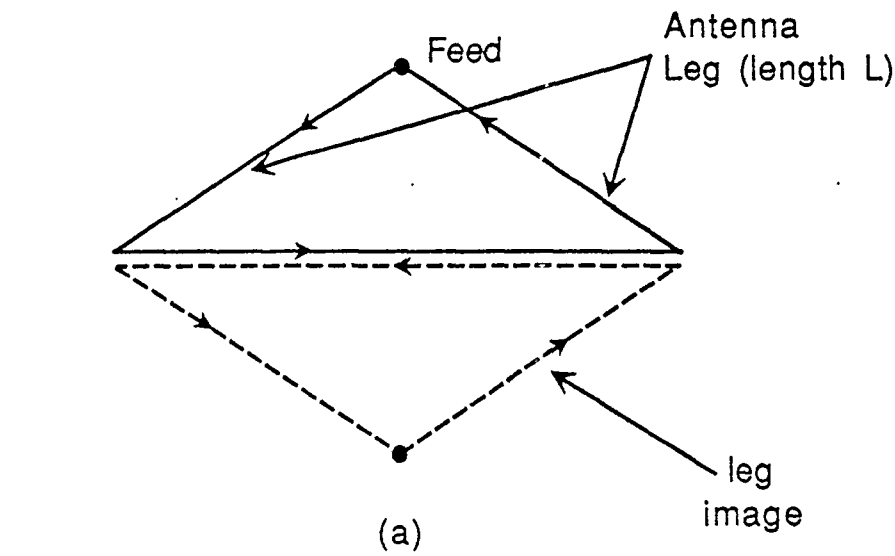

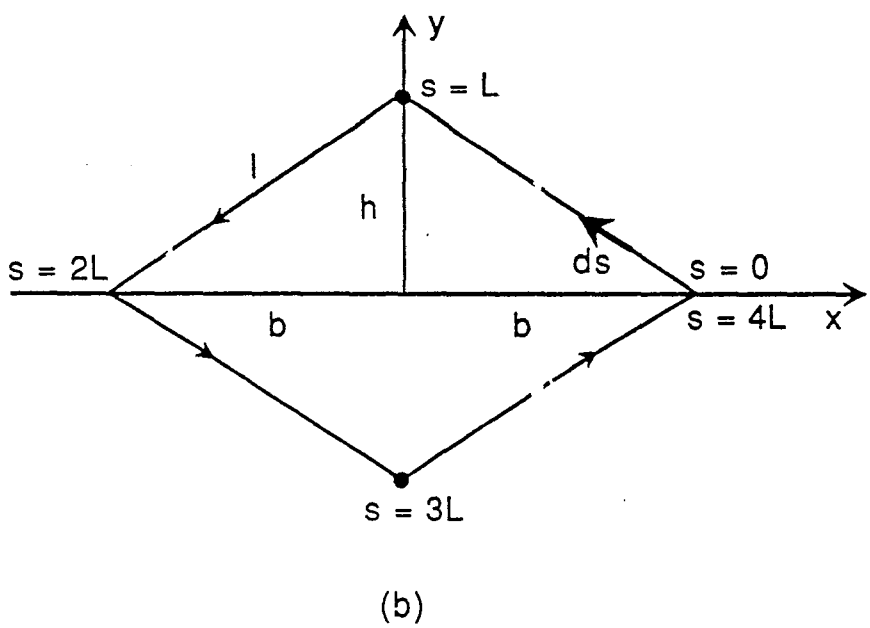

Figure 13. Geometrical model for the antenna describing the direction of the flow of current.
(a) both real loop and image are shown.
(b) loop effectively used in calculations (contribution from section on the ground is cancelled by its image).

where $k=2\pi/\lambda$ is the wave number, s is the arc along the loop starting at x = b, y = 0 (see Fig. 13), V_o is the source or the image strength in V/m, and

$$Z_c = \begin{cases} 60\ell n\left(\dfrac{2L}{\pi r}\right) & \dfrac{2kL}{\pi} \le 1 \\ -60\ell n(kr) & \dfrac{2kL}{\pi} \ge 1 \end{cases} \tag{11}$$

A time dependence $e^{-i\omega t}$ has been assumed throughout this chapter.

The boundary conditions for this problem are

$$I_s(2L^-) = I_s(2L^+), \quad I_s(4L^-) = I_s(0^+) \tag{12}$$

$$\int_{\text{across gap}} \frac{\partial^2}{\partial s} I_s ds = \frac{ikV_o}{Z_c} \qquad \text{for both source and image} \tag{13}$$

Introducing

$$\gamma = ik\sqrt{\left(1 - \frac{\text{Im}\{Z_L\}}{Z_c k}\right)^2 + \left(\frac{\text{Re}\{Z_L\}}{Z_c k}\right)^2} \cdot \exp\left\{i\frac{1}{2}\arctan\frac{\text{Re}\{Z_L\}}{Z_c k - \text{Im}\{Z_L\}}\right\} \tag{14}$$

the solution is

$$I_s(s) = \begin{cases} Ae^{\gamma(s-L)} + Be^{-\gamma(s-L)} & (x > 0, y > 0) \\ Be^{\gamma(s-L)} + Ae^{-\gamma(s-L)} & (x < 0, y > 0) \end{cases} \tag{15}$$

with

$$A = \frac{ikV_o e^{2\gamma L}}{2\gamma Z_c}\left(\frac{1}{1 - e^{2\gamma L}}\right) \tag{16}$$

$$B = Ae^{-2\gamma L} \tag{17}$$

Such current flows in the direction shown in Fig. 13, which is defined as the positive direction. The image is obtained by considering the symmetry about the plane z = 0.

From Eq. (14) one obtains for the velocity of propagation

$$v = \frac{c}{\sqrt{\left(1 - \frac{Im\{Z_L\}}{Z_c k}\right)^2 + \left(\frac{Re\{Z_L\}}{Z_c k}\right)^2} \cos\left\{\frac{1}{2}\arctan\left[\frac{Re\{Z_L\}}{kZ_c - Im\{Z_L\}}\right]\right\}} \tag{18}$$

Since the velocity v is lower than the speed of light in a vacuum, the wavelength $\lambda = v/f$ is lower than its correspondent in free space by the same amount. Because the antenna resonances occur when the length is an integer multiple of the wavelength in the medium, as a consequency of loading they are shifted to lower frequencies, In fact, for the first resonance one obtains

$$f_r = \frac{v}{4L} \sim 600\text{kHz} \tag{19}$$

Without loading it would be

$$f'_r = \frac{c}{4L} \sim 1.7\ \text{MHz} \tag{20}$$

3.2 Current Calculation - Lossy Ground Accounted For

A second alternative model was derived by assuming that the cable at the base of the triangle and the earth form a (lossy) transmission line, loaded periodically with ferrite beads, as shown schematically in Fig. 14. The effect of such transmission line on each antenna leg can be modeled as one lumped impedance positioned at $x = \pm b$, $y = 0$, resulting from the cumulative effect of the toroids and the length of transmission line, and calculated acording to the recursive relationship

$$Z(p+1) = Z(p) + Z_{77}$$

$$Z(p) = Z_g \frac{Z(p-1)\cosh\gamma_g v(p) - Z_g \sinh\gamma_g v(p)}{Z_g \cosh\gamma_g v(p) - Z(p-1)\sinh\gamma_g v(p)} \tag{21}$$

$$Z(0) = 0 \tag{22}$$

where v(p) is the separation between two ferrite material #77 beads, p is an integer varying between 1 and $N_2/2$ with $v(1) = \ell/2$, $v(p) = \ell$ $p>2$ and

$$Z_g = 60\ell n\left(\frac{2h_o}{r}\right)H \tag{23}$$

$$\gamma_g = ikH \tag{24}$$

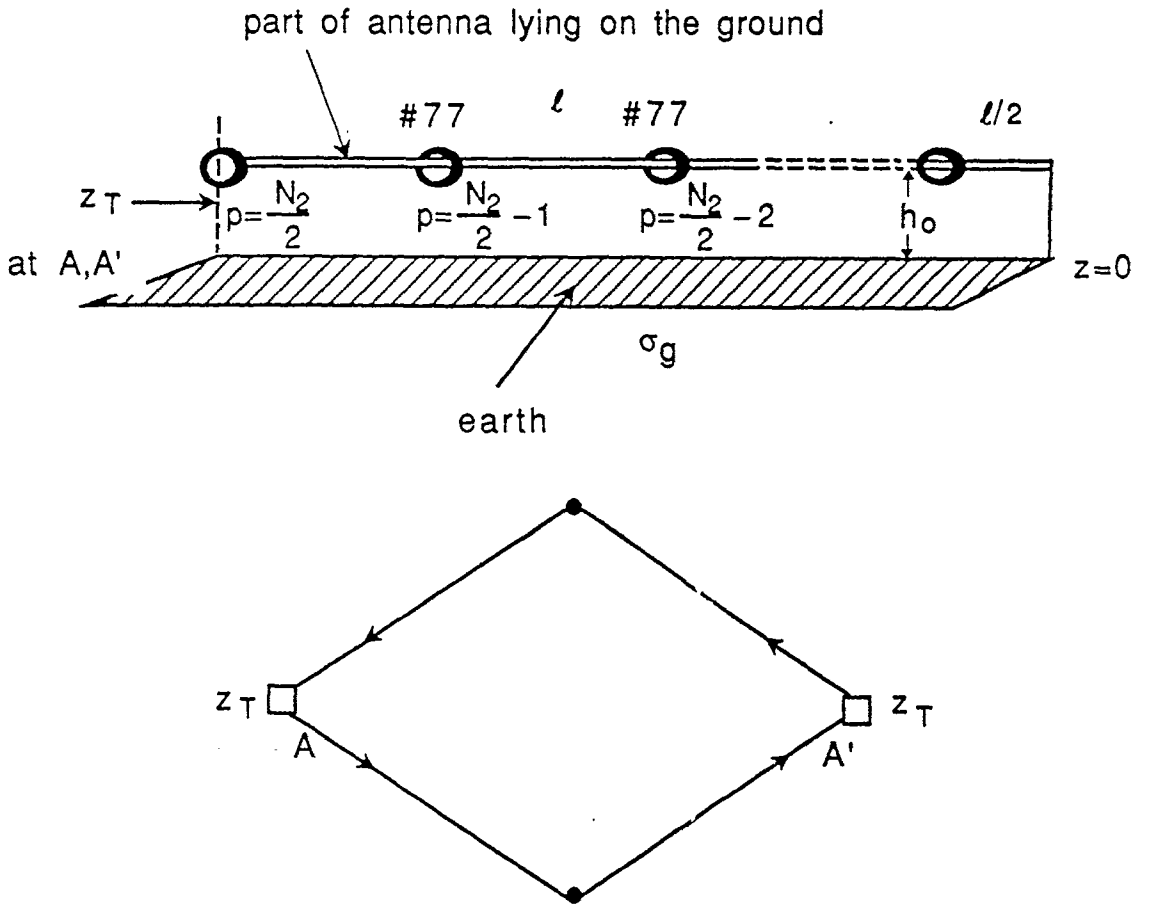

Figure 14. Model introduced to account for the presence of the real ground and the distribution of low frequency ferrite beads.
(a) "transmission line" formed between antenna coaxial cable and ground, loaded periodically with #77 ferrites
(b) the effect of such section of line is a lumped impedance at the points A, A'.

$$H = \left[1 + \left(\ell n(\frac{2h_o}{r}) \right)^{-1} \ell n \left(\frac{1 + \sqrt{-i2\pi f \mu_o \sigma_g h_o^2}}{\sqrt{-i2\pi f \mu_o \sigma_g h_o^2}} \right) \right]^{1/2} \tag{25}$$

are the characteristic impedance and propagation constant of the transmission line formed between the outer conductor of the antenna cable (of radius r) and the lossy ground (ground conductivity σ_g), the distance between the two being h_o, along the antenna base.

To solve for the current, the differential equation of Eq. (10) must still be satisfied with $Z_L = \frac{N_1 Z_{43}}{2L}$ and with the following boundary condition, instead of Eq. (12).

$$Z(N_2/2) I_s(0^+) = Z_T I_s(0^+) = V(0^+) \tag{26}$$

$$Z(N_2/2) I_s(2L^-) = Z_T I_s(2L^-) = V(2L^-) \tag{27}$$

The solution is formally similar to Eq. (15), but with A and B replaced by

$$A' = \frac{-ikV_o \Gamma_L}{\gamma Z_c} \frac{e^{+2\gamma L}}{1 + \Gamma_L e^{+2\gamma L}} \tag{28}$$

$$B' = \frac{-A'}{\Gamma_L} e^{-2\gamma L} \tag{29}$$

with $\Gamma_L = \frac{Z_T - Z_c}{Z_T + Z_c}$ being the reflection coefficient at the end of the legs, as indicated in Fig. 14.

Note that the image of the antenna legs is still considered in this approximation, and, additionally, the properties of the ground are accounted for in determining the effect of the ferrite loading along the base.

3.3 Potentials And Fields

Once the current is known one can calculate the vector and scalar potentials everywhere in space by using

$$\bar{A}(x,y,z) = \frac{\mu_o}{4\pi} \int_s I(x',y') \frac{e^{ik|\bar{r} - \bar{r}'|}}{|\bar{r} - \bar{r}'|} \, ds \tag{30}$$

and

$$\phi(x,y,z) = \frac{1}{4\pi\varepsilon_o}\int_s \rho(x',y')\frac{e^{ik|\bar{r}-\bar{r}'|}}{|\bar{r}-\bar{r}'|}\,ds \tag{31}$$

such that $i\omega\rho = \nabla\cdot I$. From Eqs. (23) and (24) $|\bar{r}-\bar{r}'| = \sqrt{(x-x')^2+(y-y')^2+z^2}$, where the primed coordinates indicate the source point and the unprimed coordinates indicate the observation point, and the integration is performed along the loop (antenna plus image) whose infinitesimal arc is indicated with $\overline{ds}$.

From Eqs. (30) and (31) the electromagnetic fields can be obtained as

$$\bar{E} = i\omega\bar{A} - \nabla\phi \tag{32}$$

and

$$\bar{B} = \nabla\times\bar{A} \tag{33}$$

For our particular geometry the explicit expressions of the field components are

$$E_v = i\omega A_v - \frac{\partial\phi}{\partial v} \tag{34}$$

where v indicates the generic Cartesian component x, y or z and

$$B_x = \frac{-\partial A_y}{\partial z},\quad B_y = \frac{\partial A_x}{\partial z},\quad B_z = \frac{\partial A_y}{\partial x} - \frac{\partial A_x}{\partial y} \tag{35}$$

The two Cartesian components of the potential A for the triangular loop are obtained as

$$A_x(x,y,z) = \frac{\mu_o}{4\pi}\int_o^b I_s(s)(ex_1 + ex_2 - ex_3 - ex_4)\,dx' \tag{36}$$

$$A_y(x,y,z) = \frac{\mu_o}{4\pi}\int_o^b I_s(s)(-ex_1 + ex_2 - ex_3 + ex_4)\tan\theta\,dx' \tag{37}$$

where θ = arctan h/b.

In Eqs. (36) and (37) for m = 1,...4 it is defined

$$ex_m = \exp(iksq_m)/sq_m \tag{38}$$

$$sq_m = \sqrt{(x-n_m x')^2 + (y-r_m[h-x'\tan\theta])^2 + z^2} \tag{39}$$

and

$$n_m = \begin{cases} +1 & m = 1,3 \\ -1 & m = 2,4 \end{cases} \qquad r_m = \begin{cases} +1 & m = 1,2 \\ -1 & m = 3,4 \end{cases} \tag{40}$$

The derivatives of A_x, A_y, and ϕ necessary to calculate Eq. (35) and (36) have been explicitly found as

$$\frac{\partial A_x}{\partial v} = \frac{\mu_o}{4\pi}\int_o^b I_s(s)\, dx' \cdot \left\{ ex_1 \frac{F_1 v}{sq_1}\left(ik - \frac{1}{sq_1}\right) + ex_2 \frac{F_2 v}{sq_2}\left(ik - \frac{1}{sq_2}\right) - ex_3 \frac{F_3 v}{sq_3}\left(ik - \frac{1}{sq_3}\right) - ex_4 \frac{F_4 v}{sq_4}\left(ik - \frac{1}{sq_4}\right) \right\} \tag{41}$$

The terms $F_m v$ in Eq. (41) stand for

$$\begin{aligned} F_1 x &= F_3 x = x - x' \\ F_2 x &= F_4 x = x + x' \\ F_1 y &= F_2 y = y - h + x' \tan\theta \\ F_3 y &= F_4 y = y + h - x' \tan\theta \\ F_m z &= z \;\forall m \end{aligned} \tag{42}$$

Note that $\partial A_y / \partial v$ can be found from Eq. (41) by changing the signs of the products containing ex_1 and ex_4, and multiplying by $\tan\theta$.

Concerning the derivative of the scalar potential ϕ, we found

$$\frac{\partial \phi}{\partial v} = \frac{1}{4\pi\varepsilon_o}\int_o^b \frac{1}{i\omega}\,\frac{\partial I_s}{\partial s}\sqrt{1+\tan^2\theta}\, dx' \cdot \left\{ +ex_1 \frac{F_1 v}{sq_1}\left(ik - \frac{1}{sq_1}\right) - ex_2 \frac{F_2 v}{sq_2}\left(ik - \frac{1}{sq_2}\right) - ex_3 \frac{F_3 v}{sq_3}\left(ik - \frac{1}{sq_3}\right) + ex_4 \frac{F_4 v}{sq_4}\left(ik - \frac{1}{sq_4}\right) \right\} \tag{43}$$

Alternatively, for the elliptical geometry, by letting x' = a cosv', y' = a' sinv', we obtained

$$A_x(x,y,z) = \frac{\mu_o}{4\pi}\int_o^b I_s(s)\,(ex_1 + ex_2 - ex_3 - ex_4)\sqrt{1-\cos^2 v'/\xi_o^2}\, dx' \tag{44}$$

$$A_y(x,y,z) = \frac{\mu_o}{4\pi}\int_o^b I_s(s)\,(-ex_1 + ex_2 - ex_3 + ex_4)\frac{x'}{y'}\sqrt{1-\cos^2 v'/\xi_o^2}\, dx' \tag{45}$$

With the expression in Eq. (39) changed as

$$sq_m = \sqrt{(x - n_m a\cos v')^2 + (y - r_m a'\sin v')^2 + z^2} \tag{46}$$

$$\frac{\partial A_x}{\partial v} = \frac{\mu_o}{4\pi}\int_o^b I_s(s)\sqrt{1-\cos^2 v'/\xi_o^2}\, dx'\left\{ex_1\frac{F_1 v}{sq_1}(ik - \frac{1}{sq_1})\right.$$

$$\left. + ex_2\frac{F_2 v}{sq_2}(ik - \frac{1}{sq_2}) - ex_3\frac{F_3 v}{sq_3}(ik - \frac{1}{sq_3}) - ex_4\frac{F_4 v}{sq_4}(ik - \frac{1}{sq_4})\right\} \tag{47}$$

In Eq. (42) the following changes need to be made

$$F_1 x = F_3 x = x - a\cos v'$$

$$F_2 x = F_4 x = x + a\cos v'$$

$$F_1 y = F_2 y = y - a'\sin v' \tag{48}$$

$$F_3 y = F_4 y = y + a'\sin v' \tag{49}$$

$$\frac{\partial \phi}{\partial v} = \frac{1}{4\pi\varepsilon_o}\int_o^b \frac{1}{i\omega}\,\frac{\partial I_s}{\partial s}\sqrt{1-\cos^2 v'/\xi_o^2}\,\frac{dx'}{\sin v'}\left\{-ex_1\frac{F_1 v}{sq_1}\,(ik - \frac{1}{sq_1})\right.$$

$$\left. + ex_2\frac{F_2 v}{sq_2}(ik - \frac{1}{sq_2}) + ex_3\frac{F_3 v}{sq_3}(ik - \frac{1}{sq_3}) - ex_4\frac{F_4 v}{sq_4}(ik\frac{1}{sq_4})\right\}$$

where v' is related to the arc lengths of the ellipse by

$$s(v) = a\int_v^{\pi/2}\sqrt{1-\cos^2 v'/\xi_o^2}\, dv' \tag{50}$$

and $\xi_o = 1/\sqrt{1-(a'/a)^2}$.

4.0 COMPARISON BETWEEN MEASUREMENTS AND CALCULATIONS

4.1 Available Measurements

This concept was first demonstrated at Kirtland in November 1990, in the triangular geometry, using the existing Achilles III poles as support structure. The scheme of the instrumentation set up is illustrated in Fig. 5. The signal from the 3577 Network analyzer is transmitted through coaxial cable and fed first to a power splitter, then to a 46 dB (nominal) power amplifier and finally connected to the 7/8" Heliax cable constituting the FFCW illuminator. The output of the power splitter was connected back to the reference input of the network analyzer via a fiber optic link. Therefore the reference measurement is the voltage corresponding to the power at the section immediately after the power splitter. For the elliptical configuration the power splitter was placed at the RF output of the network analyzer and therefore no fiber optic link was employed to connect its output back to the network analyzer reference channel.

A representative set of test point coordinates used for the field map of both antenna geometries is illustrated in Table 1. They are used to establish the comparisons with the values calculated with the models of Sec. 3. The field sensors were MGL-2, MGL-5 and ACD-4 for the measurements of $\dot{B}$ and $\dot{D}$, respectively, in the triangular geometry, whereas ACD-10 sensors were used for the elliptical geometry, instead of ACD-4S. Additionally, for the triangular configuration, the current was measured at four symmetric locations, two along the antenna legs and two along the base, all quite close to the ground. For practical purposes the coordinates of these points are $(\pm 39, 0, 0)$ and $(\pm 1, 0, 0)$. An SCP-1 current probe was used for these measurements.

4.2 Antenna Properties And Field Characteristics

4.2.1 Triangular Geometry

The first issue to be addressed is the determination of the radiated power, from the knowledge of the field levels. In the first demonstration test at Kirtland no measurement of antenna input impedance, or equivalently, input reflection coefficient was made. One can therefore only make a guess at what the incident power might have been by knowing its value after the power splitter from the reference measurement V_s, and multiplying it by the gain provided by the amplifier. Assuming that the loss along the cable connecting the amplifier output to the antenna gap is negligible it turns out that the incident power at low frequency can be estimated to have been P_{in} ~ 5W. At higher frequencies the cable connecting the 3577 to the power splitter introduces losses and the incident power is reduced to ~1.6W. However the exent of the reflection at the

Table 1.

Test Point Coordinates	Measured fields							
		B_x	B_y (T)	B_z		E_x	E_y (C/m^2)	E_z
0, 0, 0				X				
0, 0, -2				X				
0, 0, 20				X				
20, 0, 20				X				
0, 3, 20	X	X	X		X	X	X	
0, 3, 40	X	X	X		X	X	X	
-20, 3, 20	X	X	X		X	X	X	

Note: (1) (0, 0, -2) was used for the triangular configuration; (0, 0, 0) was used for the elliptical one

(2) (0, 3, 40) was used for the triangular configuration only

(3) the height above the ground was 3.3 m instead of 3m for the elliptical configuration

antenna gap is not known. To this purpose the mathematical model illustrated in Section 3 can be usefully employed to estimate what the radiated power might have been by calculating the fields at the available test points. Starting with Eq. (15) and in all the following field expressions it is noted that the current and field levels depend on the value V_0 of the source strength, which can be expressed as

$$V_o = \left[\frac{2\, P_{rad} |Z_i|^2}{re\{Z_i\}} \right]^{1/2} \tag{51}$$

where Z_i is the input impedance at the antenna gap and P_{rad} is the transmitted power, also at the antenna gap. In the absence of any measurements for Z_i, this was estimated by using the current of Eq. (15) itself, i.e. by taking V_0/I and then the parallel combination with the 50 Ω resistor was calculated. By numerically fitting the calculations with a constant value of P_{rad} which gives the best agreement with the measurements, it was found that about 0.1 W was actually radiated by the antenna.

Figures 15 through 20 illustrate the comparison between measurements and calculations, and the model of Secs. 3.1 and 3.3 is shown to be a good estimator over the entire frequency range of interest. Note that the current is modeled as though the loop has four legs, two actual ones and two images, and no portion of it were running along the ground. To calculate the current we assume that both species of toroids were distributed along the antenna legs resulting in a uniform impedance per unit length and also that the radiated power is constant. From Fig. 20b one can see that there is very good agreement up to 100 MHz and beyond that the measured current falls below the calculated one, perhaps because the radiated power drops. However the descrepancy might be due to some extent to the measurement set up.

On the other hand the model of Sec. 3.2 for the current does not give an equally good agreement between measured and caculated fields. For this reason we report, as an example, only the comparison at the test point (0, 3, 20), illustrated in Fig. 21. Various reasons could account for the discrepancy; for instance it is difficult to specify the line parameters for the section of transmission line above the ground and, additionally, the inclusion of the image in this case is no longer completely justified. However, note that the disagreement is not very drastic and is limited to frequencies below 10 MHz. Above that point the agreement is just as good as with the other model. It must also be remembered that the measured data are themselves not very reliable at low frequencies because of the small values of the derivative signals measured by the sensors. Such values could be in the noise of the network analyzer.

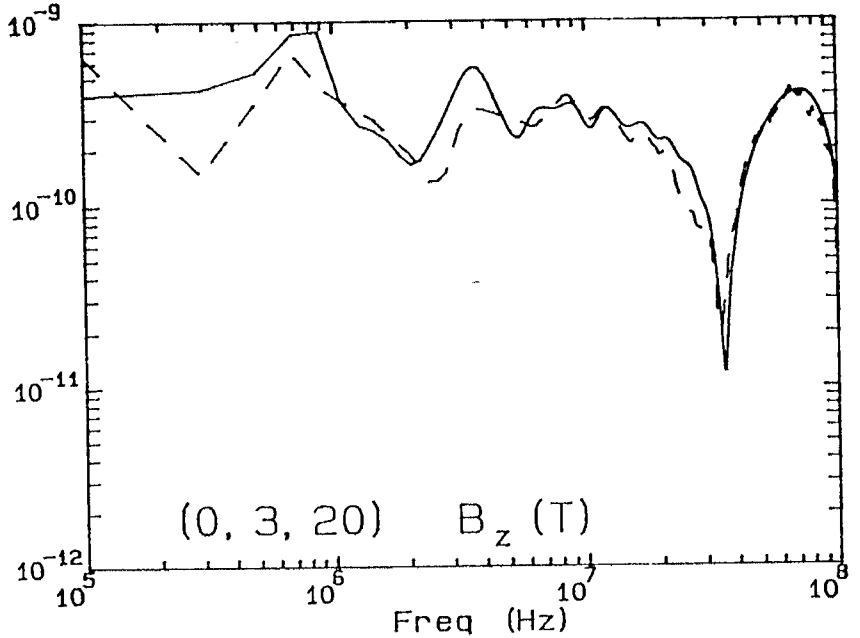

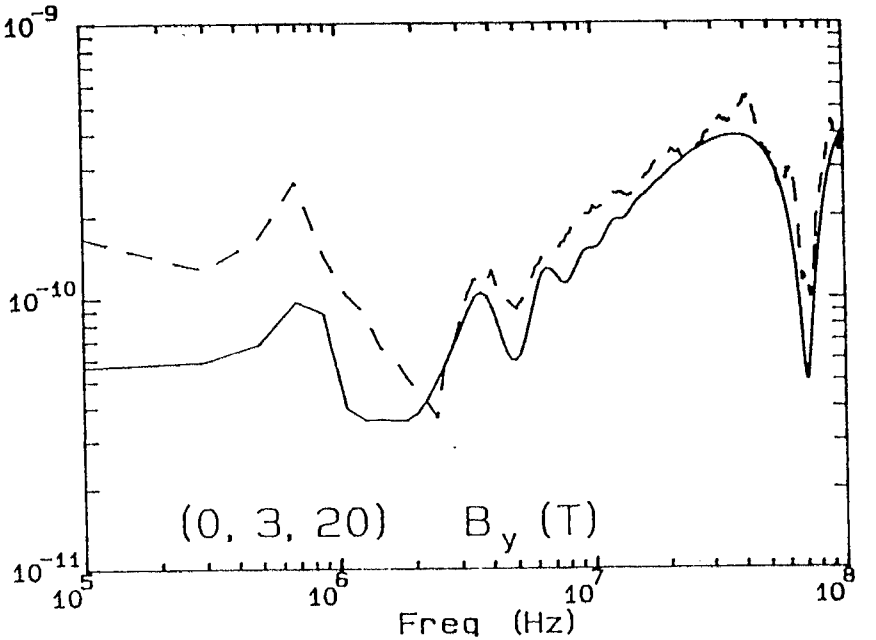

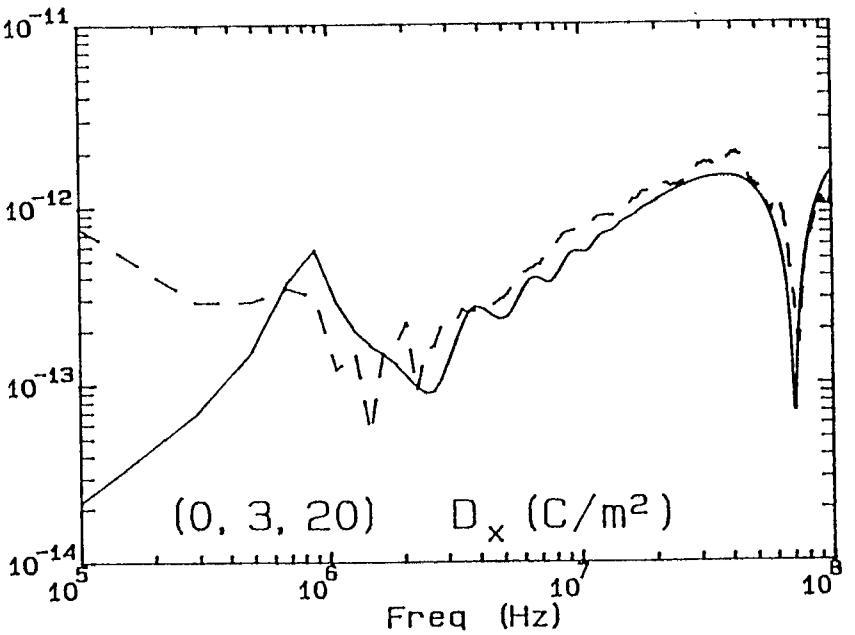

Calc.

Meas.

Triangular Geometry

Figure 15a. Comparison between model calculations (Secs. 3.1 and 3.3) and measurements at (0, 3, 20). The logarithmic frequency scale emphasizes the low frequencies.

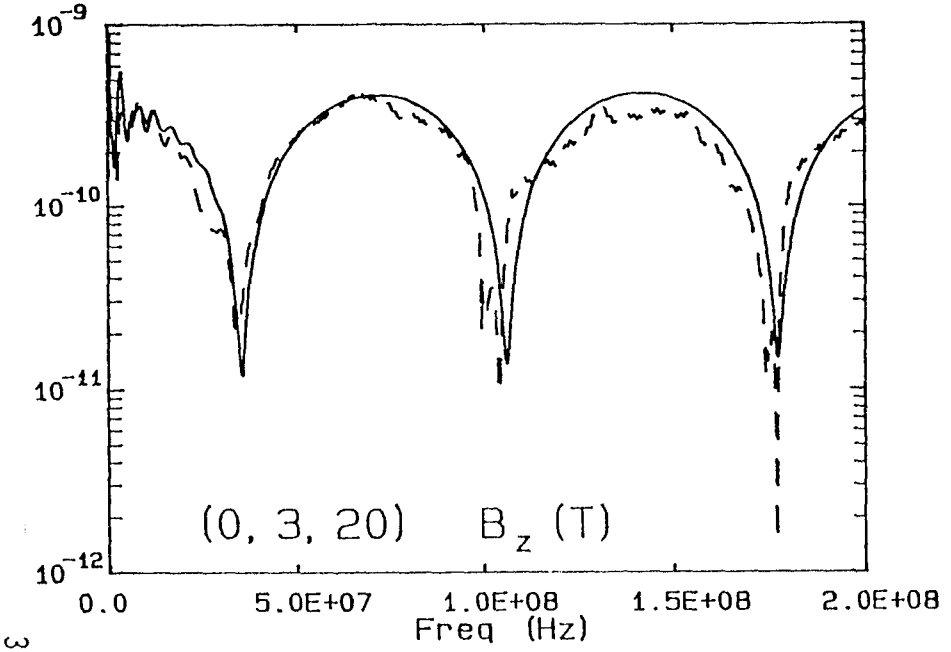

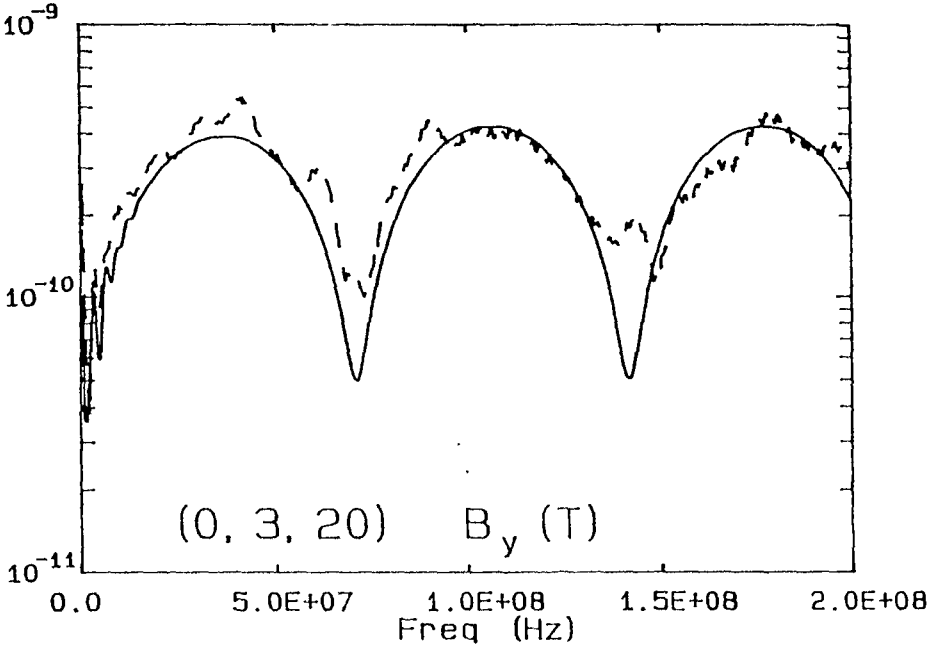

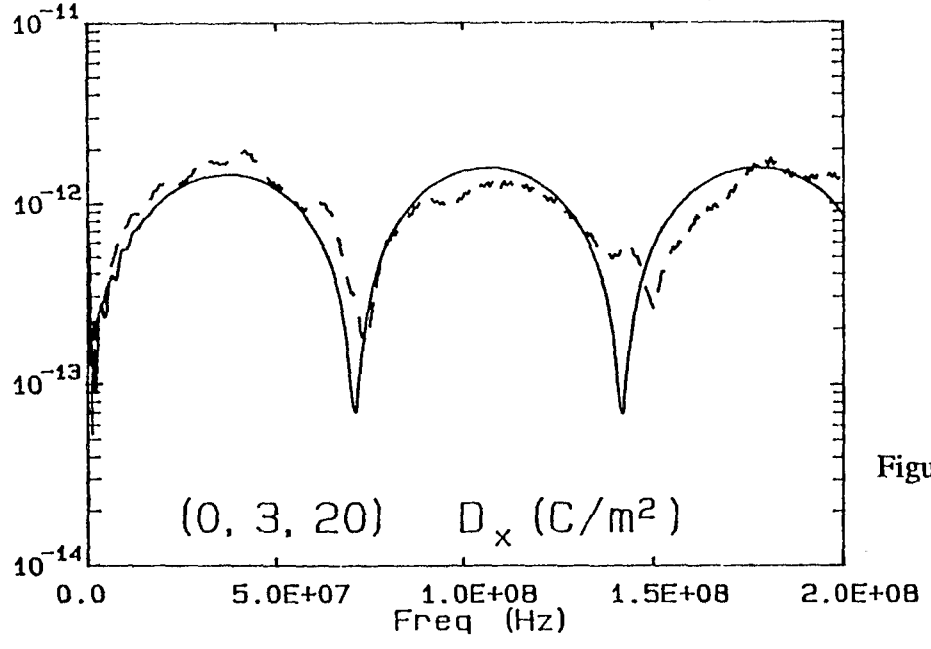

Calc.

Meas.

Triangular Geometry

Figure 15b. Comparison between model calculations (Secs. 3.1 and 3.3) and measurements at (0, 3, 20). The linear frequency scale emphasizes the high frequencies.

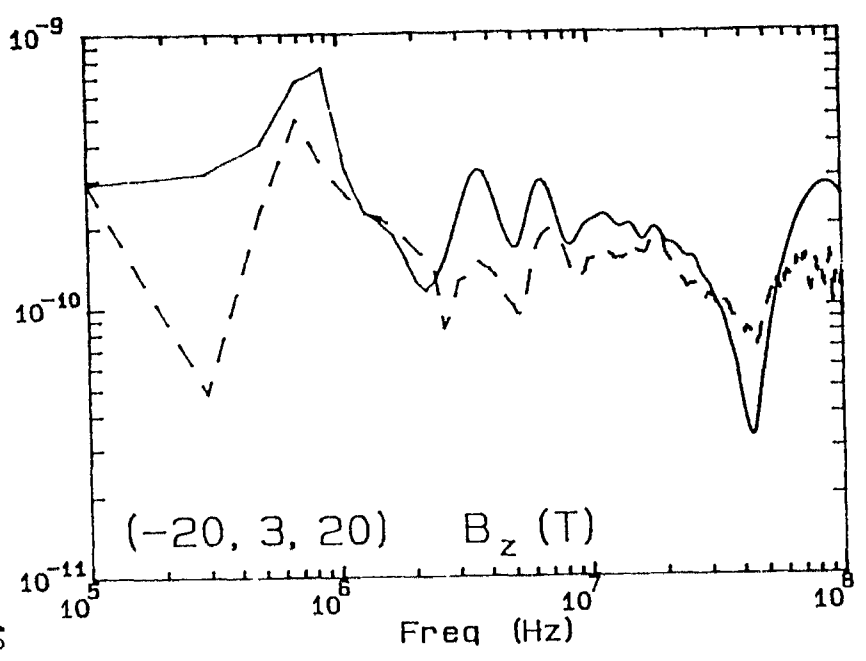

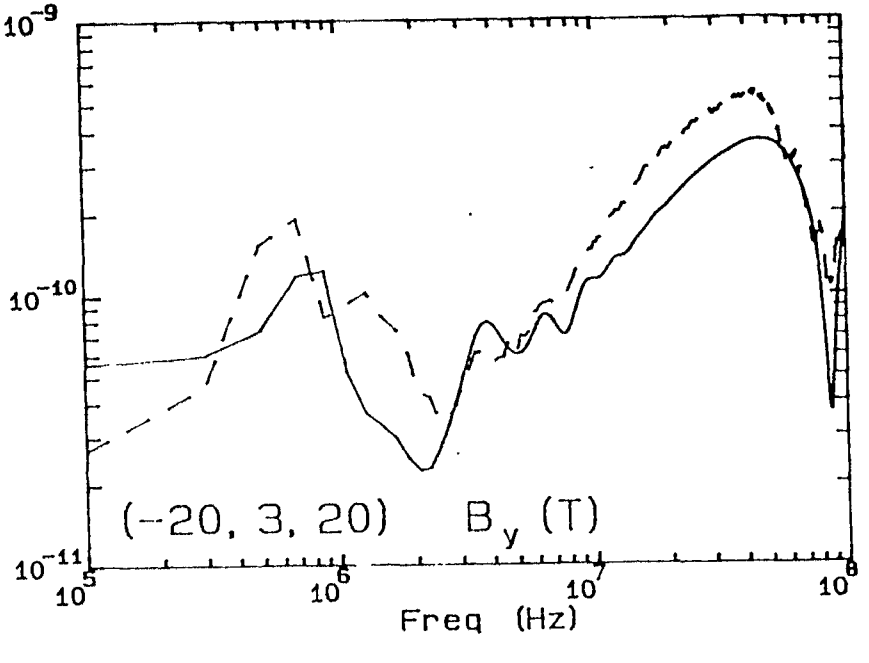

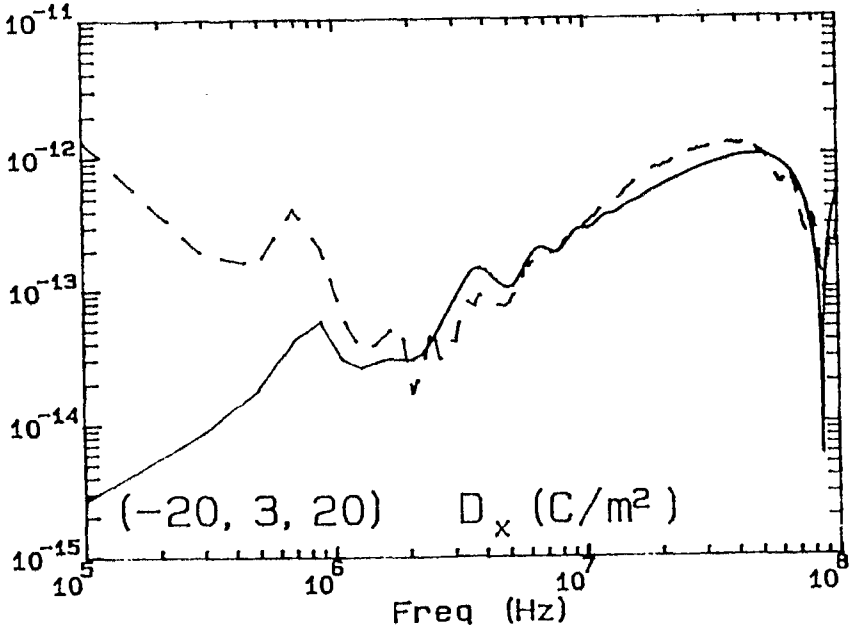

Calc.

Meas.

Triangular Geometry

Figure 16a. Comparison between model calculations (Secs. 3.1 and 3.3) and measurements at (-20, 3, 20). The logarithmic frequency scale emphasizes the low frequencies.

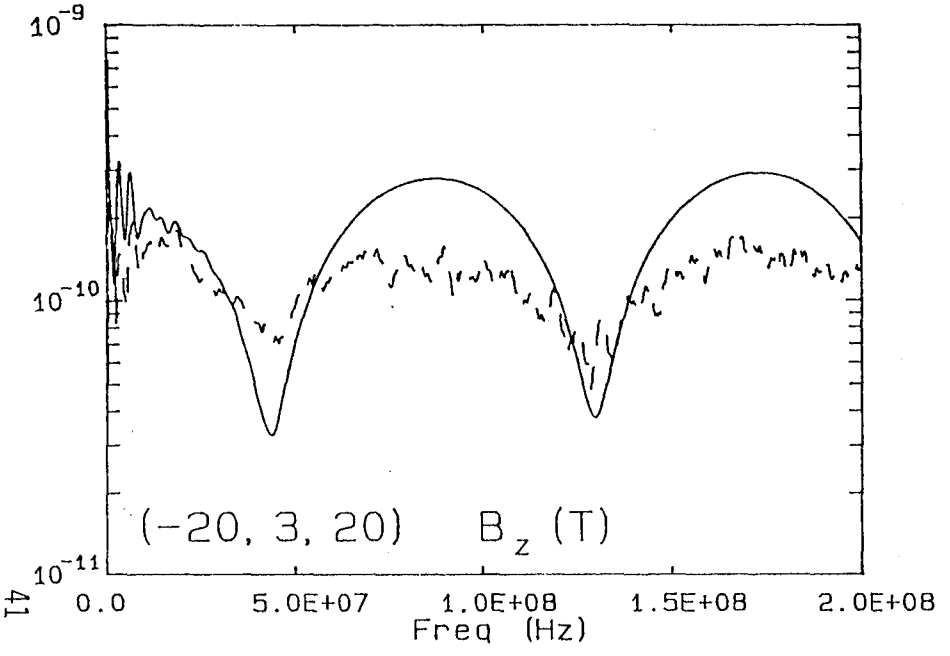

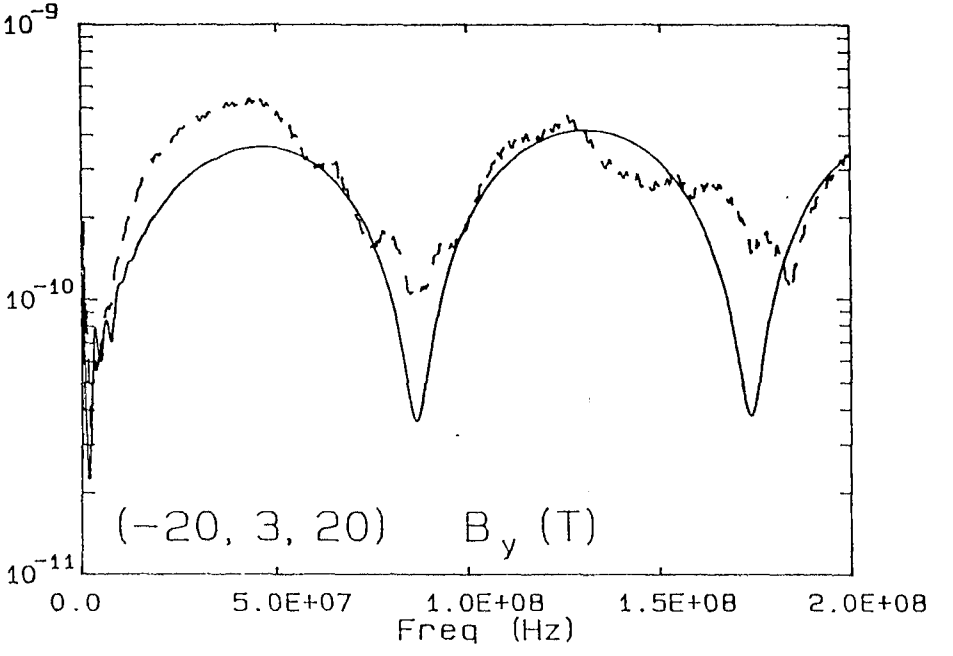

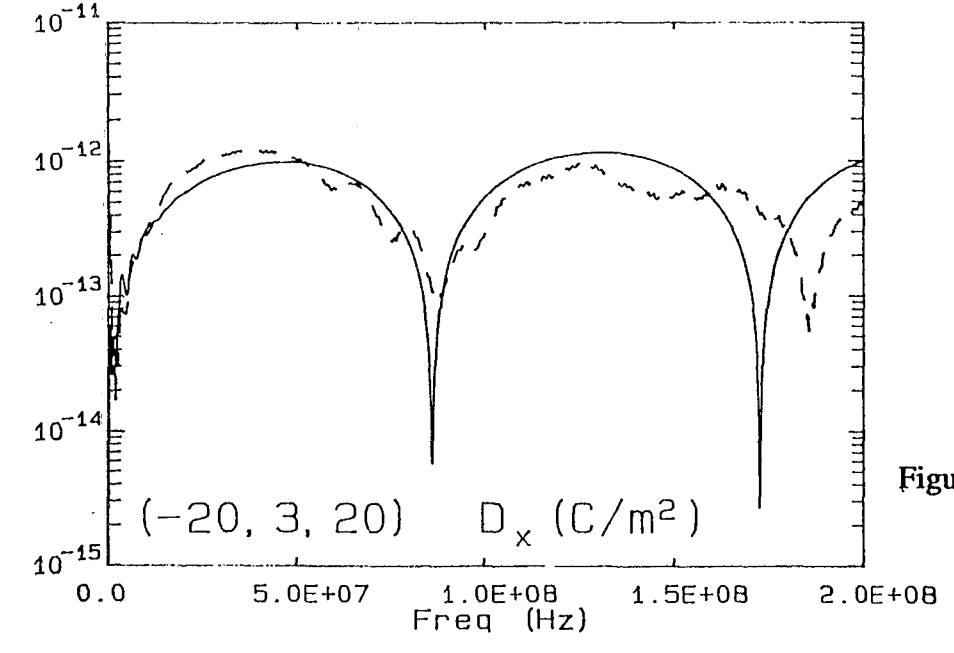

——— Calc.

– – – – – Meas.

Triangular Geometry

Figure 16b. Comparison between model calculations (Secs. 3.1 and 3.3) and measurements at (-20, 3, 20). The linear frequency scale emphasizes the low frequencies.

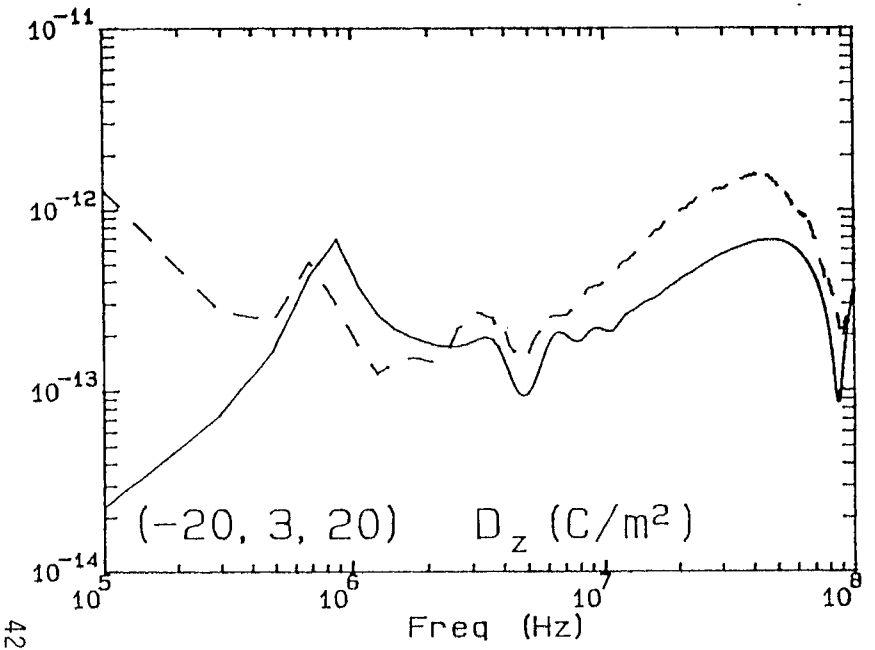

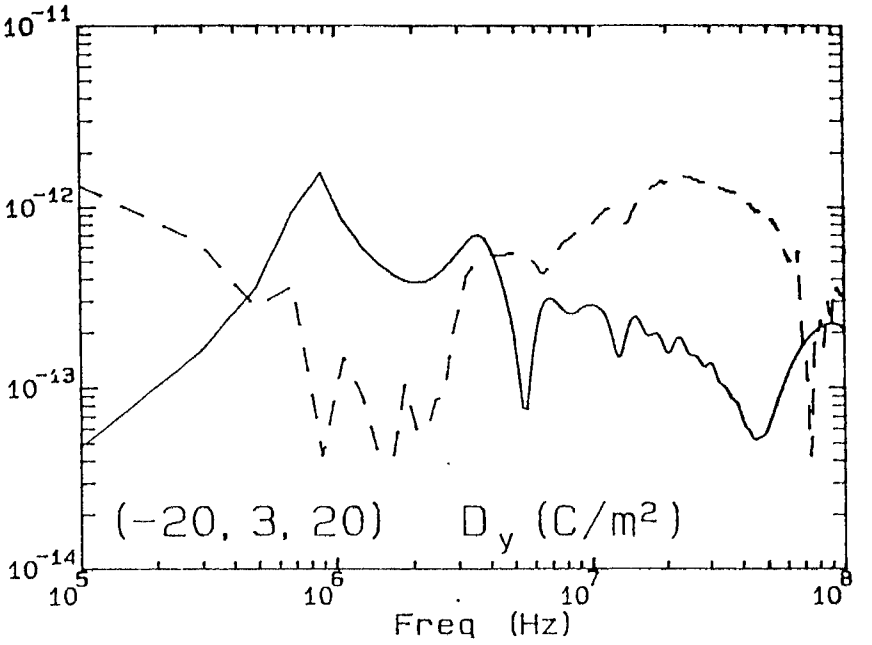

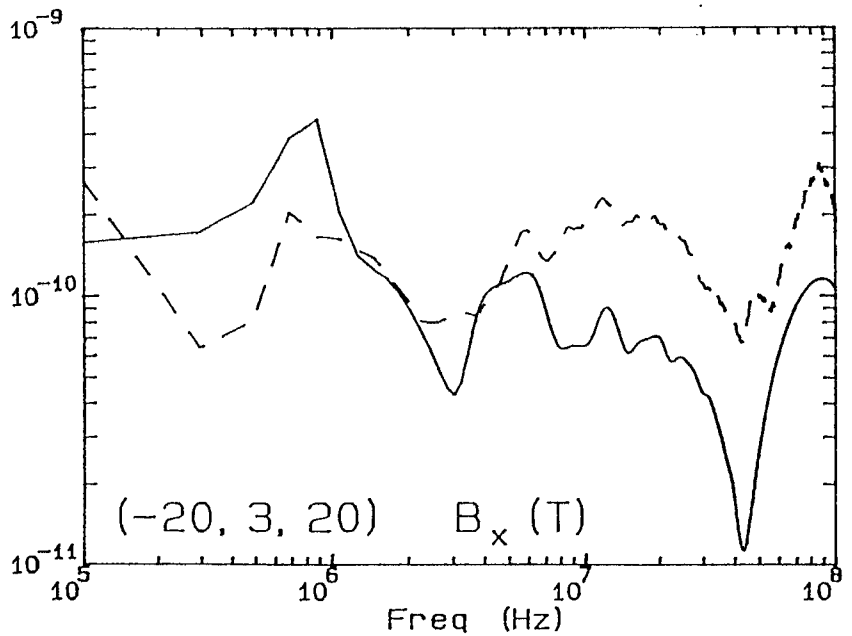

Calc.
Meas.
Triangular Geometry

Figure 17a. Comparison between model calculations (Secs. 3.1 and 3.3) and measurements at (-20, 3, 20). The logarithmic frequency scale emphasizes the low frequencies.

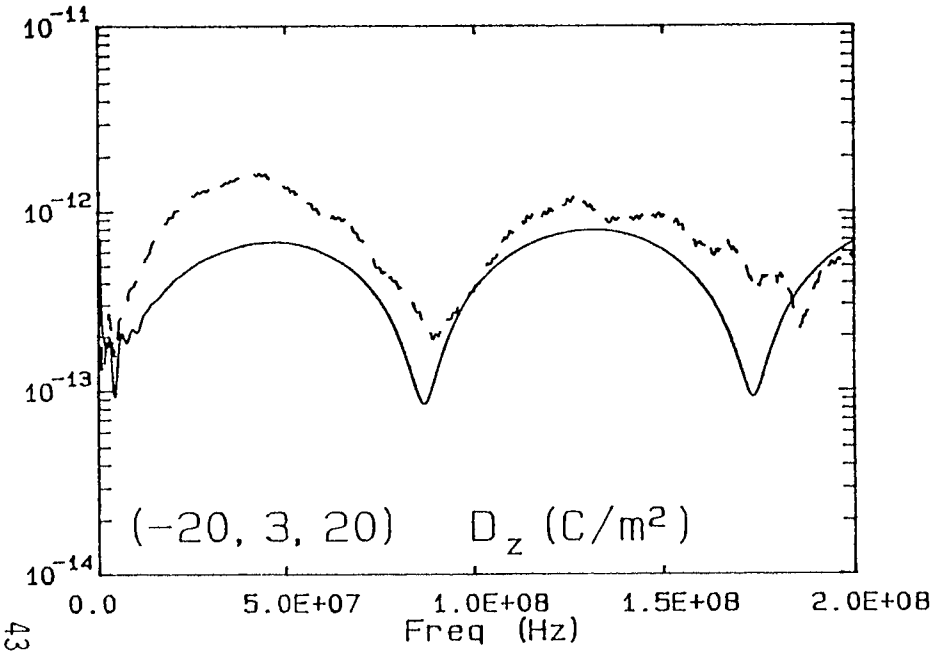

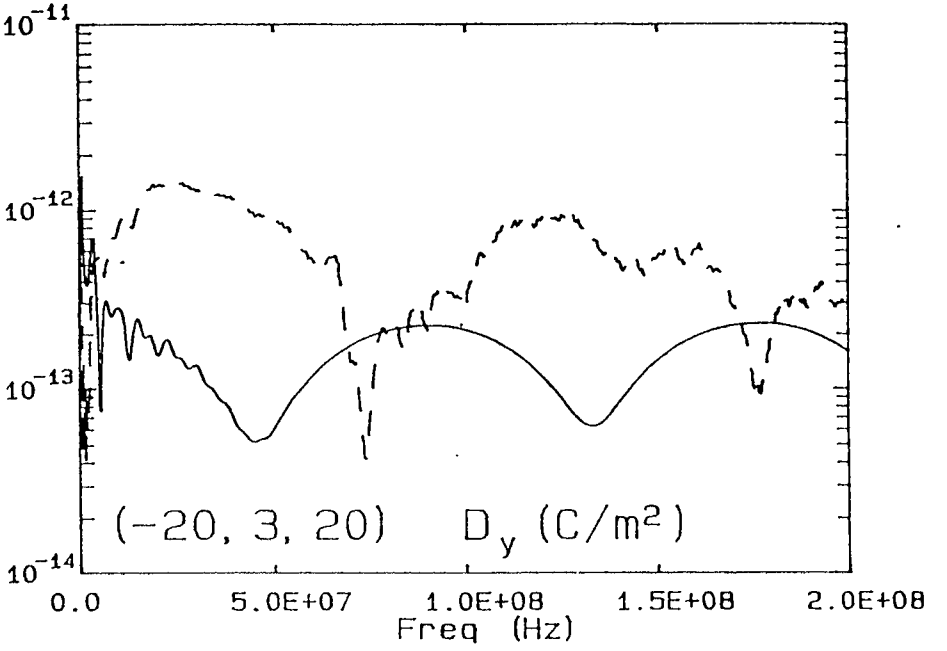

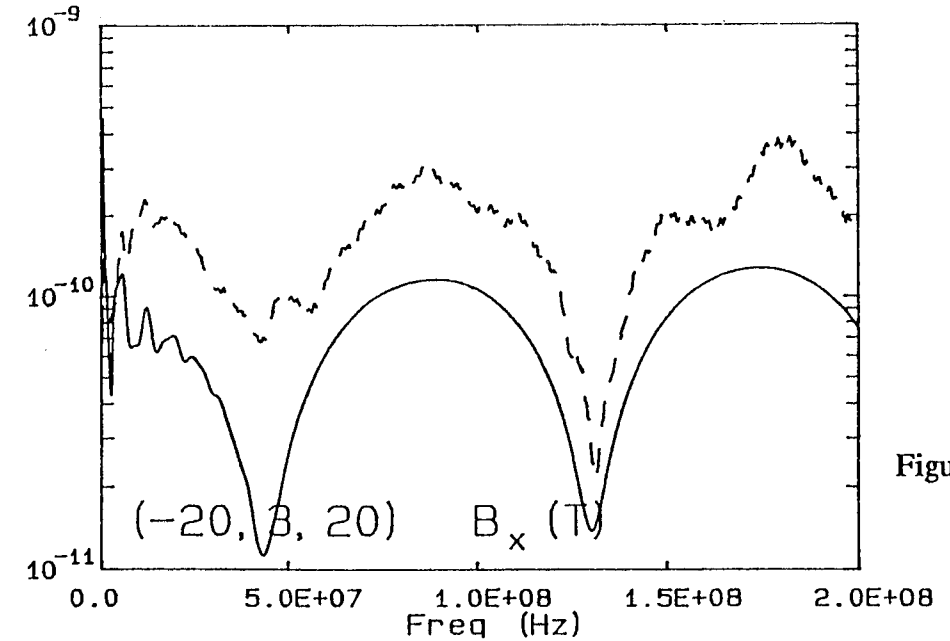

Calc.

Meas.

Triangular Geometry

Figure 17b. Comparison between model calculations (Secs. 3.1 and 3.3) and measurements at (-20, 3, 20). The linear frequency scale emphasizes the low frequencies.

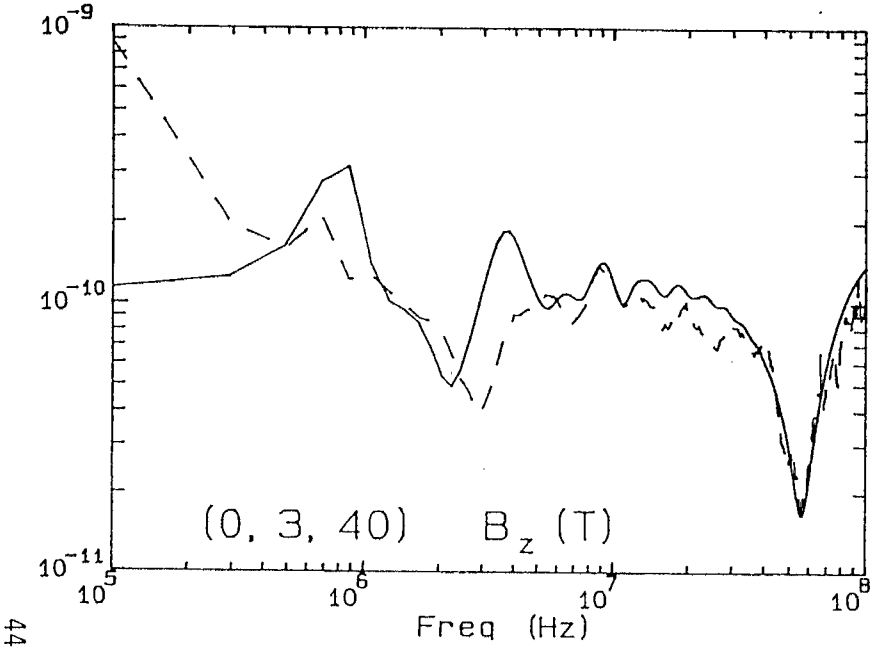

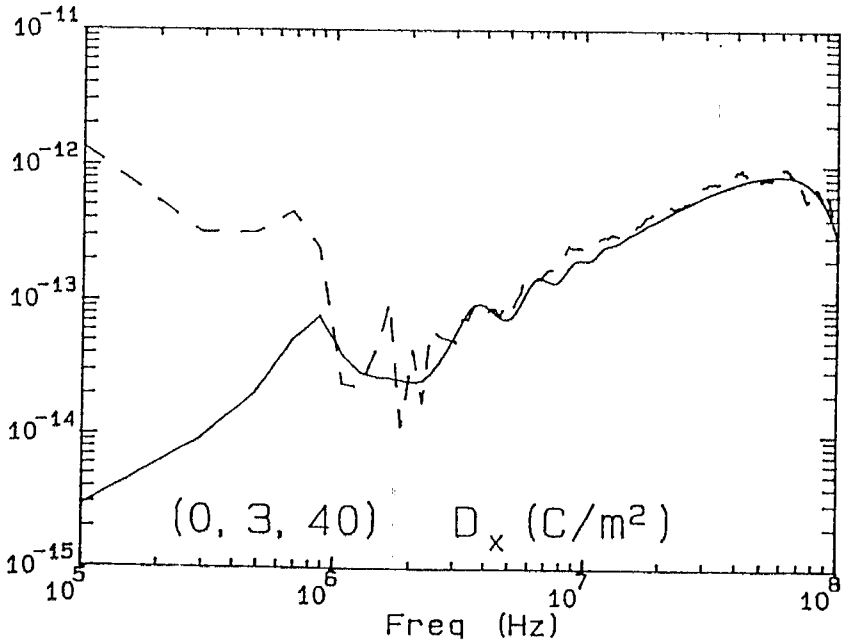

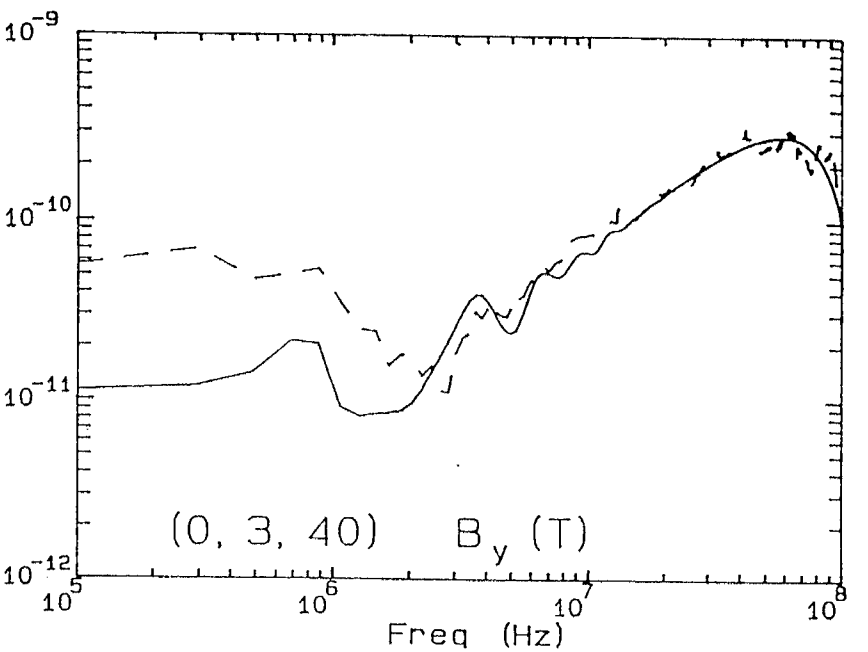

Calc.
Meas.

Triangular Geometry

Figure 18a. Comparison between model calculations (Secs. 3.1 and 3.3) and measurements at (0, 3, 40). The logarithmic frequency scale emphasizes the low frequencies.

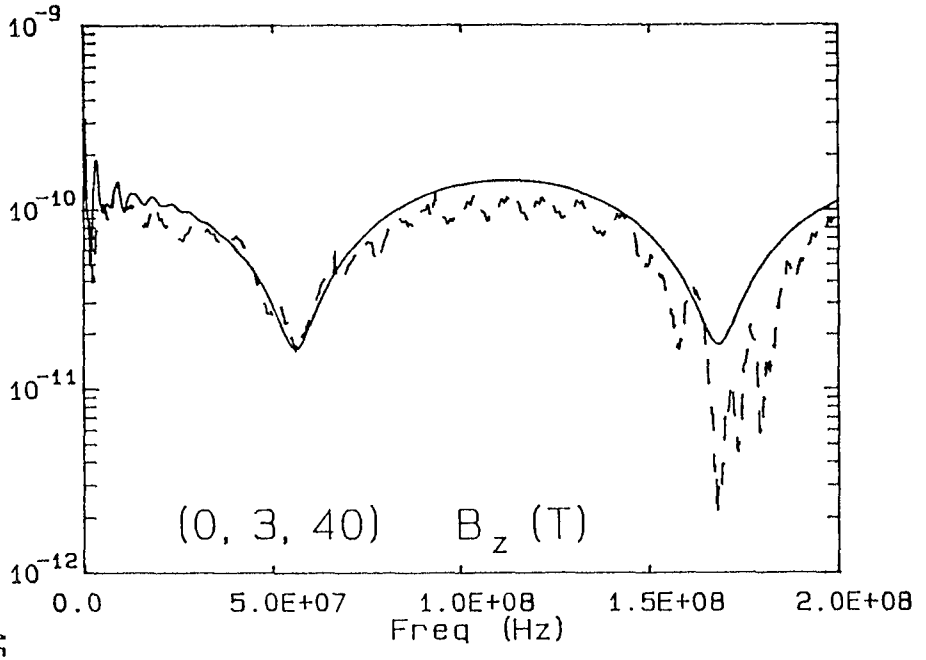

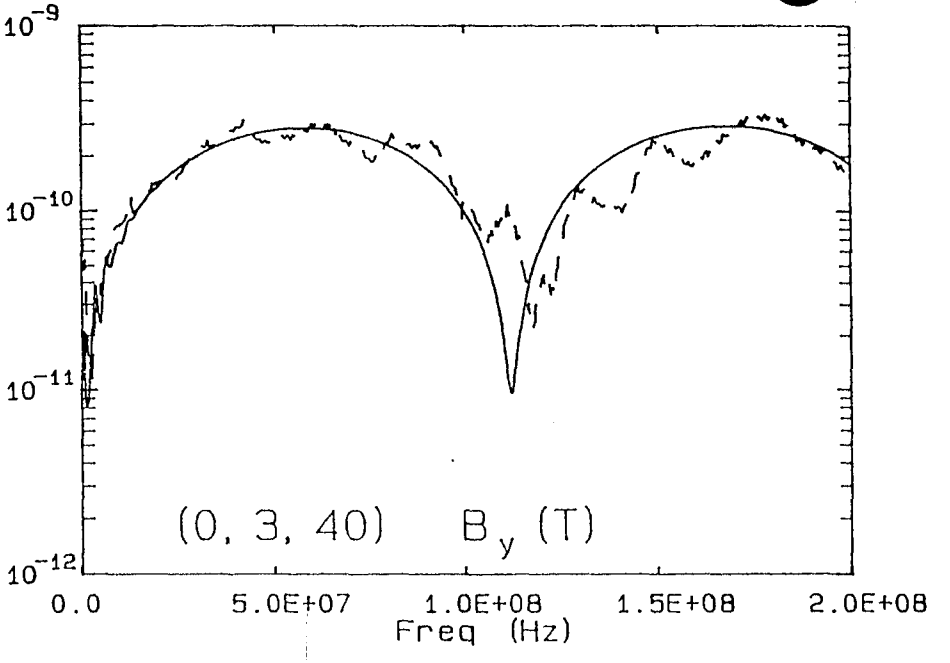

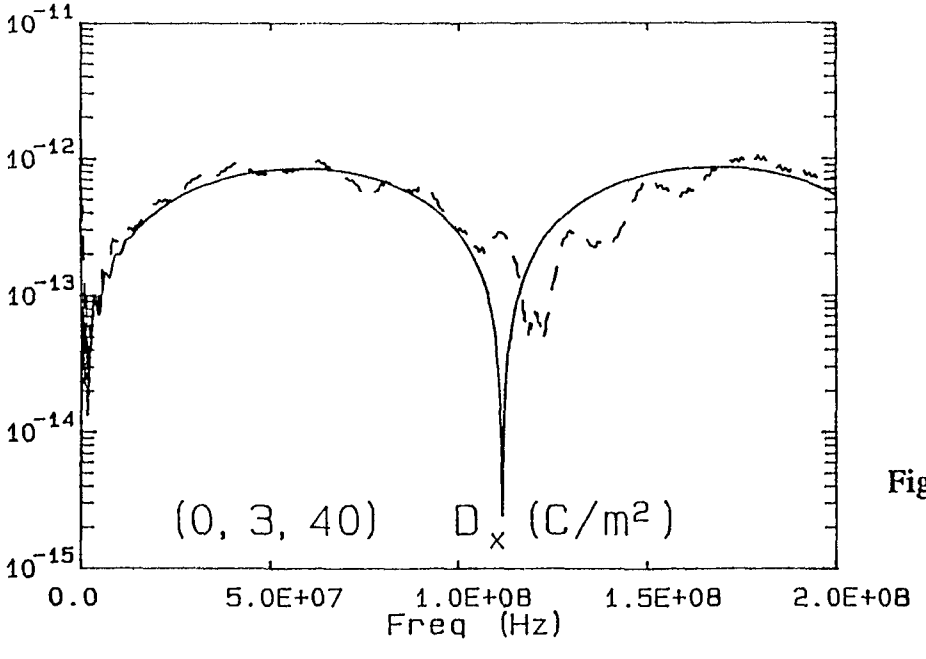

Calc.

Meas.

Triangular Geometry

Figure 18b. Comparison between model calculations (Secs. 3.1 and 3.3) and measurements at (0, 3, 40). The linear frequency scale emphasizes the low frequencies.

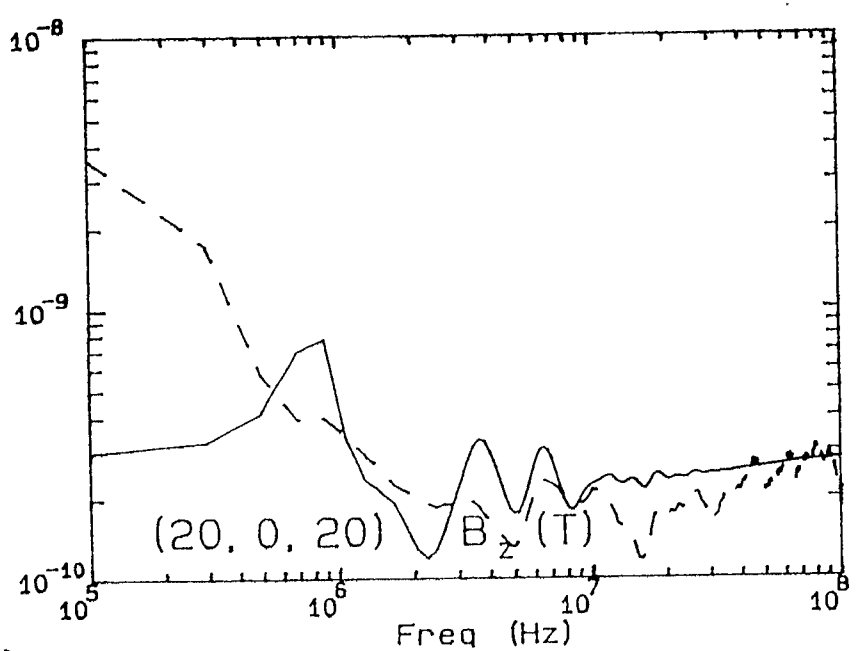

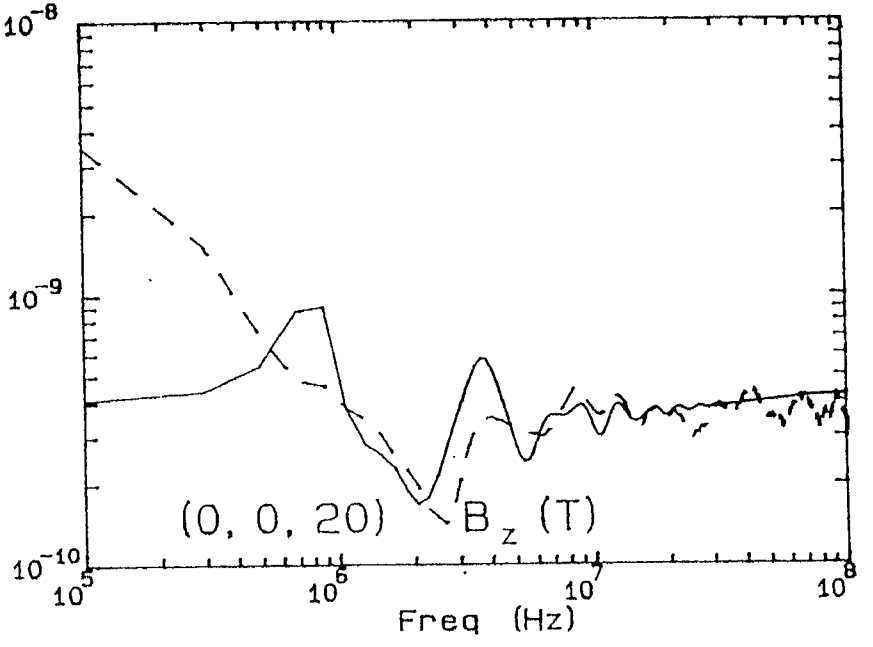

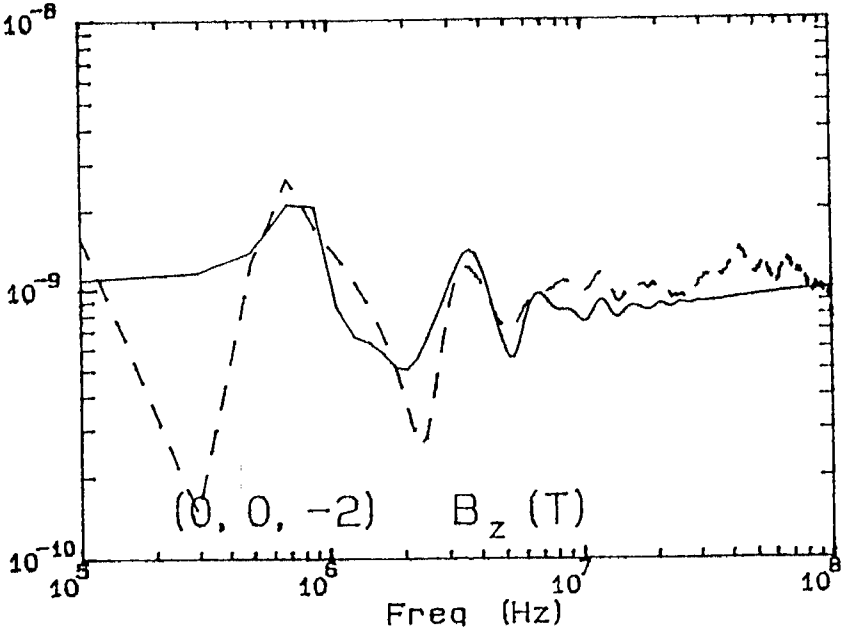

Calc.

Meas.

Elliptical Geometry

Figure 19a. Comparison between model calculations (Secs. 3.1 and 3.3) and measurements at (20, 0, 20), (0, 0, 20), and (0, 0, -2). The logarithmic frequency scale emphasizes the low frequencies.

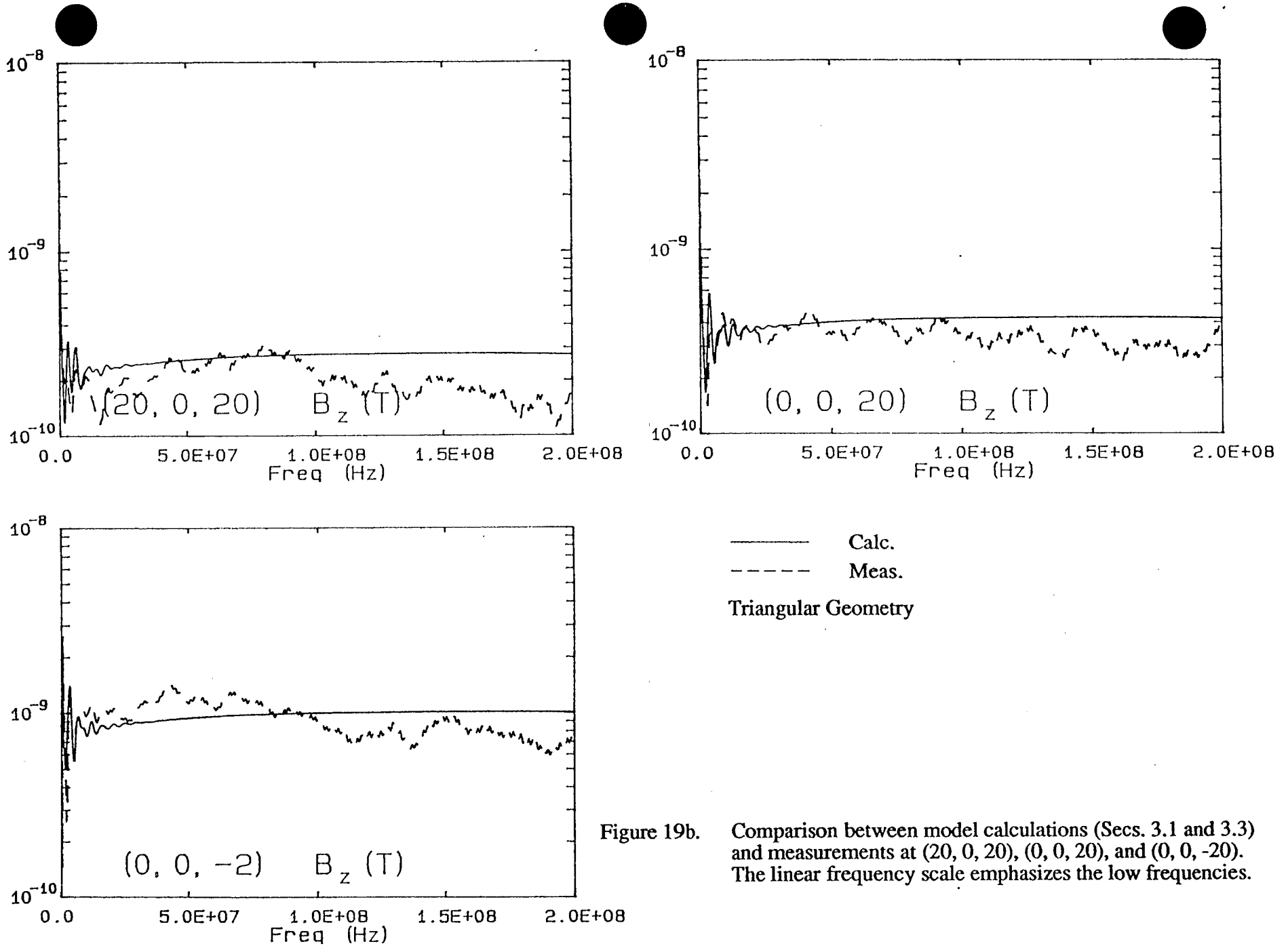

Figure 19b. Comparison between model calculations (Secs. 3.1 and 3.3) and measurements at (20, 0, 20), (0, 0, 20), and (0, 0, -20). The linear frequency scale emphasizes the low frequencies.

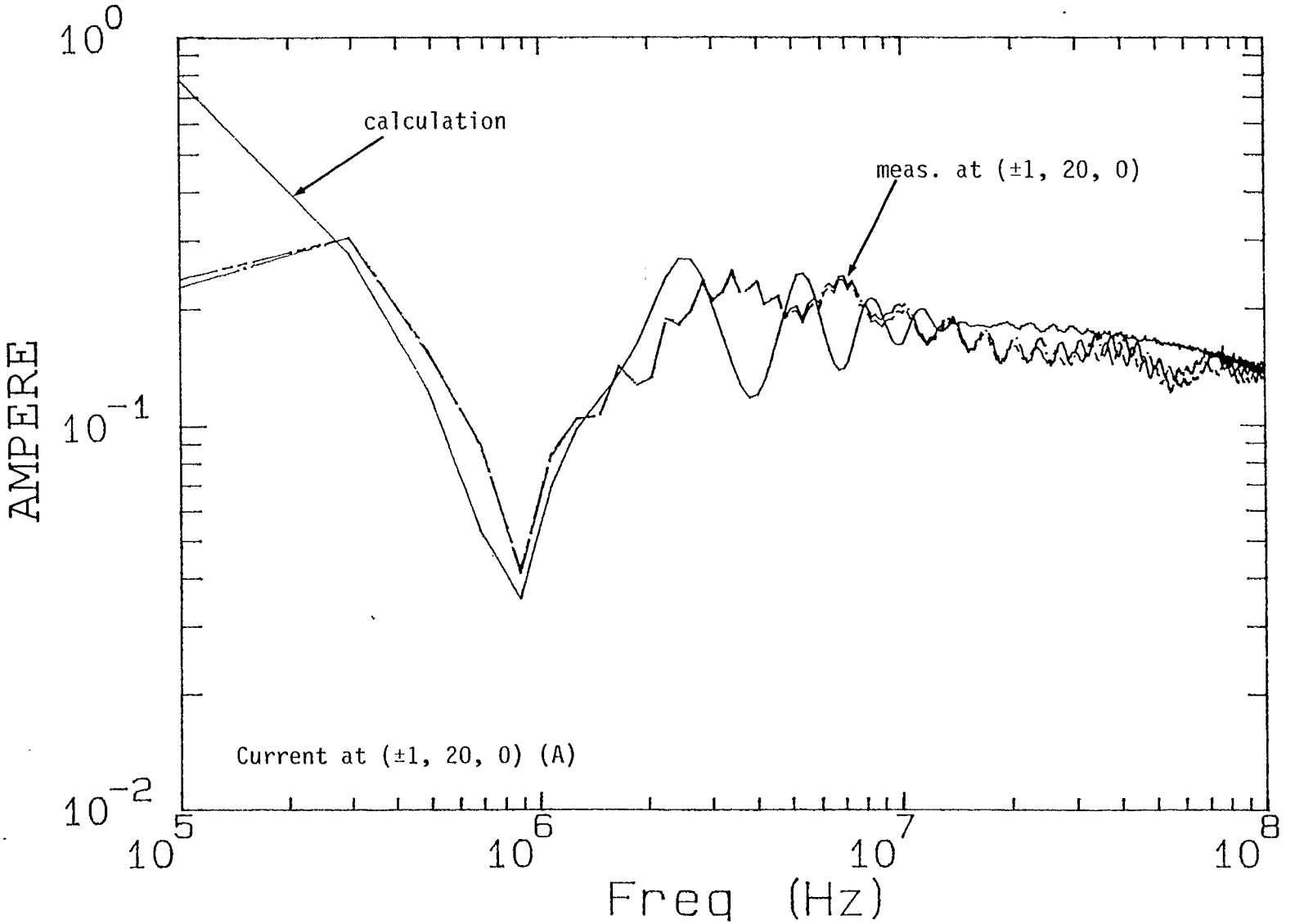

Figure 20a. Comparison between model calculations (Secs. 3.1 and 3.3) and measurements at (1, 20, 0). The logarithmic frequency scale emphasizes the low frequencies.

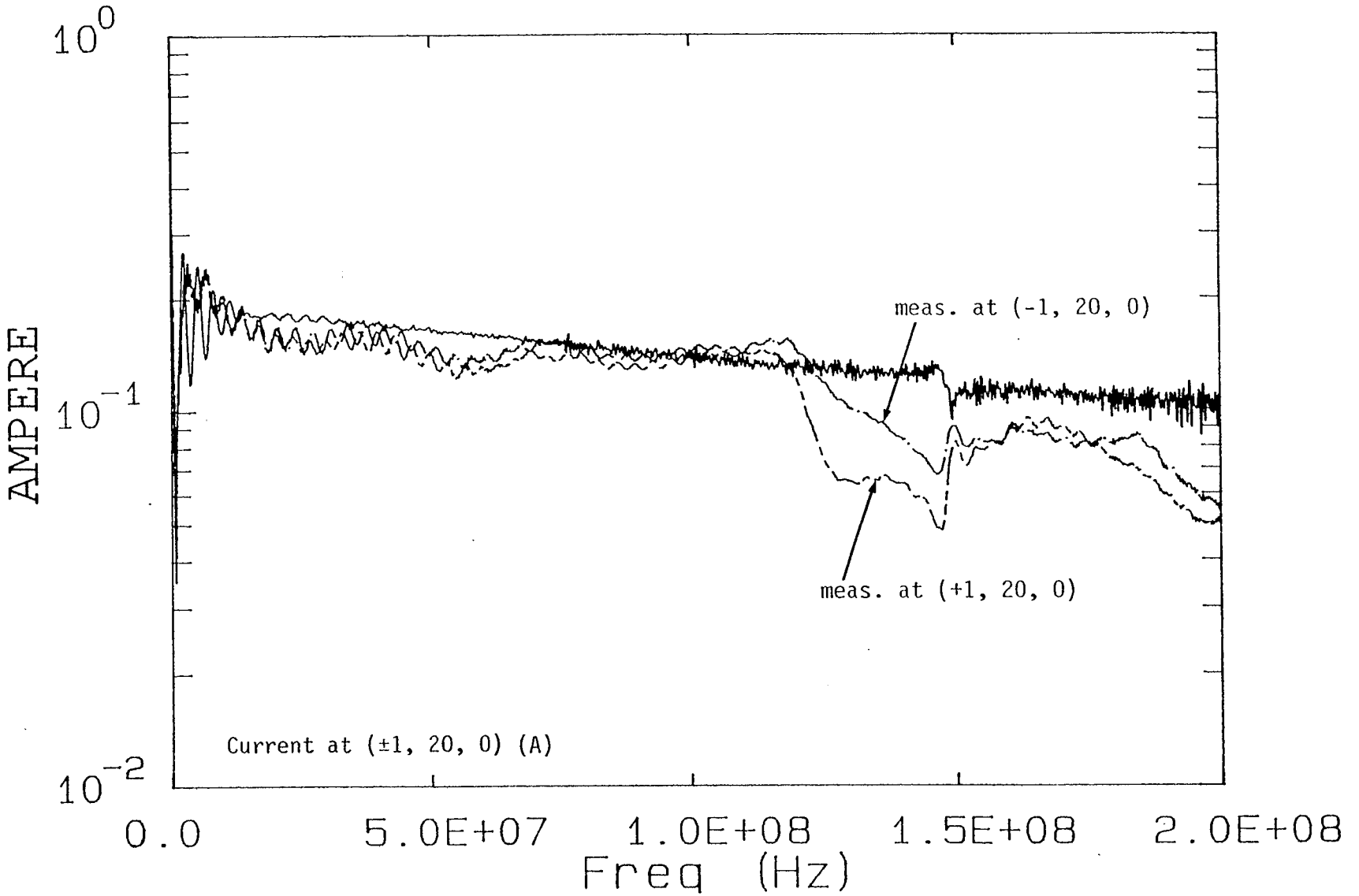

Figure 20b. Comparison between model calculations (Secs. 3.1 and 3.3) and measurements at (1, 20, 0). The linear frequency scale emphasizes the high frequencies.

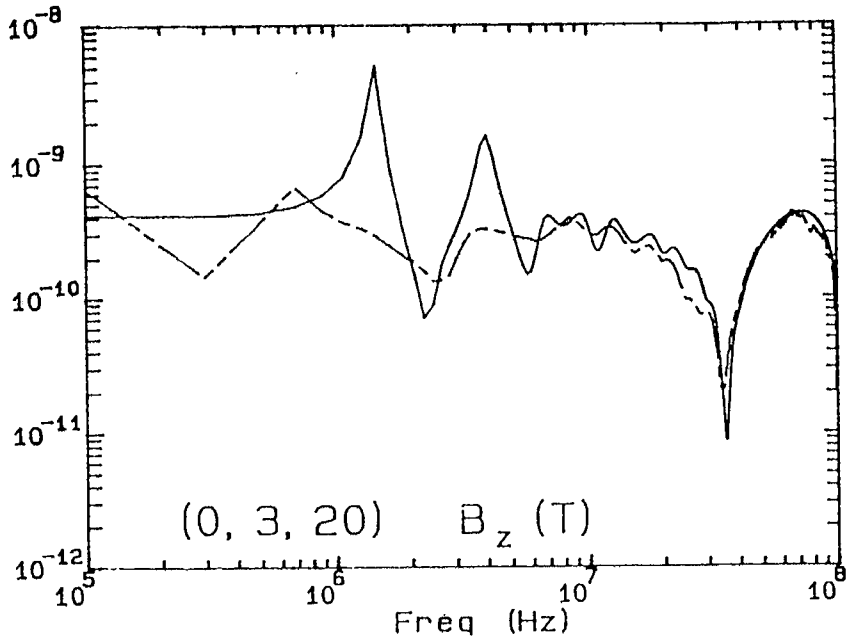

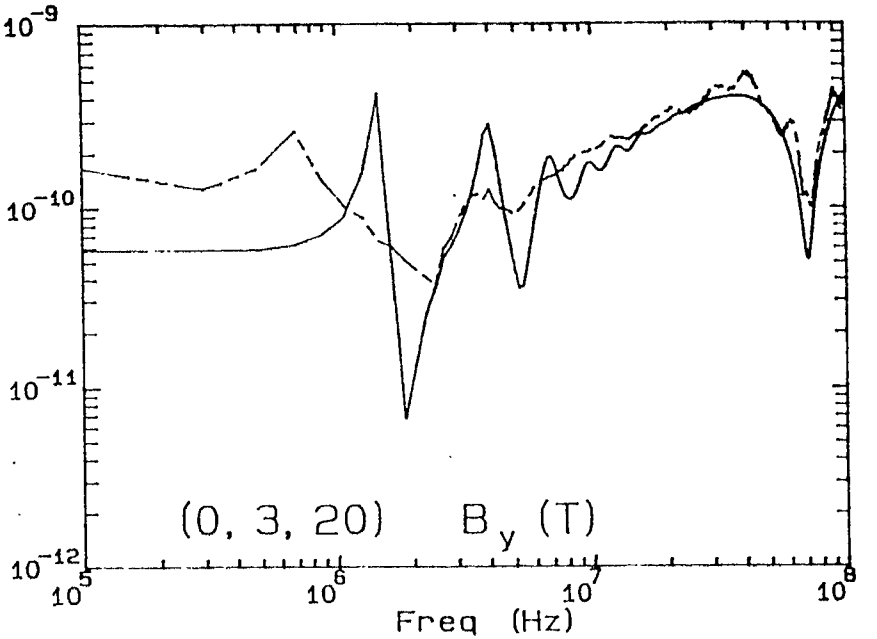

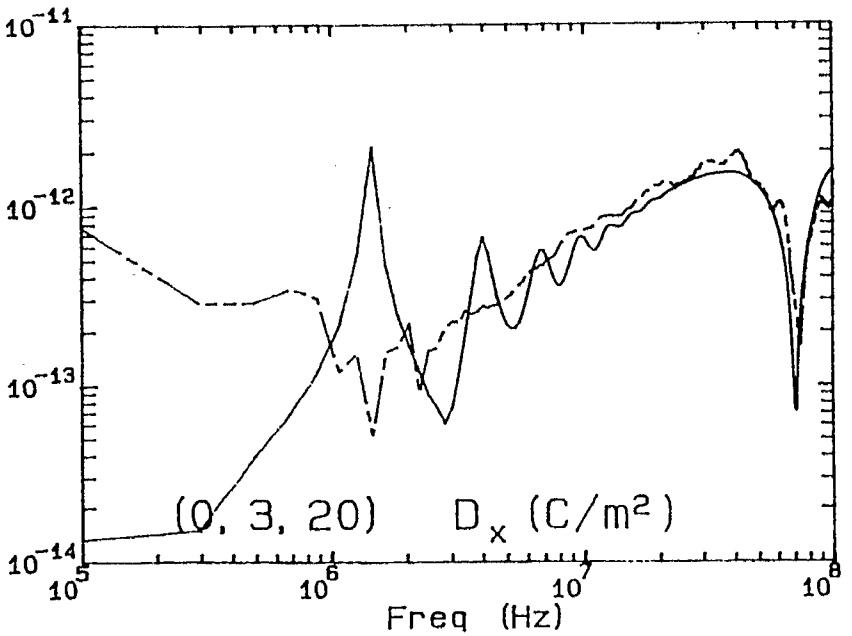

Calc.

Meas.

Triangular Geometry

Figure 21a. Comparison between model calculations (Secs. 3.2 and 3.3) and measurements at (0, 3, 20). The logarithmic frequency scale emphasizes the low frequencies.

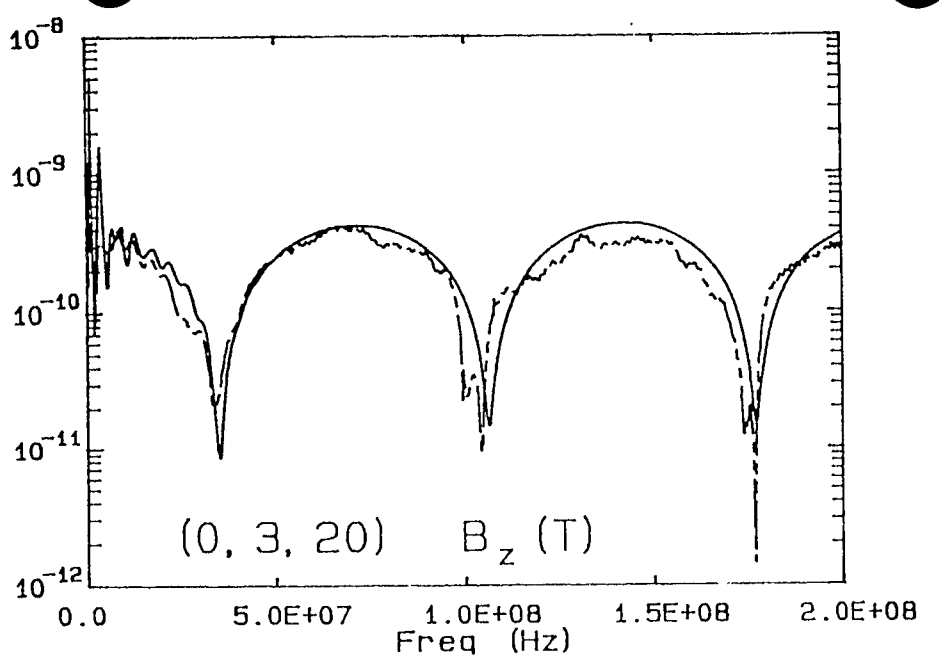

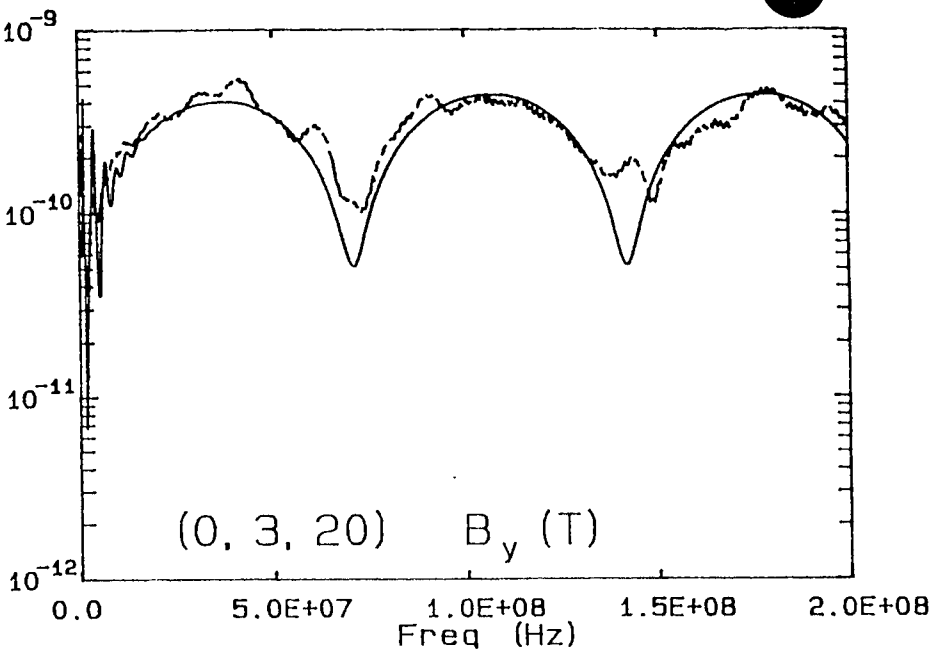

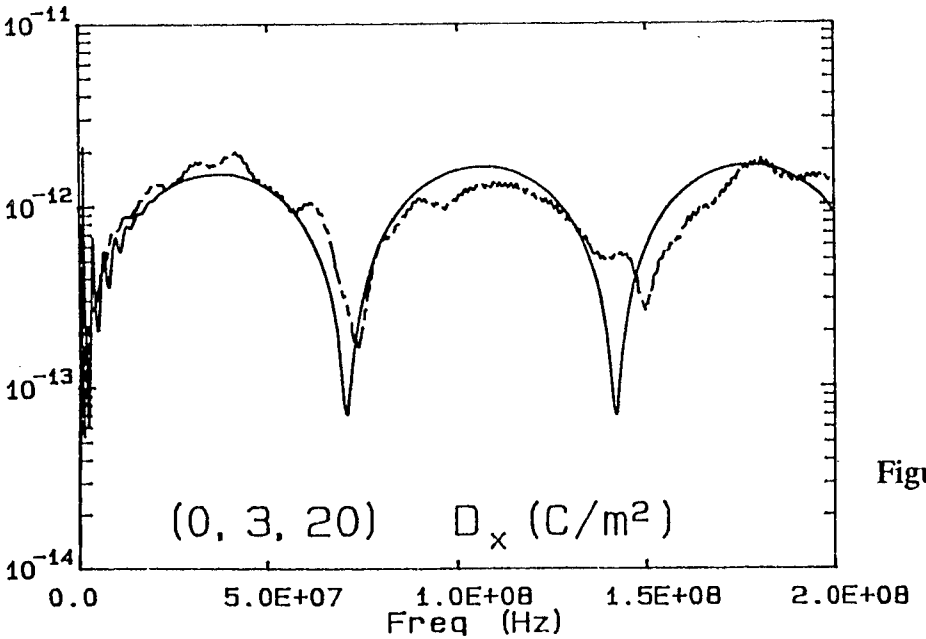

Calc.
Meas.

Triangular Geometry

Figure 21b. Comparison between model calculations (Secs. 3.2 and 3.3) and measurements (0, 3, 20). The linear frequency scale emphasizes the high frequencies.

It is pointed out that the antenna response is quite smooth at points on (or very near) the ground, as shown in Fig. 19, excluding the small residual resonant behavior exhibited at frequencies below 10 MHz. This is caused by the limitations of the ferrite loading to provide for a complete damping of the first few resonances. On the other hand, at points above the ground both measurements and calculations exhibit an interference pattern with repetitions of broad maxima and sharp nulls, whose location and periodicity, in frequency, depend on the coordinates of the test point itself. To explain such behavior for the point (0, 3, 20), chosen as an example, one can refer to the sketch of Fig. 22 which illustrates the paths of interference between a plane wave originating at the source (0, 20, 0) and propagating towards P in the direction identified by k_{dir} and a plane ave originating at the image point (0, -20, 0), and propagating along the direction given by k_{ima}. Note that the plane of the figure is perpendicular to that containing the antenna and passes through its center. The path difference Δ between the two rays is, for this specific case, 4.23 m. Such length becomes equal to one half of a wavelength in air at a frequency very close to 35 MHz. Hence, considering that the electromagnetic field components at the source and image are related in the following way

D_x source = $-D_x$ image
B_y source = $-B_y$ image
B_z source = B_z image

it is clear that D_x and B_y start off with 180° phase difference between source and image, whereas B_z has the same phase. At a frequency very close to 35 MHz an additional 180° is added and so there is a constructive interference (maximum) for D_x and B_y and a destructive interference for B_z, resulting in a minimum. The period of repetition of the pattern is ~70 MHz, which corresponds to Δ being equal to one wavelength.

It is stressed that the fields presented here are total fields, i.e. they include incident and ground reflected components. To fairly evaluate the antenna characteristics, one should look at incident fields only. In fact, the knowledge of the incident field is needed to perform an extraplation process of the responses induced inside a system by some kind of threat, since threat fields are usually defined as incident fields. Therefore, simulators such as the antenna under investigation here should be designed and evaluated for their ability to generate an incident field which is as close as possible to that of a uniform plane wave in a predefined volume. To this effect we evaluated the incident field at the point (0, 3, 20) by not including the ground reflected contribution in our model and the results are presented in Fig. 23. It is shown that the interference pattern has been eliminated, as expected, and only the effect of the first few antenna resonances is visible. At frequencies above 10 MHz the field is flat since all the resonances at

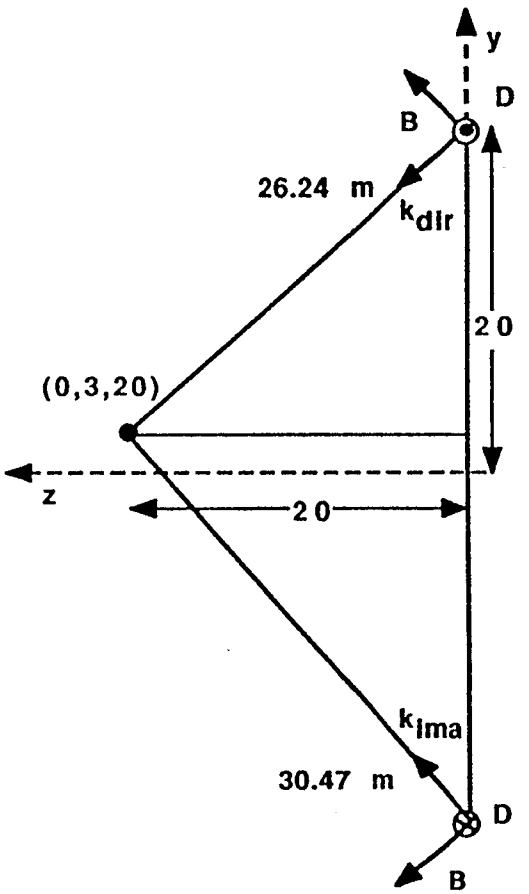

Figure 22. Scheme of interference of incident and reflected field components at (0, 3, 20).

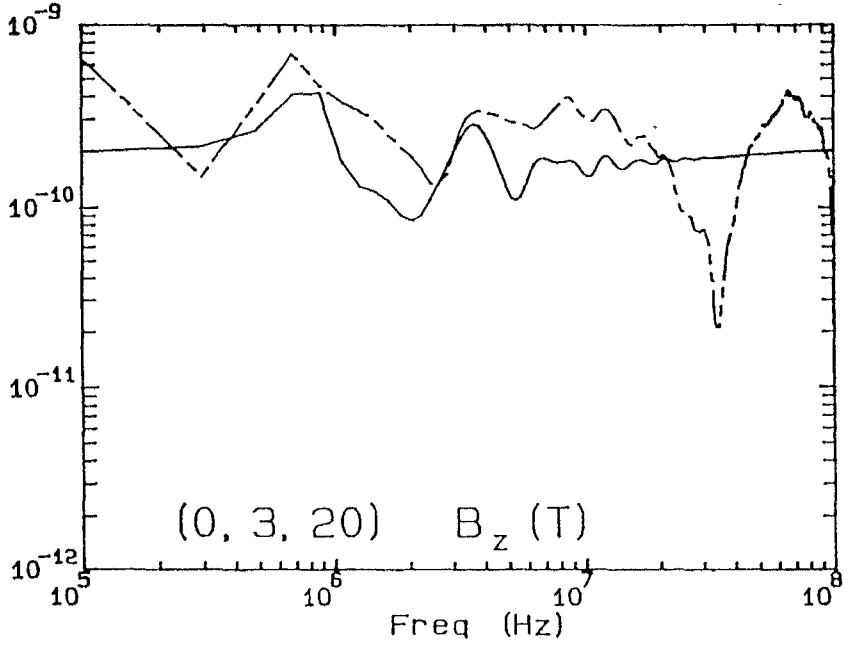

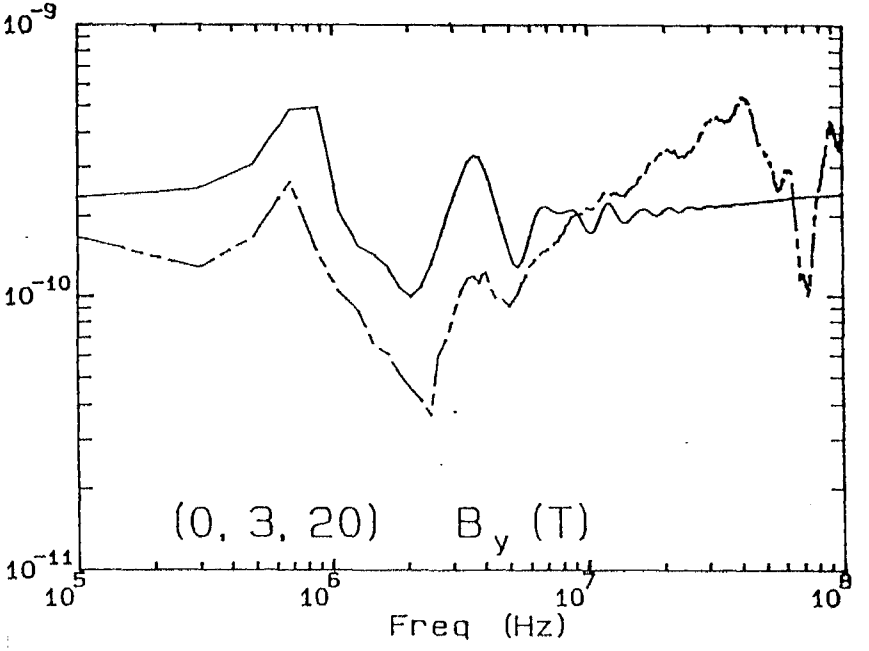

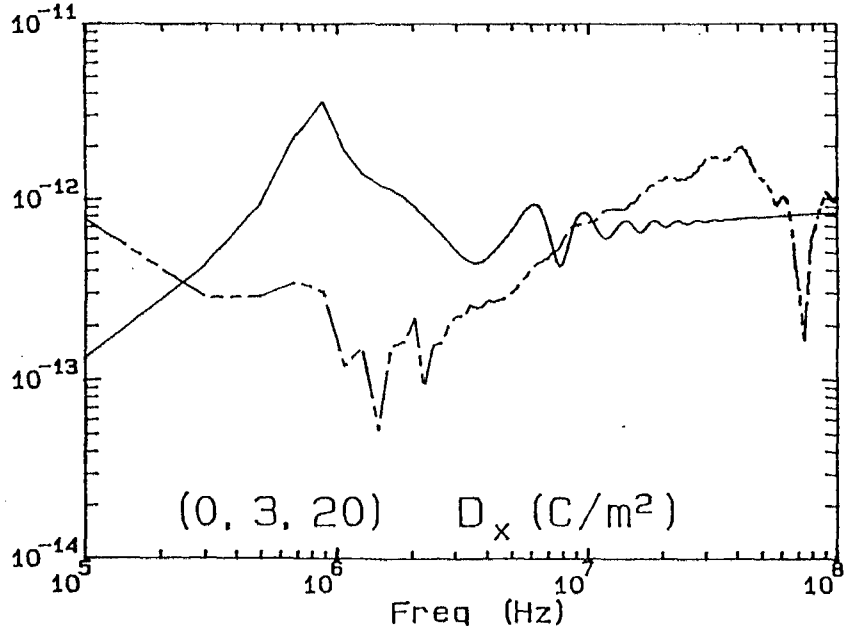

Calc.
Meas.

Figure 23a. Comparison between measured total field and calculated incident field at (0, 3, 20). The logarithmic frequency scale emphasizes the low frequencies.

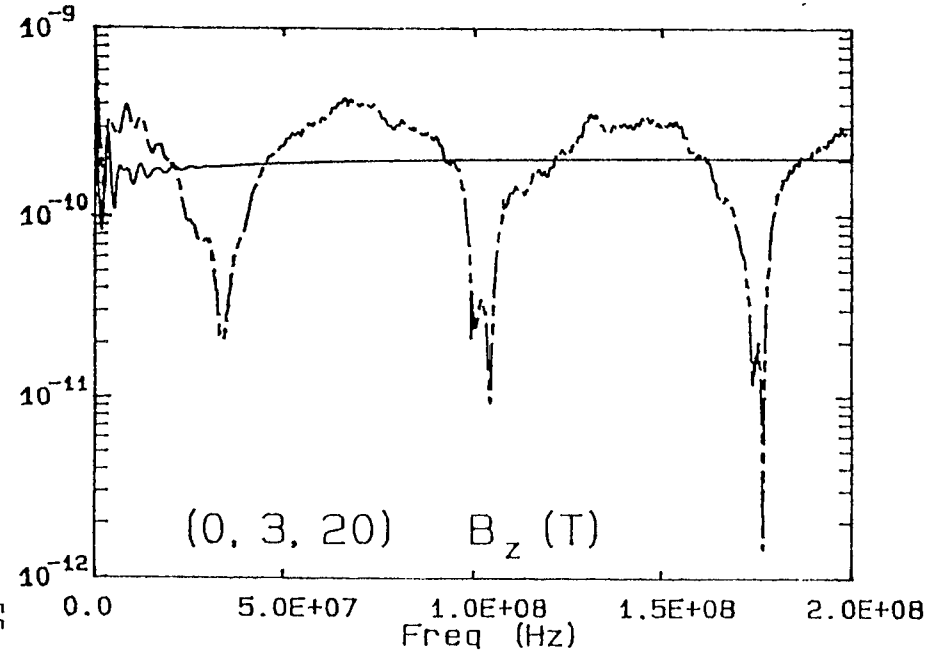

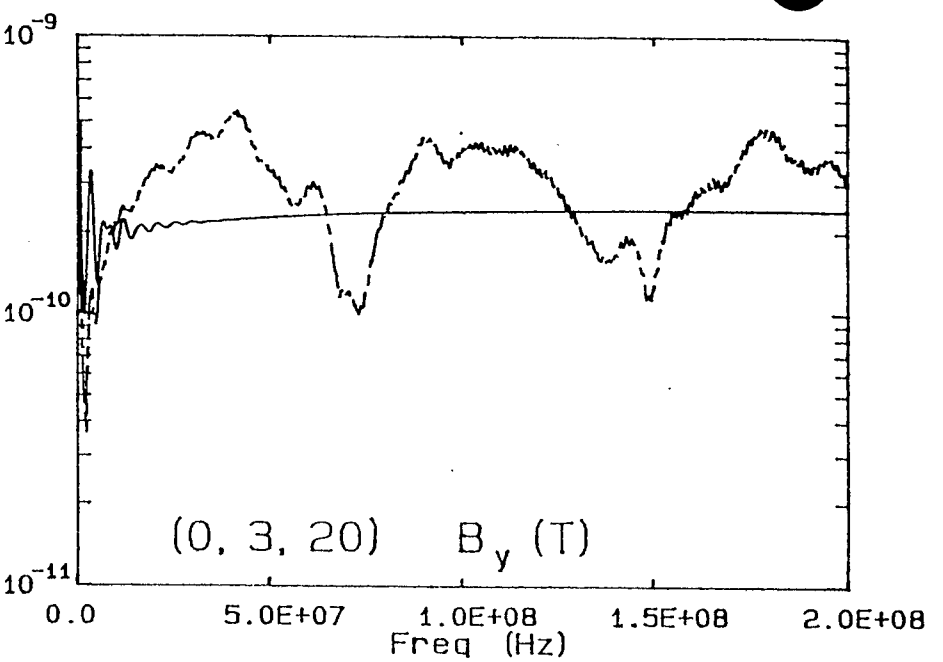

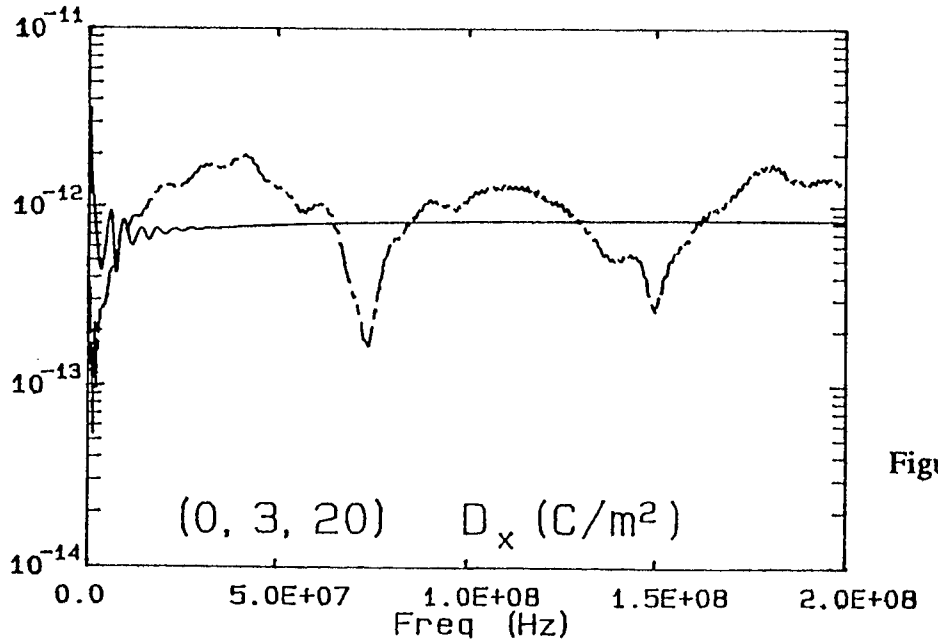

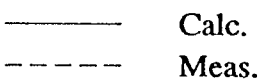

Figure 23b. Comparison between measured total field and calculated incident field at (0, 3, 20). The linear frequency scale emphasizes the high frequencies.

high frequencies are completely damped by the ferrite load. Note that the incident D_x and B_y at frequencies below 10 MHz are higher than the total fields, whereas B_z is lower (in the same frequency range) consistently with the model of interference and the sign relationship described in the paragraph above.

4.2.2 Elliptical Geometry

For the elliptical geometry the input impedance was obtained through measurements of the reflection coefficient at the section where the coaxial cable is cut open. Since the network analyzer measures the reflection coefficient at an internal instrument interface, to obtain the value at the desired antenna gap one needs to take, in addition, a measurement of the portion of cable between the instrument and the wanted interface, configured as an open circuit. The ratio of reflection coefficients thus transfers the measurement to the antenna gap.

Two configurations were considred; in the first one the antenna leg fed by the network analyzer had its inner conductor directly attached to the outer conductor of the second leg at the gap, in the second configuration a resistor was added between the center and outer conductor of the antenna first leg to reduce the mismatch. The resulting input impedance for both cases is illustrated in Figs. 24-25. Note the behavior of the impedance in the case there is no resistor: due to the resonances of the loop (the first appears around 450 kHz) the impedance varies substantially, particularly around 1 MHz. This is attributed to the characteristic of the #77 material ferrite toroids which exhibit a resonance at around 1 MHz that coincides with a loop resonance. The impedance gradually decays above 10 MHz, and the rate of decay changes with ferrite loading.

It appears clear that when a 50 Ω resistor is added in parallel, the overall input impedance is lowered at frequencies below 50 MHz, while above the parallel arrangement introduces a resonance around 100 MHz. In this case the total impedance becomes inductive at high frequencies, whereas in the absence of the parallel resistor the impedance was slightly capacitive. Evidently the 50 Ω resistor is not just a pure resistor at high frequencies but has some reactance as well. In fact, by modeling the 50 Ω resistor at high frequencies as an impedance $R_1 + j\omega L_1$, and placing this in parallel with the antenna impedance $R + 1/j\omega C$, it can easily be shown that there is a value of frequency at which resonance occurs, i.e. the imaginary part of the total impedance is zero. Such value is

$$\omega_R = \left[\frac{1}{CL_1} \frac{CR_1^2 - L_1}{CR^2 - L_1} \right]^{1/2} \tag{52}$$

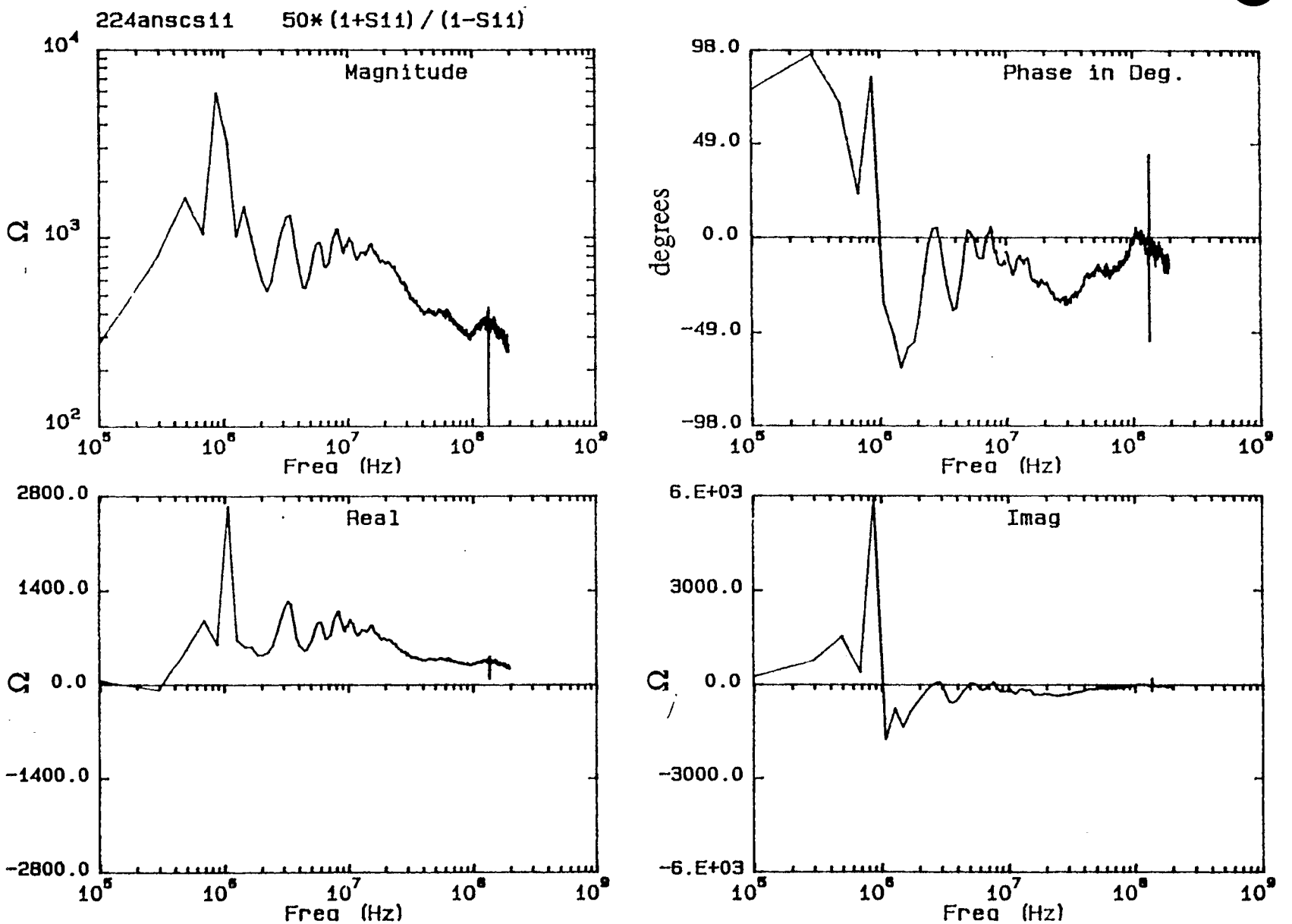

Figure 24. Input impedance for loop of elliptical geometry (Fig. 7). No matching resistor used here (Baseline configuration).

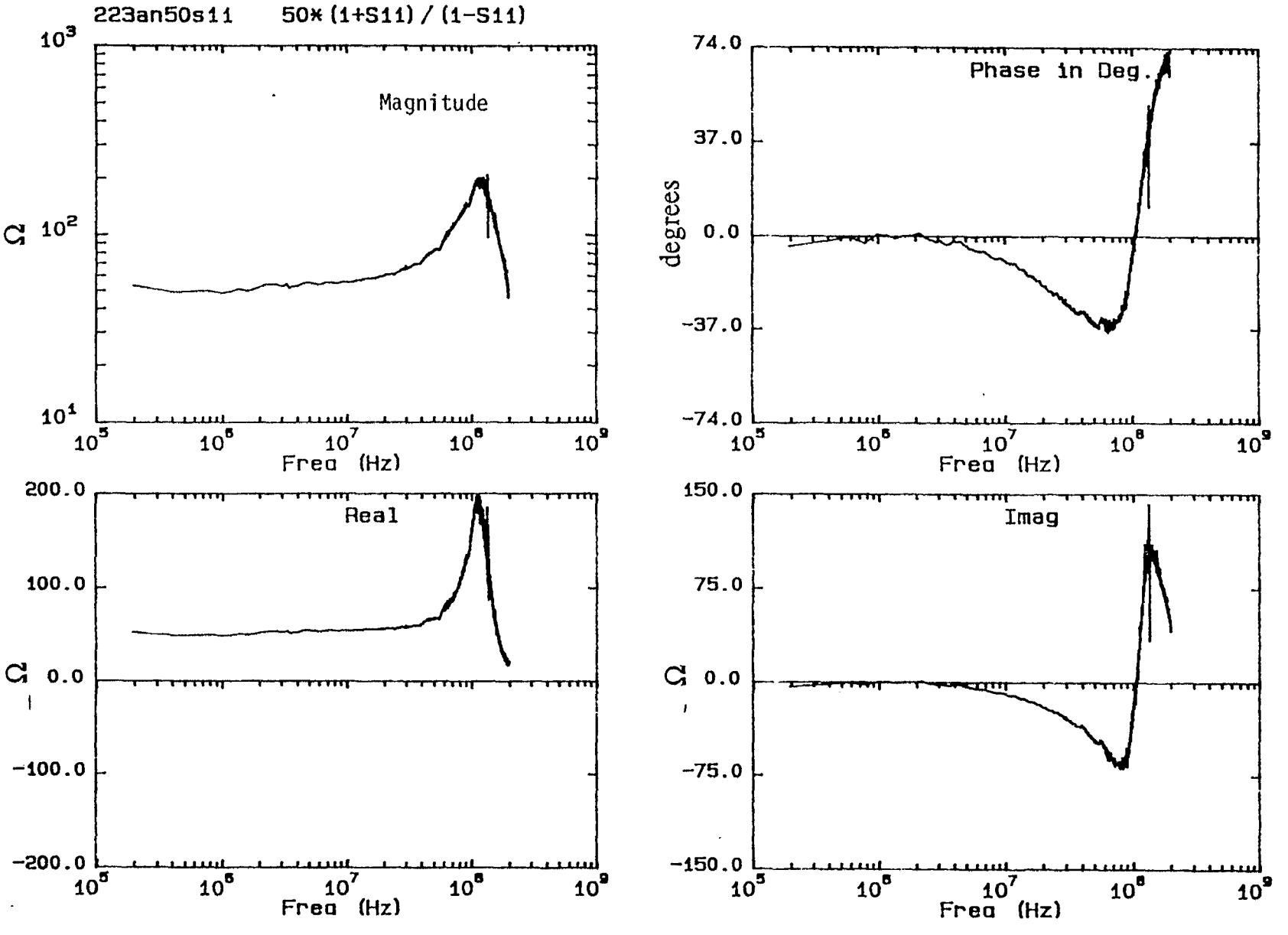

Figure 25. Antenna input impedance when a 50 Ω resistor is placed in parallel, according to Fig. 7. (Baseline configuration, elliptical geometry).

This problem can be mitigated by using shorter lead lengths or a parallel combination of resistors.

The comparisons for the semi elliptical loop are reported in Figs. 26-29, and the chosen set of measured points closely resembles that used for the triangular shape. The overall agreement between measurements and calculations is very similar to that obtained for the other geometry and similar considerations can be made to explain the features of the fields.

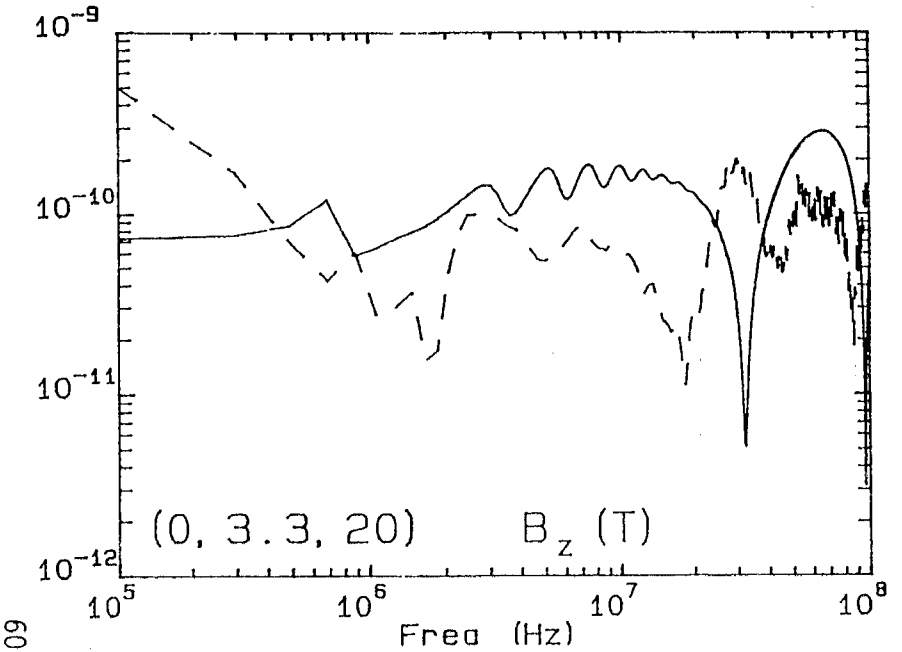

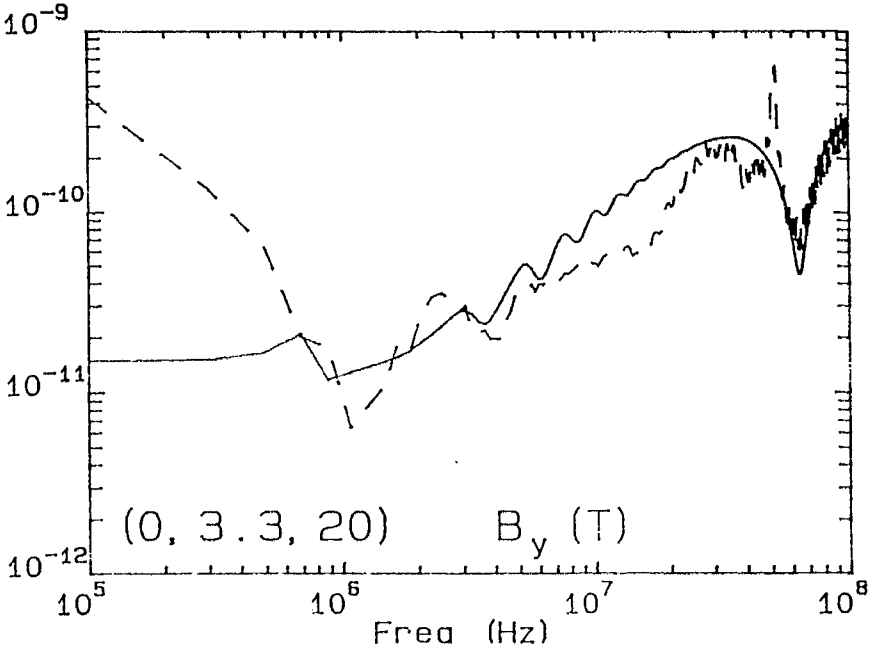

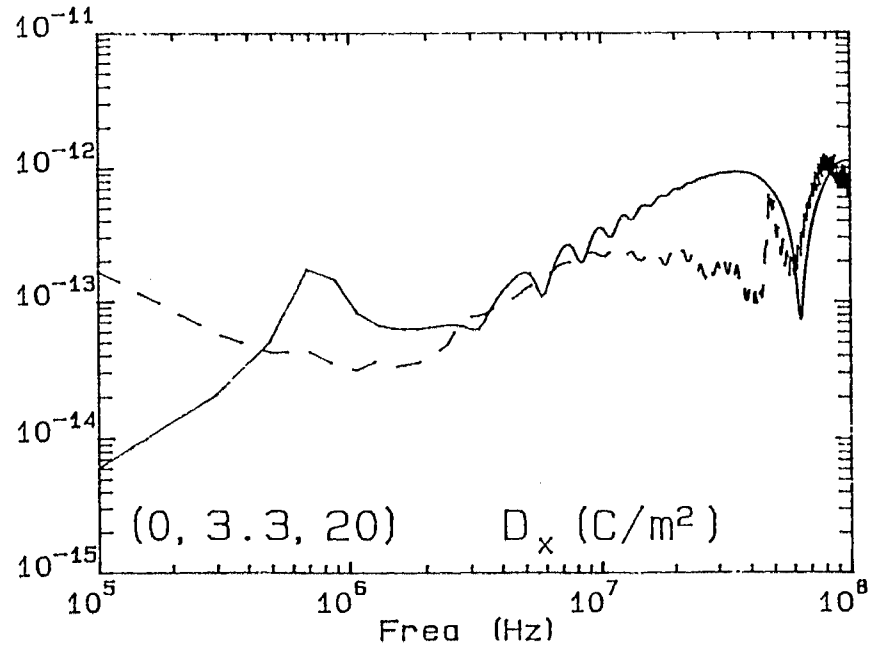

Calc.

Meas.

Elliptical Geometry

Figure 26a. Comparison between model calculations (Secs. 3.1 and 3.3) and measurements at (0, 3.3, 20). The logarithmic frequency scale emphasizes the low frequencies.

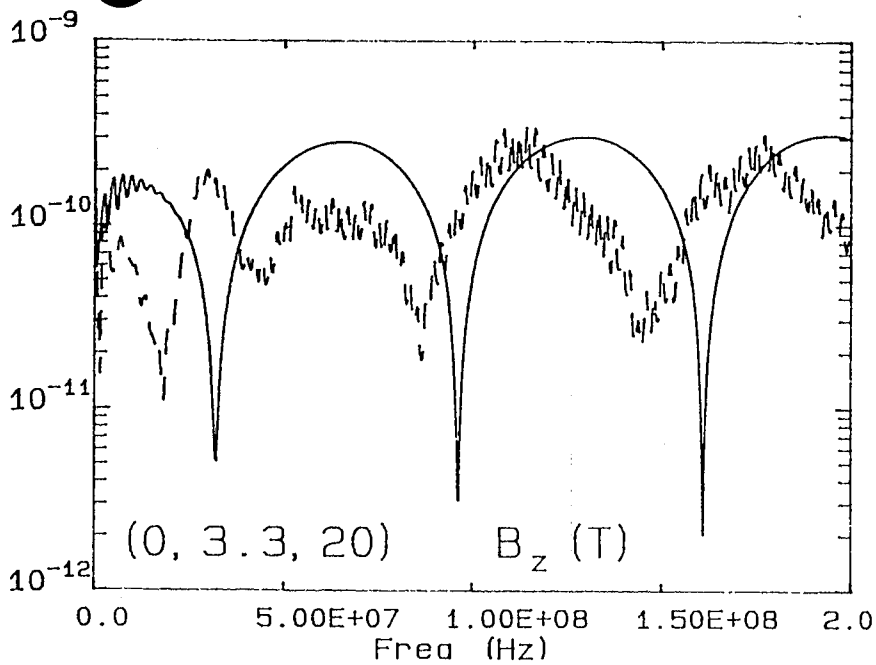

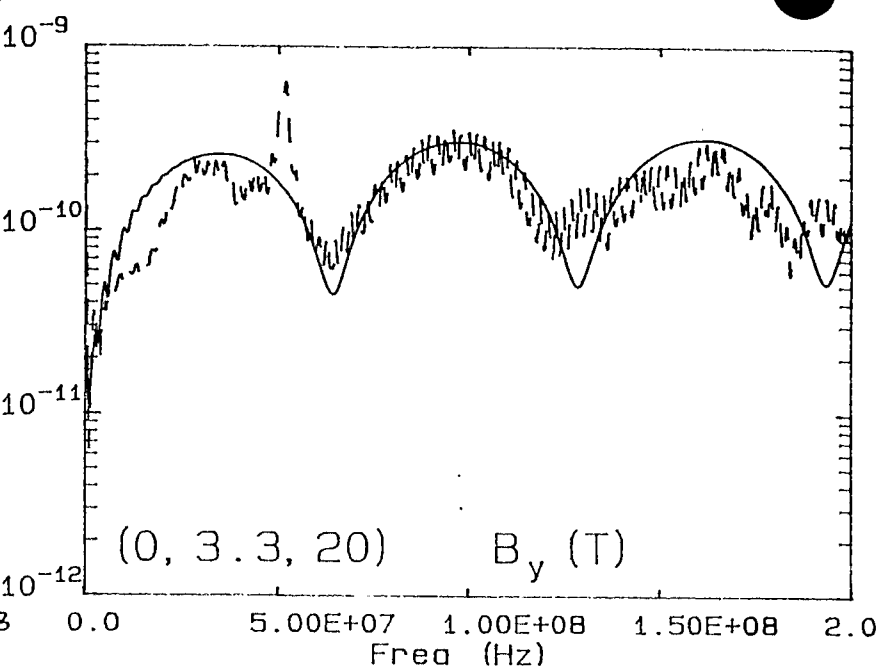

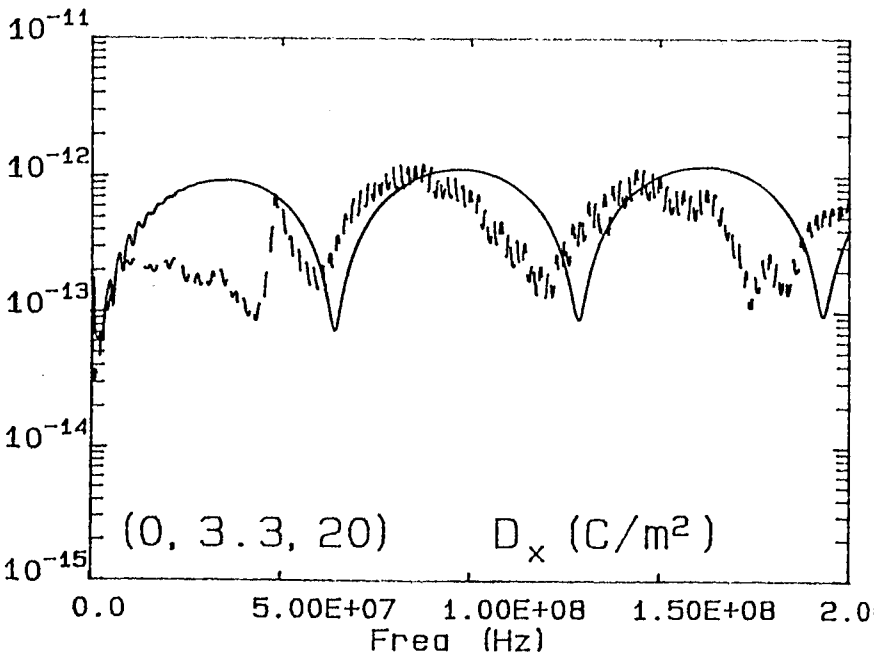

Calc.

Meas.

Elliptical Geometry

Figure 26b. Comparison between model calculations (Secs. 3.1 and 3.3) and measurements at (0, 3.3, 20). The linear frequency scale emphasizes the high frequencies.

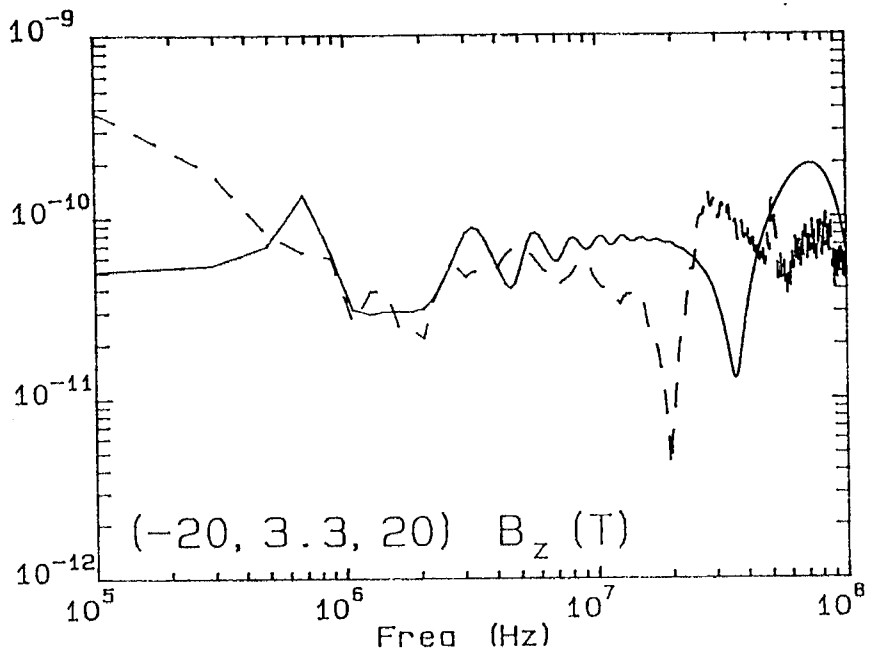

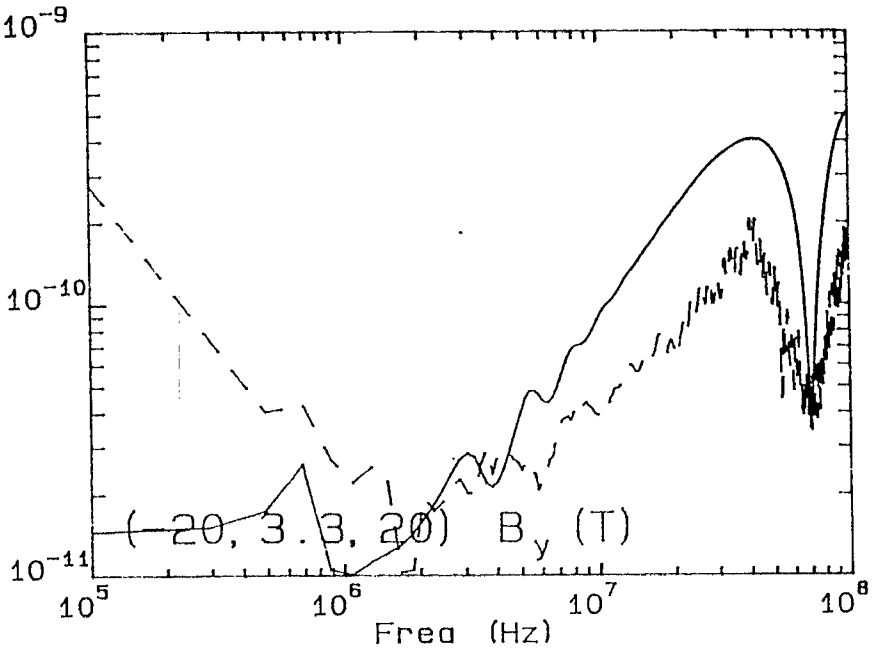

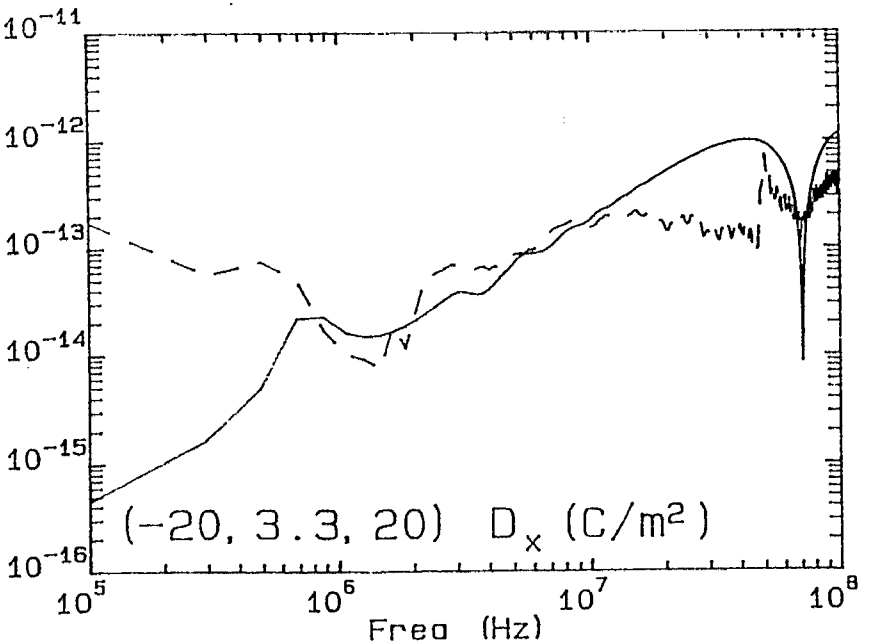

Calc.

Meas.

Elliptical Geometry

Figure 27a. Comparison between model calculations (Secs. 3.1 and 3.3) and measurements at (-20, 3.3, 20). The logarithmic frequency scale emphasizes the low frequencies.

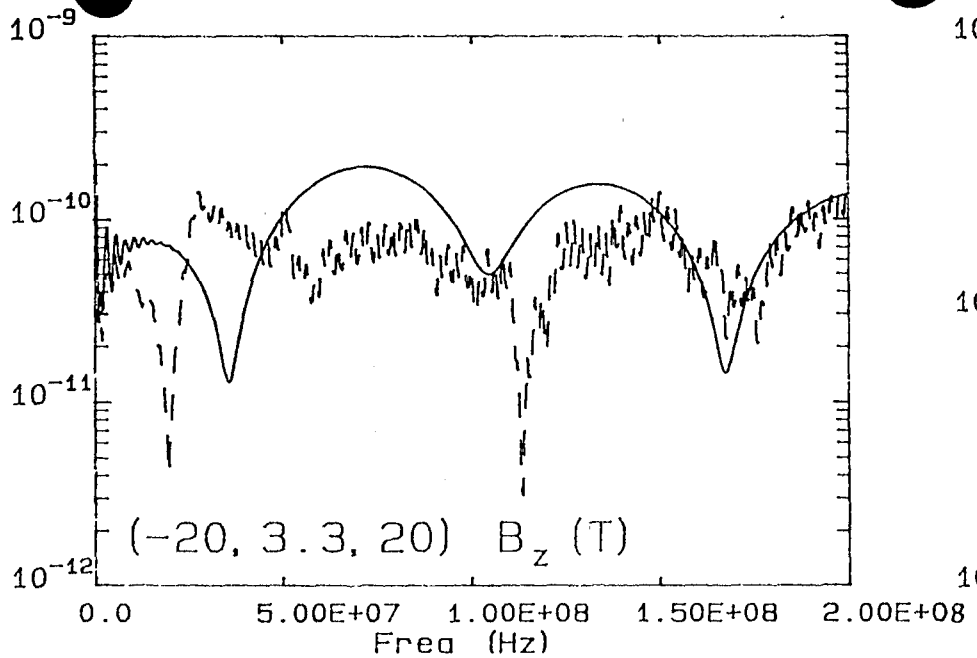

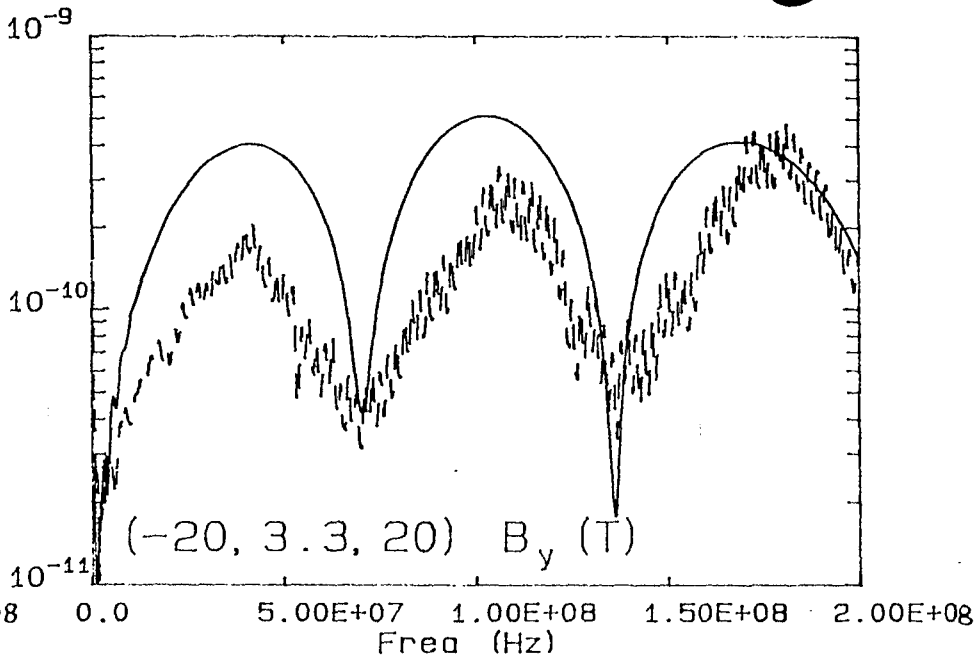

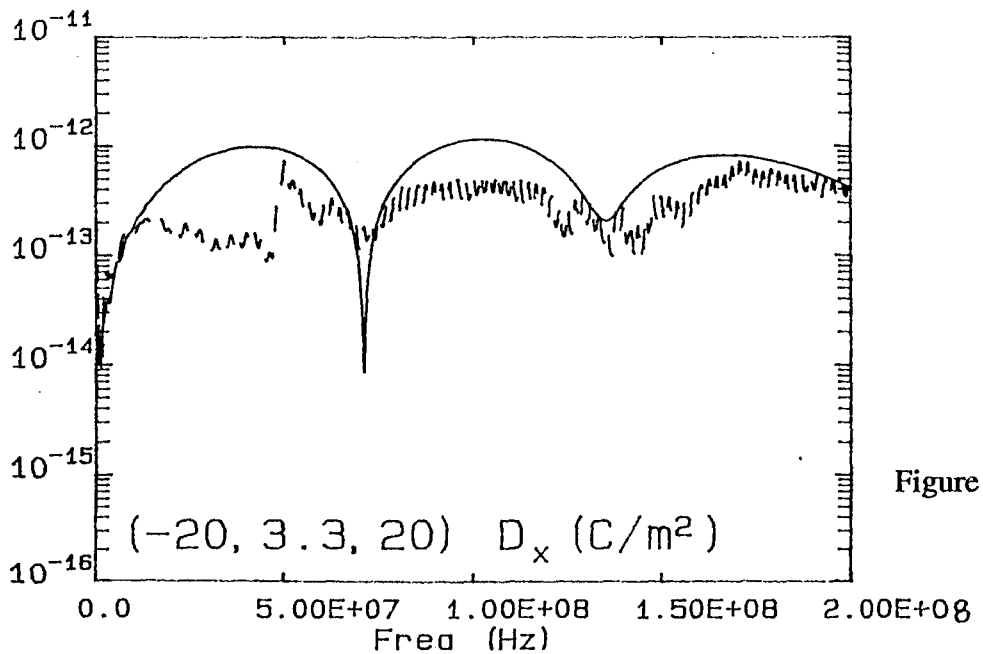

Calc.

Meas.

Elliptical Geometry

Figure 27b. Comparison between model calculations (Secs. 3.1 and 3.3) and measurements at (-20, 3.3, 20). The linear frequency scale emphasizes the low frequencies.

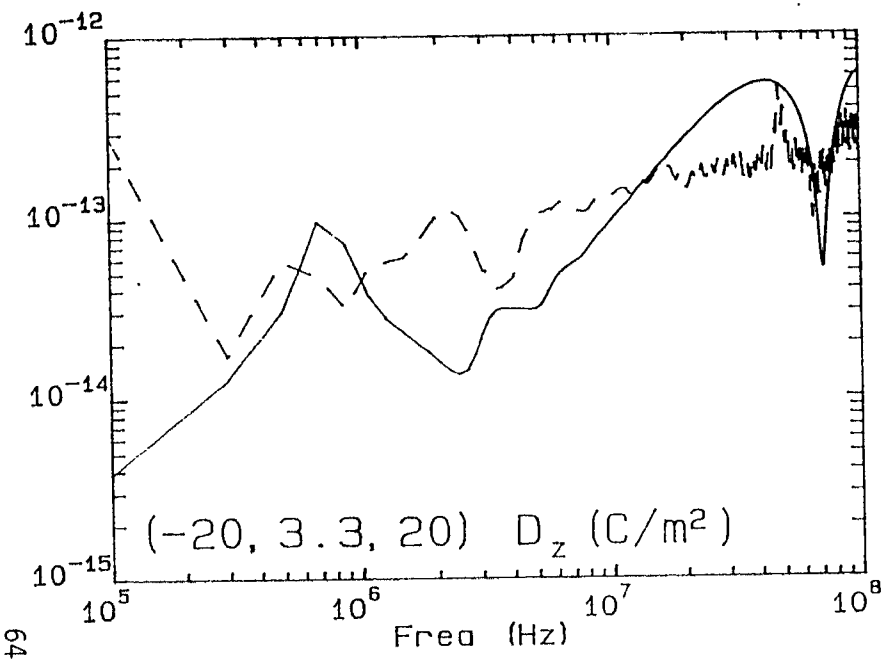

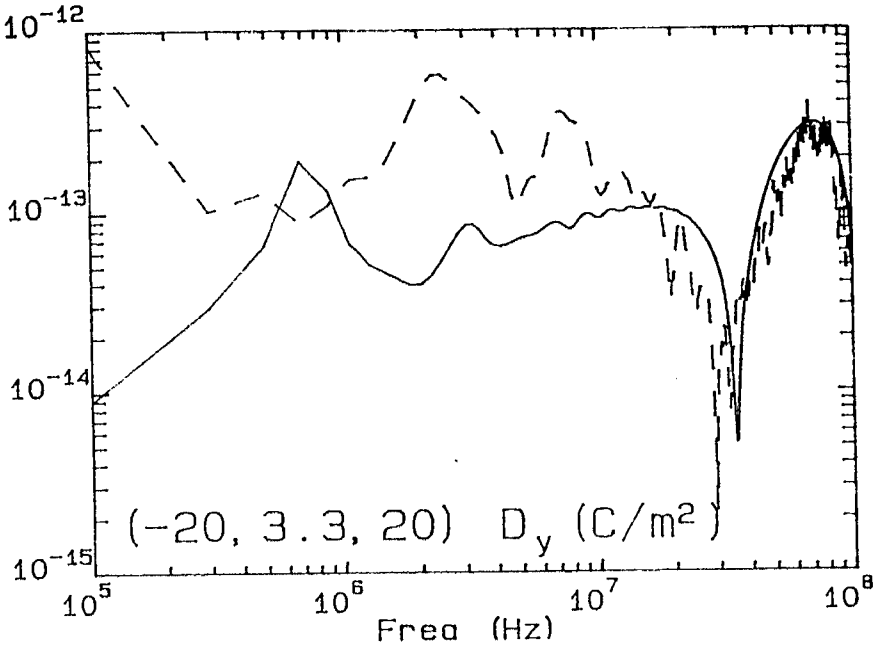

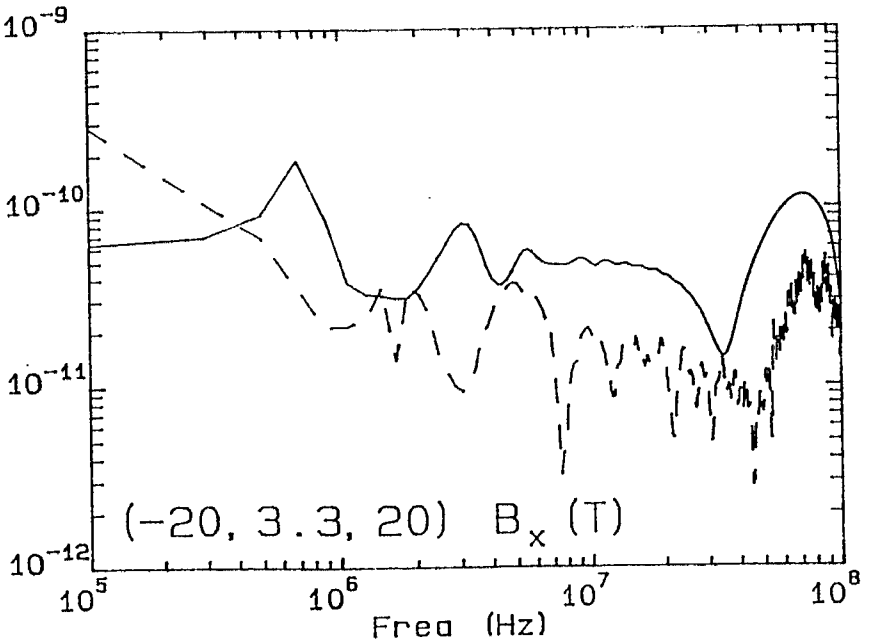

Calc.

Meas.

Elliptical Geometry

Figure 28a. Comparison between model calculations (Secs. 3.1 and 3.3) and measurements at (-20, 3.3, 20). The logarithmic frequency scale emphasizes the low frequencies.

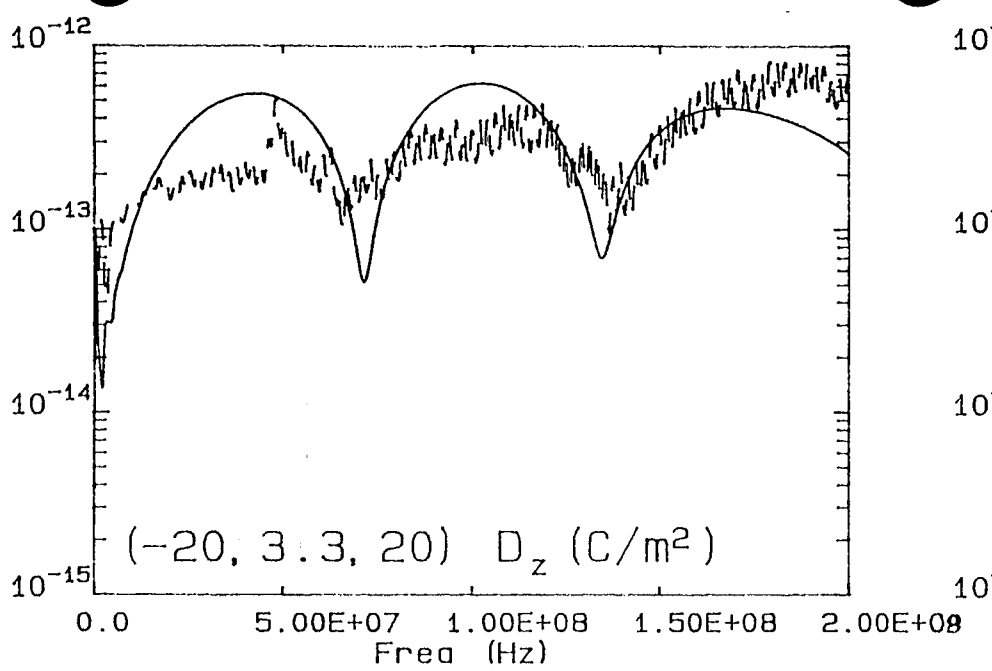

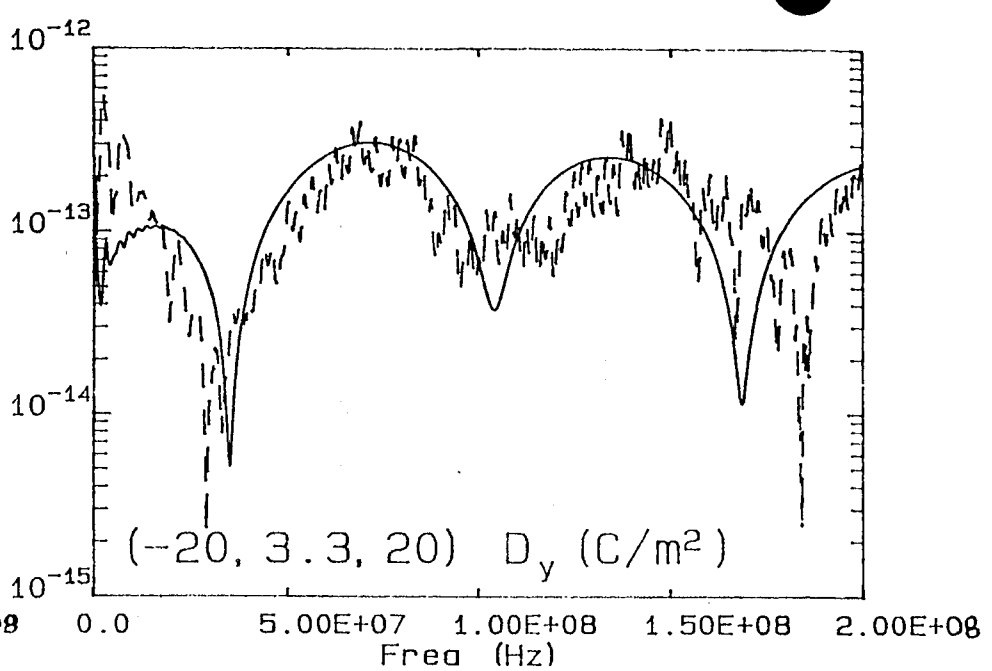

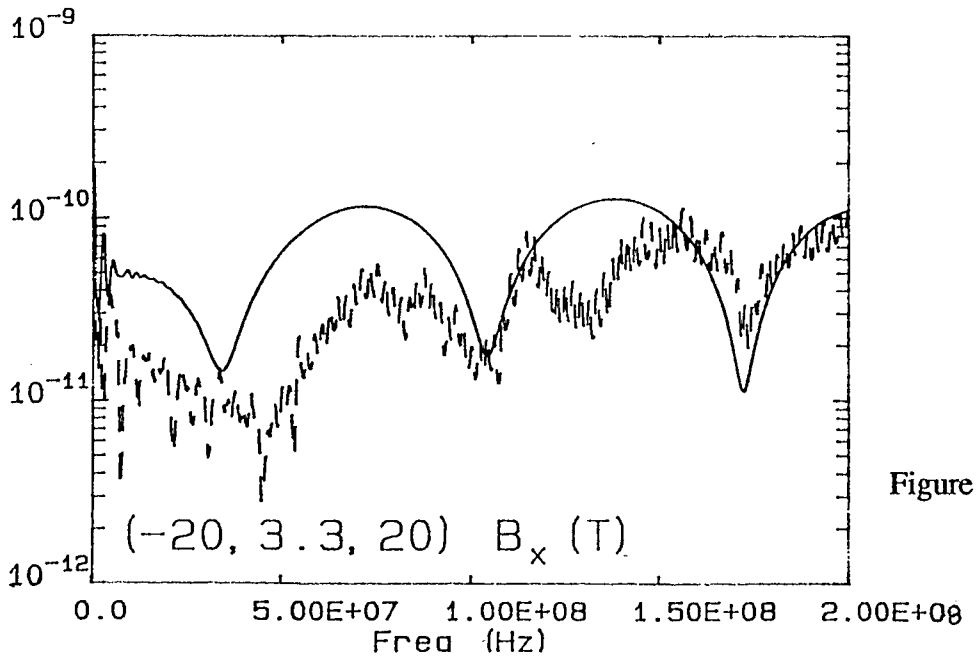

Calc.

Meas.

Elliptical Geometry

Figure 28b. Comparison between model calculations (Secs. 3.1 and 3.3) and measurements at (-20, 3.3, 20). The linear frequency scale emphasizes the low frequencies.

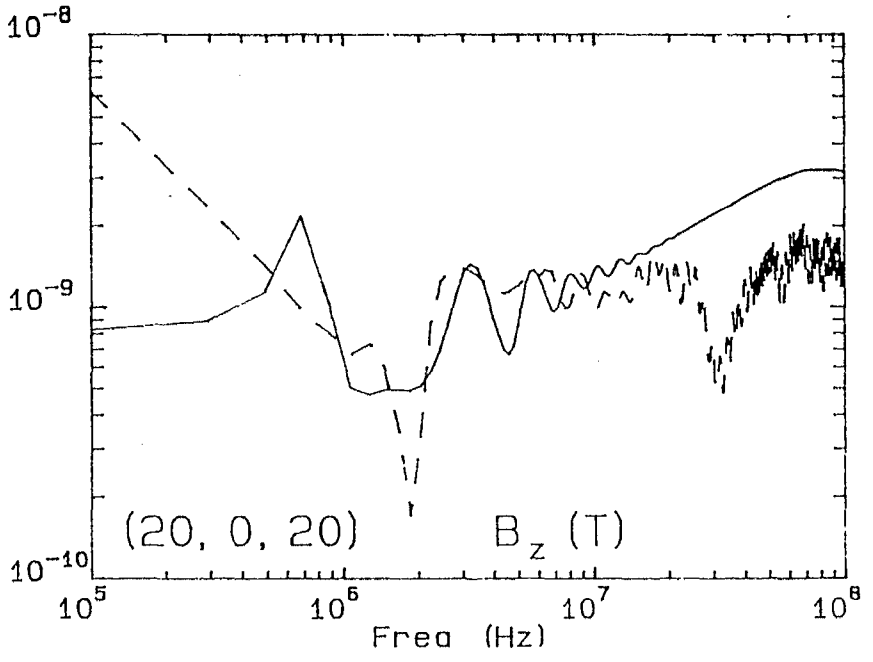

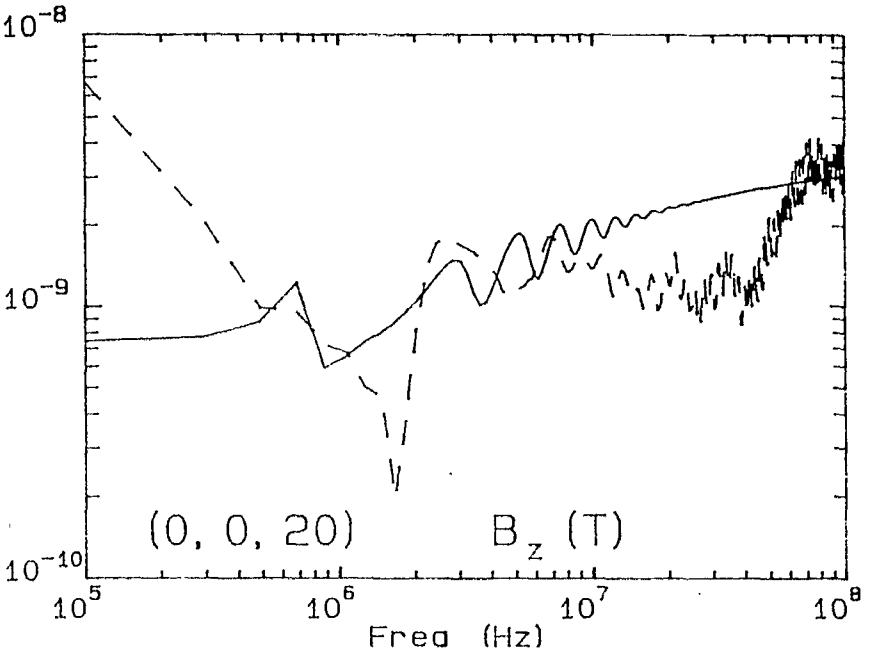

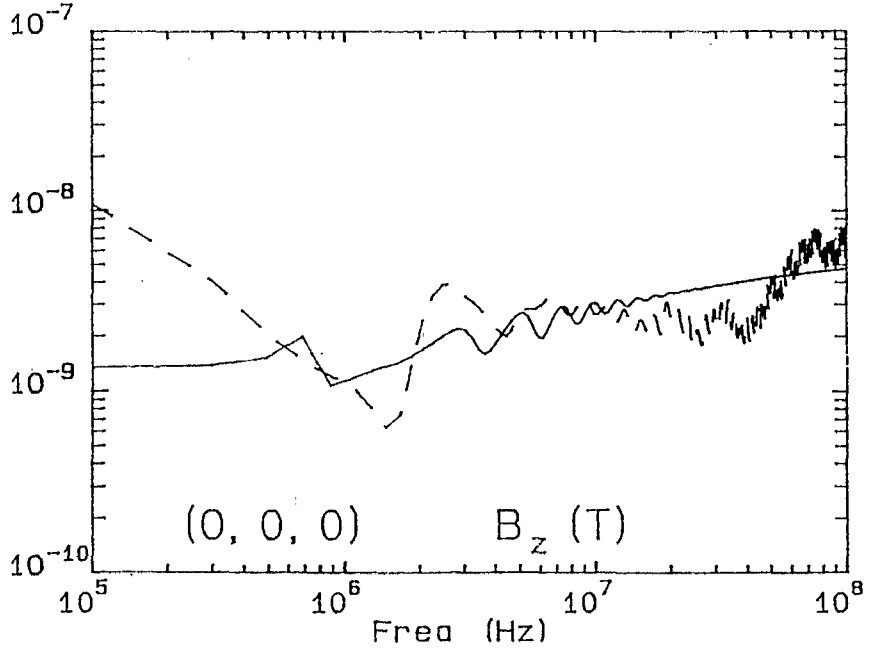

Calc.
Meas.
Elliptical Geometry

Figure 29a. Comparison between model calculations (Secs. 3.1 and 3.3) and measurements at (20, 0, 20), (0, 0, 20), and (0, 0, 0). The logarithmic frequency scale emphasizes the low frequencies.

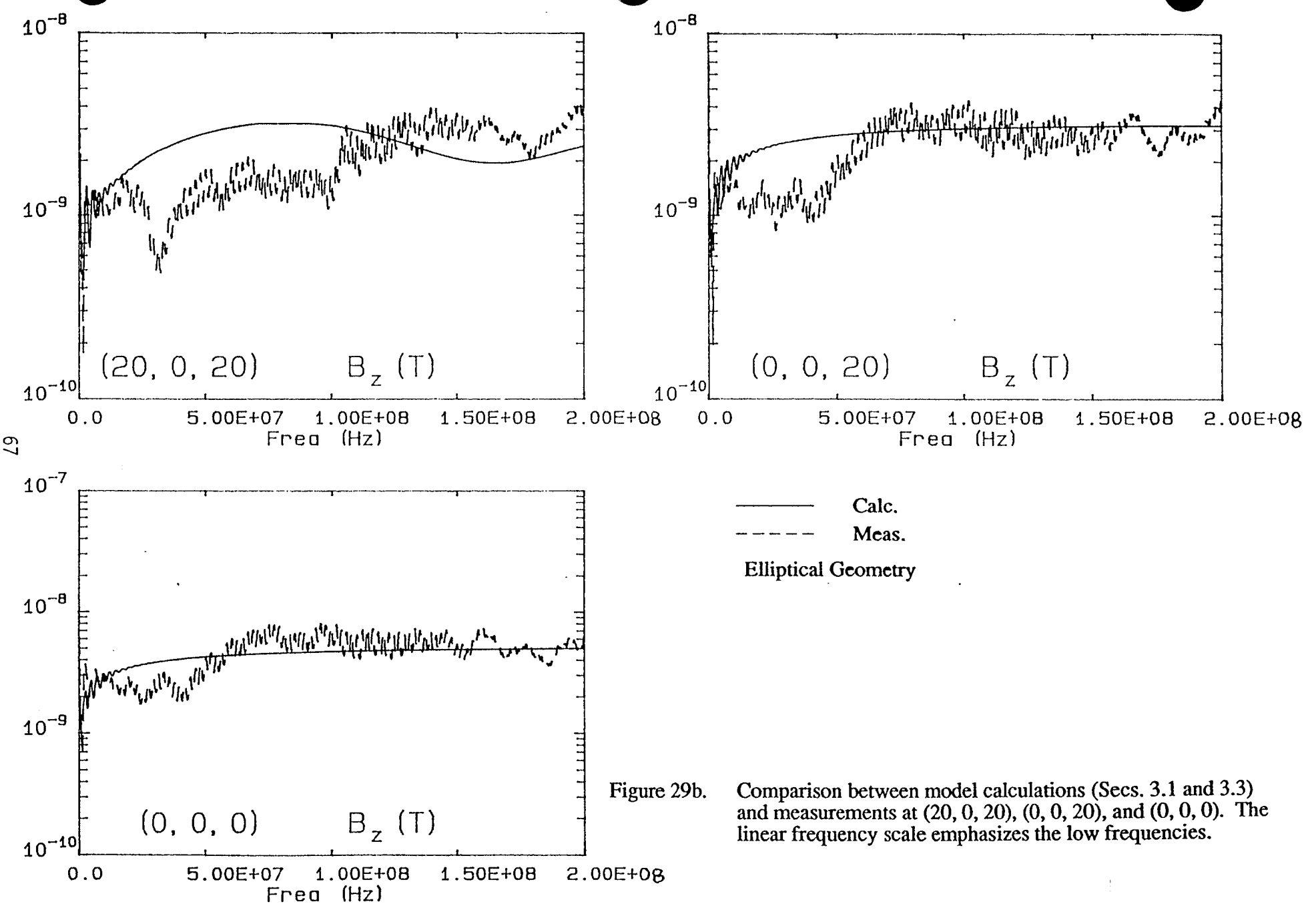

Figure 29b. Comparison between model calculations (Secs. 3.1 and 3.3) and measurements at (20, 0, 20), (0, 0, 20), and (0, 0, 0). The linear frequency scale emphasizes the low frequencies.

5.0 DESIGN IMPROVEMENTS

The current choice of ferrite load provides a reasonable damping of the unwanted antenna resonances but has drawbacks, particularly at low frequency. In fact the frequency dependent ferrite impedance is very small at low frequencies because the inductance is very small and does not provide sufficient load, since the ferrites are designed as low pass filters. Furthermore, the impedance varies with frequency and is not completely controllable. Ideally, one would like to have a constant resistance along the antenna, according to the discussion presented in Sec. 1 where an approach is outlined to accomplish this goal. However materials other than ferrites must be used as magnetic cores so that at all frequencies of interest the core impedance is much larger than that of the constant resistor which is inductively coupled to the antenna cable through the core. Suitable materials have recently been identified and future efforts will be devoted to improve the existing illuminator concept with a controlled resistive loading.

REFERENCES

[1] Zuffada, C. Yang, F.C. and Wong, I.: "On the Thin Toroidal And Elliptical Antennas," Sensor and Simulation Note 315, January 1989. Also "Currents and Fields of Thin Circular And Elliptical Loops," IEEE Transactions on EMC, Vol. 33, No.2, May 1991.

[2] Baum, C.E. and Chang, H.: "Fields at The Center of a Full Circular TORUS And a Vertically Oriented TORUS on a Perfectly Conducting Earth," Sensor and Simulation Note 160, December 1972.

[3] Baum, C.E., Prather, W.D. and McLemore, D.P.: "Topology For Transmitting Low-Level Signals From Ground Level to Antenna Excitation Position in Hybrid EMP Simulators," Sensor and Simulation Note 333, September 1991.

[4] Baum, C.E.: "An Anisotrophic Medium For High Wave Impedance," Measurement Note 39, May 1991.

[5] Misner, C.W., Thorne, K.S. and Wheeler: Gravitation, W.H. Freeman and Co., San Francisco, 1973.

[6] Baum, C.E.: "A Spiral-Transmission-Line Technique For Detecting Slot Apertures in Shield Enclosures," Measurement Note 37, December 1987.

[7] Baum, C.E.: "Some Electromagnetic Considerations For a Rocket Platform For Electromagnetic Sensors," Sensor and Simulation Note 56, June 1968.

[8] Baum, C.E.: "Some Considerations For Inductive Current Sensors," Sensor And Simulation Note 59, July 1968.

[9] Darras, D., Zuffada, C., Marin, L. and Cheung, C.: "Achilles III Simulator Facility Description And Field-Map Set Up," Achilles Memo 10, May 1988.